

Quantifying photodegradation of peatland-derived dissolved organic carbon in the coastal ocean of Southeast Asia

Yongli Zhou¹, Moritz Müller², Nagur RC Cherukuru³, and Patrick Martin¹

¹Nanyang Technological University

²Swinburne University of Technology Sarawak Campus

³Commonwealth Scientific and Industrial Research Organisation (CSIRO)

February 21, 2023

Abstract

The terrigenous dissolved organic carbon (tDOC) exported from the peatlands in Southeast Asia appears to be extensively remineralized in the shelf sea, but the processes that drive this remineralization remain unclear. Here, we combined incubation experiments and model simulations to quantify the rate and extent of photodegradation of tDOC in the Sunda Shelf Sea. Laboratory photodegradation experiments indicate that up to 74% of the peatland tDOC is potentially labile to photochemical remineralization. Based on our estimated apparent quantum yield for tDOC remineralization, modeled in-situ solar irradiance, and measured inherent optical properties of the water column, we simulated peatland tDOC photoremineralization for two coastal regions of the Sunda Shelf Sea. These simulation results show that natural solar radiation can directly remineralize $20 \pm 11\%$ of tDOC over 2 years, which corresponds to the approximate residence time of water in the Sunda Shelf Sea, and that significant photobleaching of tDOC can occur in coastal waters over shorter time-scales. We further derived a simplified photochemical decay constant of $0.008\text{--}0.017\text{day}^{-1}$ for Southeast Asia's peatland-derived tDOC, which can be used to parameterize the recently proposed UniDOM model framework. We conclude that direct photodegradation may be a greater sink for tDOC in Southeast Asia's coastal ocean compared to higher latitudes, although it is insufficient to account for the total tDOC remineralization observed in the Sunda Shelf Sea.

1 Quantifying photodegradation of peatland-derived dissolved organic carbon in
2 the coastal ocean of Southeast Asia

3

4 Yongli Zhou^{1,*}, Moritz Müller², Nagur Cherukuru³, Patrick Martin^{1,*}

5

6 ¹Asian School of the Environment, Nanyang Technological University, 639798 Singapore

7 ²Faculty of Engineering, Computing and Science, Swinburne University of Science and
8 Technology, 93350 Kuching, Sarawak, Malaysia

9 ³CSIRO Oceans and Atmosphere Flagship, Canberra ACT 2601, Australia

10 †Current address: the Ecosystems Center, Marine Biological Laboratory, Woods Hole, 02543,
11 United States

12

13 Email:

14 Yongli Zhou*: zhou0303@e.ntu.edu.sg

15 Moritz Müller: mmueller@swinburne.edu.my

16 Nagur Cherukuru: Nagur.Cherukuru@csiro.au

17 Patrick Martin*: pmartin@ntu.edu.sg

18 *Corresponding author(s)

19

20

21

22 **Abstract**

23 The terrigenous dissolved organic carbon (tDOC) exported from the peatlands in Southeast
24 Asia appears to be extensively remineralized in the shelf sea, but the processes that drive this
25 remineralization remain unclear. Here, we combined incubation experiments and model
26 simulations to quantify the rate and extent of photodegradation of tDOC in the Sunda Shelf
27 Sea. Laboratory photodegradation experiments indicate that up to 74% of the peatland tDOC
28 is potentially labile to photochemical remineralization. Based on our estimated apparent
29 quantum yield for tDOC remineralization, modeled *in-situ* solar irradiance, and measured
30 inherent optical properties of the water column, we simulated peatland tDOC
31 photoremineralization for two coastal regions of the Sunda Shelf Sea. These simulation
32 results show that natural solar radiation can directly remineralize $20\pm 11\%$ of tDOC over 2
33 years, which corresponds to the approximate residence time of water in the Sunda Shelf Sea,
34 and that significant photobleaching of tDOC can occur in coastal waters over shorter
35 time-scales. We further derived a simplified photochemical decay constant ϕ^{ref} of 0.008–
36 0.017day^{-1} for Southeast Asia's peatland-derived tDOC, which can be used to parameterize
37 the recently proposed UniDOM model framework. We conclude that direct photodegradation
38 may be a greater sink for tDOC in Southeast Asia's coastal ocean compared to higher
39 latitudes, although it is insufficient to account for the total tDOC remineralization observed in
40 the Sunda Shelf Sea.

41

42

43 **Plain Language Summary**

44 Tropical peatlands in Southeast Asia are contributing large quantity of organic carbon to the
45 coastal ocean. This organic carbon flux is rapidly decomposed to CO₂ but the mechanism of
46 this extensive remineralization is unclear. Organic carbon from peatlands appears to be easily
47 decomposed upon exposure to sunlight, known as photodegradation. In this study, we
48 conducted incubation experiments to collect data of photochemical decay efficiency of
49 peatland-derived organic carbon and developed model simulation to calculate, in natural
50 coastal waters, how much of the organic carbon is decomposed via the pathway of
51 photodegradation. Our data show that sunlight radiation can directly cause a loss of 20% of
52 the peatland-derived organic carbon input in the coastal ocean of Southeast Asia, indicating
53 that photodegradation contribute to a larger portion of the total organic carbon decomposition
54 in Southeast Asia than in coastal oceans at the higher latitudes. In addition, our data allowed
55 us to derive region-specific decay rates of photodegradation for coastal ocean of Southeast
56 Asia, which can be used to parameterize large-scale aquatic organic carbon biogeochemistry
57 model.

58

59

60

61

62

63

64 **1 Introduction**

65

66 The biogeochemical fate of terrigenous dissolved organic carbon (tDOC) in the ocean is still
67 poorly understood. This is important in the context of the global carbon cycle, because the
68 riverine input and the biogeochemical processing of tDOC can have significant impacts on
69 coastal marine environments. Intact tDOC can absorb sunlight and lead to ecologically
70 harmful “coastal darkening” by shoaling the euphotic zone and altering the spectral quality of
71 light underwater (Aksnes et al., 2009; Martin et al., 2021; Urtizberea et al., 2013). Moreover,
72 a significant fraction of tDOC may undergo remineralization in shelf seas, as shown for the
73 Eurasian Shelf (Kaiser et al., 2017), the North Sea (Painter et al., 2018), the Louisiana Shelf
74 (Fichot & Benner, 2014), and the Sunda Shelf (Wit et al., 2018; Zhou et al., 2021). In some
75 regions, remineralization of tDOC is sufficiently large to cause ocean acidification
76 (Semiletov et al., 2016; Wit et al., 2018; Zhou et al., 2021) and to drive strong sea-to-air CO₂
77 fluxes (Cai, 2011; Kitidis et al., 2019; Wit et al., 2018; Zhou et al., 2021). However, the
78 *in-situ* rates and extent of tDOC degradation that control these environmental impacts remain
79 poorly constrained.

80

81 The degradation of tDOC is influenced by its optical properties. Rich in colored dissolved
82 organic matter (CDOM) (Massicotte et al., 2017), tDOC can absorb ultraviolet and visible
83 solar radiation (Zepp, 2007). Meanwhile, the abundant unsaturated bonds of the tDOC pool
84 are subject to cleavage upon absorbing radiant energy, leading to a series of photochemical

85 reactions (Zika, 1981). These reactions can cause removal of CDOM (i.e., photobleaching)
86 (Helms, Stubbins, et al., 2013; Tzortziou et al., 2007), complete oxidation of tDOC into CO₂
87 (i.e., photo-remineralization) (Allesson et al., 2021; Mopper et al., 1991; Moran et al., 2000),
88 and chemically alter tDOC molecules (i.e., photo-modification) in a way that renders them
89 more labile to microbial degradation (Dittmar et al., 2007; Stubbins et al., 2010, 2017). The
90 findings that tDOC derived from peatlands of the Congo Basin (Spencer et al., 2009;
91 Stubbins et al., 2010) and of Southeast Asia (Martin et al., 2018; Zhou et al., 2021) is highly
92 photo-labile imply that photodegradation can play an important role in the biogeochemical
93 cycling of tropical peatland tDOC.

94

95 Recently, Aarnos et al. (2018) estimated that direct photo-remineralization can cause a loss of
96 18% of the global riverine tDOC flux in the ocean, based on the relationship between tDOC
97 loss and CDOM loss derived from incubation experiments, and the assumption that all
98 riverine CDOM is photochemically destroyed. However, quantification of the *in-situ* rates
99 and the extent of tDOC photodegradation via realistic modeling is challenging because it
100 requires data for the inherent photochemical properties of the tDOC (i.e., photo-lability and
101 apparent quantum yield), the *in-situ* solar irradiance, and the underwater light field; this
102 requires combining data from incubation experiments, field measurements, satellite
103 observations and meteorological models. To date, such modelling has only been performed in
104 a few cases, such as the Louisiana Shelf (Fichot & Benner, 2014) and the Baltic Sea (Aarnos
105 et al., 2012). Fichot & Benner (2014) concluded that direct photo-remineralisation only

106 consumes 8% of the riverine tDOC input. In contrast, Aarnos et al. (2012) found that the
107 annual DOC photoremineralization exceeds the riverine DOC supply in the Baltic, and
108 concluded that photoremineralization is likely an important tDOC sink in the Baltic Sea.
109 However, for most shelf sea regions we have little understanding of *in-situ* tDOC
110 photo-remineralization, which limits our ability to predict how anthropogenically driven
111 changes to tDOC fluxes might impact coastal ecosystems (Ciais et al., 2013). Although
112 modeling frameworks are being developed to represent the biogeochemistry of tDOC across
113 the land-ocean aquatic continuum (Anderson et al., 2019) and to integrate coastal carbon
114 cycling processes in global ocean models (Mathis et al., 2022), appropriate rate constants for
115 tDOC remineralization are still very poorly constrained.

116

117 In this study, we attempt to estimate *in-situ* photodegradation rates for one of the world's
118 hotspots of riverine tDOC export: Southeast Asia. Rivers draining the peatlands in this region
119 deliver ~21 Tg C of tDOC to the Sunda Shelf Sea annually, which could account for ~10% of
120 the global fluvial tDOC flux (Baum et al., 2007; S. Moore et al., 2011). It appears that at least
121 60–70% of this peatland-derived tDOC is rapidly remineralized in the Sunda Shelf Sea after
122 estuarine mixing (Wit et al., 2018; Zhou et al., 2021). Photodegradation might play an
123 important role here because Southeast Asia's peatland tDOC appears to be highly photo-labile
124 (>70% photo-remineralizable) (Martin et al., 2018; Zhou et al., 2021) but much less
125 bio-labile (Nichols & Martin, 2021). In addition, because of the greater solar irradiance
126 year-round in the tropics (Apell & McNeill, 2019), photodegradation might be a stronger

127 tDOC sink in the Sunda Shelf Sea compared to higher latitudes.

128

129 We incubated riverine and shelf water samples with simulated sunlight to determine the
130 photo-degradability and photochemical efficiency (apparent quantum yield) of tDOC
131 remineralization. We then developed a spectrally resolved optical model based on previous
132 work (Aarnos et al., 2012, 2018; Fichot & Benner, 2014) to estimate the *in-situ* rates and
133 extent of tDOC photo-remineralization, and CDOM photobleaching, for two coastal regions
134 of the Sunda Shelf Sea. We further used our results to estimate a simplified photochemical
135 decay constant that can be applied in ocean biogeochemical models using the recently
136 proposed Unified Model of Dissolved Organic Matter model (Anderson et al., 2019). This
137 will assist to integrate tDOC processing into larger-scale carbon cycle models, especially in
138 Southeast Asia.

139

140

141 **2 Materials and Methods**

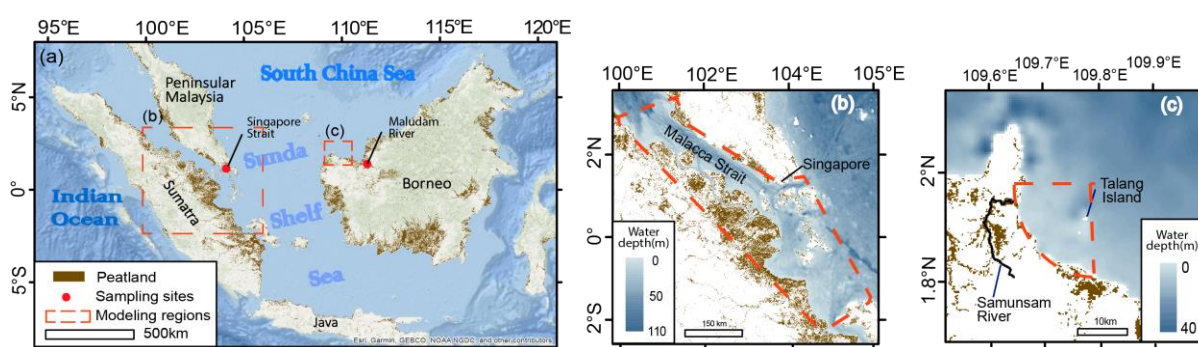
142 **2.1 Overview of study area**

143 Southeast Asia's peatlands are found mainly in the coastal lowlands of Sumatra and Borneo
144 (Fig. 1a). The peat-draining rivers deliver tDOC into the Sunda Shelf Sea, where the oceanic
145 currents and movement of tDOC are controlled by the monsoon (Mayer et al., 2018; Susanto
146 et al., 2016). During the Northeast Monsoon (November to February), water flows from the
147 South China Sea into the central shelf sea and flows towards the Java Sea and the Malacca

148 Strait; during the Southwest Monsoon (May to August), the currents reverse and carry the
149 tDOC input from the Sumatran rivers into the central Sunda Shelf. After a residence for 1–2
150 years in the shelf sea, the tDOC exits into the open Indian Ocean through the Malacca Strait,
151 the Sunda Strait, or the Lombok Strait.

152

153



154

155 Figure 1. (a) Distribution of peatlands in Southeast Asia and locations of water sampling sites
156 (the Maludam River and the Singapore Strait) and modeling regions. (b) – (c) Red dashed
157 lines encircle the modeling regions, with bathymetry shown: (b) the Southern Malacca Strait
158 (receives input from the Sumatran peatlands) and (c) the Talang Region (receives tDOC input
159 from the Samunsam River). Peatland distribution was obtained from the Center for
160 International Forestry Research, Indonesia (<https://www2.cifor.org/global-wetlands/>).
161 Bathymetry data were obtained from the GEBCO_2020 grid (GEBCO Compilation Group,
162 2020).

163

164 2.1.1 Sampling sites and water collection for photodegradation experiments

165 To obtain photochemical data of peatland tDOC, we collected two surface water samples (0–

166 1 m depth) from the Maludam River (1.636°N 111.049°E) in Sarawak, Borneo in December
167 2017 and June 2019 and one from the Singapore Strait (1.226°N, 103.860°E) in the coastal
168 Sunda Shelf Sea in July 2020 (Figure 1). The Maludam River samples were gravity-filtered
169 through pre-rinsed 0.22 μm pore-size Whatman Polycap filters on the day of collection and
170 filtered again through pre-rinsed 0.22 μm pore-size polyethersulfone membrane filters upon
171 arrival at Nanyang Technological University, Singapore. The Singapore Strait shelf water
172 sample was filtered through pre-rinsed 0.22 μm pore-size polyethersulfone membrane filters
173 on the day of collection. All filtered water samples were kept at 4°C in the dark and filtered
174 again through pre-rinsed 0.22 μm pore-size polyethersulfone membrane filters before
175 experiments.

176
177 Samples from these two sites are representative of the tDOC exported from peatlands into our
178 modeling regions of the coastal ocean, because multiple lines of evidence suggest that the
179 underlying optical and photochemical characteristics of tDOC are similar across the peatlands
180 of Southeast Asia. The Maludam River drains one of the largest remaining intact peatlands in
181 Malaysia, and its catchment consists exclusively of peatlands (Müller et al., 2015). The
182 Maludam samples therefore allow us to obtain AQY estimates for tDOC that is freshly
183 released from a peatland, and that are not influenced by contributions of DOC from other soil
184 types or anthropogenic input. In contrast, the Singapore Strait receives substantial tDOC
185 input from Sumatran peatlands between May and September when tDOC comprises ~50% of
186 the bulk DOC pool, but this tDOC has already undergone fairly extensive remineralization

187 prior to reaching the Singapore Strait (Zhou et al. 2021). This allows us to estimate the AQY
188 for peatland tDOC that has already undergone some degree of biogeochemical processing in
189 the shelf sea. As a purely peatland-draining river, the Maludam has high DOC concentrations
190 (3000–4000 $\mu\text{mol l}^{-1}$). Although different rivers across Sumatra and Borneo can vary around
191 10-fold in DOC concentration, the DOC concentration is linearly related to the proportion of
192 catchment area that is peatland (Rixen et al., 2022). Moreover, across multiple rivers in
193 northwestern Borneo draining catchments with varying peatland proportions and DOC
194 concentrations, there is a strong and linear relationship between DOC concentration and
195 CDOM absorption (Fig. S1, data from (Martin et al., 2018)). This suggests that the
196 concentration of tDOC varies according to the extent of peatland cover in a catchment, but
197 that the optical properties of the tDOC pool are then very similar across rivers, including the
198 Maludam. In addition, the stable carbon isotope composition of DOC ($\delta^{13}\text{C}_{\text{DOC}}$) is very
199 similar across peatland-draining rivers on Sumatra, Borneo, and Peninsular Malaysia, mostly
200 between -28‰ and -30‰ (data compiled in (Zhou et al., 2021)), and these peatlands share
201 many similarities in plant species (Giesen et al., 2018) and climatic conditions. This further
202 suggests that the photochemical and optical characteristics of the peat-derived tDOC pool
203 should be similar between rivers across the region. This is also supported by our data (see
204 below) that the photochemical efficiency (i.e., apparent quantum yield) of DOC is similar
205 between the Singapore Strait water and the Maludam River water.

206

207

208 **2.1.2 Modeling regions**

209 Using our experimental data, we simulated photo-remineralization of tDOC and
210 photobleaching of CDOM for two regions of the Sunda Shelf Sea: the southern Malacca
211 Strait and the Talang Region in Sarawak, Borneo (Fig. 1). Selection of the modeling regions
212 was based on the following considerations. First, both regions receive large riverine input of
213 tDOC from peatlands (Martin et al., 2018; Wit et al., 2018; Zhou et al., 2019, 2021). Second,
214 previous work has indicated the possibility of a significant contribution of photodegradation
215 in both regions: it potentially drives a major part of the tDOC remineralization observed in
216 the shelf sea (Zhou et al., 2021) and the removal of terrigenous CDOM (Kaushal et al., 2021).
217 Third, measurements of the water column inherent optical properties (i.e., particulate
218 absorption and backscattering) are available for both regions (Cherukuru et al., 2021; Martin
219 et al., 2021).

220

221 We ran simulations over different durations for the two regions to accomplish two different
222 objectives. The simulation for the southern Malacca Strait aimed to quantify the contribution
223 of photodegradation to the total quantity of tDOC remineralization observed in this region of
224 the shelf sea, where the water residence time is up to approximately 2 years (Mayer et al.,
225 2015). In contrast, the simulation for the Talang Region aimed to test whether photobleaching
226 of tDOC is sufficiently rapid to contribute to the seasonal variability of CDOM observed at
227 the Talang Islands (Kaushal et al., 2021), where the water residence time is much shorter
228 (Mayer et al., 2015).

229

230 The southern Malacca Strait encompasses the shelf waters near the largest peatland area on
231 Sumatra, including the southern part of the Malacca Strait, the Singapore Strait, and the
232 waters to the north of Bangka Island, Indonesia (Fig. 1b). It receives substantial terrestrial
233 input from the Sumatran peatlands by riverine runoff, and it was found that 60–70% of the
234 tDOC is remineralized on the shelf (Wit et al., 2018; Zhou et al., 2021). Based on the water
235 residence time of 1–2 years within this region of the Sunda Shelf (Mayer et al., 2015), we
236 simulated photodegradation for 2 years to quantify a likely upper boundary for the
237 photochemical contribution to the total quantity of tDOC remineralization.

238

239 Waters in the Talang Region in Sarawak receive peatland tDOC input carried by the
240 Samunsam River (Fig. 1c). Skeletal luminescence in a coral core from the Talang Island
241 showed seasonal variability terrigenous CDOM levels, with very low values during the
242 Southwest Monsoon (May to August) (Kaushal et al., 2021). This seasonal decrease in the
243 CDOM signal in coral skeletons was argued to be greater than the expected seasonal decrease
244 in the riverine CDOM flux, but closely matched the seasonal changes in solar irradiance
245 (higher during Southwest Monsoon, Fig. S2d). This might indicate a significant role for
246 photodegradation in removing more tDOC and CDOM in the coastal waters during
247 Southwest Monsoon (Kaushal et al., 2021). To test this hypothesis, we estimated the
248 photo-remineralization and photobleaching for different periods of the year.

249

250

251 **2.2 Photodegradation experiments for AQY determination**

252 We performed four photodegradation experiments (Exp 1, 2, 3, and 4 below, Table 1) with the
253 water samples from the Maludam River and the Singapore Strait. The changes in DOC
254 concentration and CDOM during Exp 1 and Exp 3 were reported previously (Zhou et al.,
255 2021). Here, we use the data further to calculate the AQY.

256

257 In Exp 1, we aimed to quantify the proportion of the peatland-derived tDOC that is
258 photo-remineralizable and to calculate the AQY. We incubated the Maludam sample collected
259 in December 2017 with simulated sunlight, monitored the DOC concentration and CDOM
260 absorption over time, and terminated the experiment when no additional DOC loss was
261 observed (after 816 hours). However, photo-flocculation of DOC was observed at 525 hours,
262 so we only used the data up until the previous time point at 416 hours to calculate the AQY.

263

264 In Exp 2, we aimed to quantify the AQY after simulating the mixing of tDOC into the coastal
265 ocean. We diluted 65 ml of the Maludam sample collected in June 2019 with 935 ml of
266 artificial seawater (0.2 g NaHCO₃ [Sigma-Aldrich S6014] and 32.09 g NaCl [Sigma-Aldrich
267 S9888] in 1 L ultrapure deionized water [18.2 MΩ cm⁻¹]), achieving a salinity of ~29. We
268 exposed the mixed sample to simulated sunlight, monitored the changes in DOC and CDOM,
269 and terminated the experiment after >25% of DOC was lost (462 hours).

270

271 In Exp 3, we aimed to quantify the proportion of tDOC in the shelf water that was still
 272 photo-remineralizable after it had already experienced extensive prior degradation in the
 273 environment (Zhou et al., 2021). We incubated the Singapore Strait sample with simulated
 274 sunlight until no additional DOC loss was observed, which was after 500 hours. Because we
 275 previously found that a marine DOC-dominated sample of shelf seawater from Singapore
 276 Strait (sample collected in January when there was little tDOC input) showed no
 277 photochemical loss of DOC (Fig. 7i in Zhou et al. 2021), the loss of DOC observed in Exp 3
 278 was attributed entirely to photochemical loss of tDOC.

279

280 In Exp 4, we aimed to further constrain the AQY of tDOC with a spectrally resolved
 281 experiment. We incubated the Maludam sample collected in June 2019 with simulated
 282 sunlight under Schott long-pass filters with cut-offs at 295nm, 320nm, 395nm, 420nm, and
 283 455nm. We terminated the experiment after 144 hours, once the DOC and CDOM loss were
 284 sufficiently large to calculate the AQY.

285

286

287 Table 1. Summary of the four photodegradation experiments.

	Sample	Duration (hour)
Exp 1	Maludam River water (Dec 2017)	416
Exp 2	Maludam River water (June 2019) diluted with artificial seawater	462

Exp 3	Shelf water during tDOC input (July 2020)	500
Exp 4	Maludam River water (June 2019) with optical cut-off filters	144

288

289

290 In all four experiments, water samples (30 ml) were filled into 14 replicate cylindrical quartz
 291 cells (Starna Cells, 50 mm pathlength, 50 mm diameter, with Teflon screw caps) and
 292 irradiated in an Atlas Suntest CPS+ solar simulator with a daylight optical filter with
 293 integrated irradiance of 40 W m⁻² between 300–400 nm; the chamber temperature was
 294 fan-cooled to below 40°C (the lowest-possible temperature setting). The vertical walls of the
 295 quartz cells and bottom of the chamber were covered with black cardboard. A dark control
 296 sample was placed in the chamber in a glass bottle wrapped in aluminum foil. At regular time
 297 intervals, one or two of the 14 replicates were sacrificed to measure DOC and CDOM to give
 298 a time series for each experiment. The long total duration of our experiments was designed
 299 for our specific goal of quantifying what proportion of an initial input of tDOC is
 300 photo-remineralized cumulatively over its residence time of up to 2 years in the shelf sea (see
 301 Section 2.5). We therefore needed the AQY that corresponds to a similar proportion of tDOC
 302 loss to what the model ultimately predicts (which is around 20%, Section 3.3), but not the
 303 initial AQY determined from very short exposure times (which would be needed to predict
 304 instantaneous daily rates of photochemical CO₂ production, which is not our objective).
 305 Because each experiment yielded a time series of DOC and CDOM loss we could also test

306 whether the AQY changed systematically over time, which was not the case.

307

308 The irradiance spectrum of the solar simulator was measured with an Ocean Insights FLAME

309 radiometer from 177 nm to 872 nm at 1 nm resolution. We conducted nitrite actinometry

310 following Jankowski et al. (1999) using the same experimental conditions as for our tDOC

311 samples, and found <6% difference between measured and predicted salicylic acid production

312 (Table S1). This showed that the irradiance measured by the radiometer and used for our

313 AQY determination provided an accurate estimate of the irradiance received by our tDOC

314 samples.

315

316 **2.3 Sample analysis**

317 CDOM absorbance was measured from 230 – 900 nm at room temperature on a Thermo

318 Evolution300 dual-beam spectrophotometer against ultrapure deionized water as a reference

319 using quartz cuvettes with pathlengths of 2, 10 or 100 mm, depending on sample absorbance.

320 The spectra were baseline-corrected, smoothed, and converted to Napierian absorption

321 coefficients using the R package hyperSpec (Beleites & Sergio, 2012). We report the

322 absorption coefficient at 350 nm (a_{350}) as a measure of the CDOM concentration. The

323 spectral slope between 275–295 nm ($S_{275-295}$) and the specific ultraviolet absorption at 254

324 nm ($SUVA_{254}$) were used as proxies for DOC apparent molecular weight (Helms et al., 2008)

325 and aromaticity (Weishaar et al., 2003), respectively.

326

327 DOC samples (30 ml) were acidified with 100 μl 50% H_2SO_4 and analyzed on a Shimadzu
328 TOC-L system with a high-salt combustion kit as previously described in Zhou et al. (2021).
329 The analytical accuracy was monitored using deep-sea water certified reference material
330 (CRM) (42–45 $\mu\text{mol L}^{-1}$ DOC, University of Miami, USA; long-term mean and standard
331 deviation were $48.0 \pm 3.9 \mu\text{mol L}^{-1}$).

332

333 **2.4 Apparent quantum yield calculations**

334 The apparent quantum yield (AQY) can be reported either as a broadband AQY or a
335 spectrally resolved AQY. The broadband AQY is a single value representing the quantity of
336 lost reactant divided by the number of absorbed photons across a specific wavelength range
337 (between 290 and 700 nm in this study), so it shows the “average” photochemical efficiency
338 across this wavelength range. However, the photochemical efficiency varies spectrally. Hence,
339 the spectrally resolved AQY is also frequently reported (Aarnos et al., 2018; Vähätalo et al.,
340 2000, 2003; Zepp, 2007). We calculated both the broadband and spectrally resolved AQY for
341 tDOC and CDOM as summarized below (full details in the Supporting Information).

342

343 The spectrally resolved AQY for tDOC photo-remineralization, $\phi_{DOC}(\lambda)$, was assumed to
344 decrease exponentially with increasing wavelength λ (Gao & Zepp, 1998; Koehler et al.,
345 2022; Vähätalo et al., 2000):

$$346 \quad \phi_{DOC}(\lambda) = c e^{-d\lambda} \quad (1)$$

347 where c ($\text{mol C (mol photons)}^{-1} \text{ nm}^{-1}$) and d (nm^{-1}) are positive constants. Because the

348 quantity of photo-remineralized DOC is the product of AQY and the number of absorbed
349 photons $\Xi(\lambda)$:

$$350 \quad \Delta DOC = \int_{300nm}^{700nm} \phi_{DOC}(\lambda) \Xi(\lambda) d\lambda \quad (2),$$

351 the constants c and d of $\phi_{DOC}(\lambda)$ can be optimized by iteration until the smallest difference
352 between the left (i.e., the measured DOC loss after irradiation) and the right side (i.e., the
353 predicted DOC loss) of Eqn. 2 is reached. For Exp 1, 2 and 3, the AQY was optimized using
354 data of a single irradiance spectrum and a single value of measured DOC loss following
355 Aarnos et al. (2018) and Aarnos et al. (2012). For Exp 4 where multiple spectral treatments
356 were applied, the AQY was optimized when the smallest sum of squared error between the
357 predicted and the measured DOC loss of all spectral treatments was achieved following
358 Powers et al. (2017). We note that in cases where only a single measurement of DOC loss is
359 available (i.e. Exp 1–3), the shape of the calculated AQY spectrum is sensitive to the choice
360 of starting values for constant c . We selected a starting value of 1.0 following Aarnos et al.
361 (2012, 2018), but we also performed a sensitivity analysis in which we repeated our AQY and
362 model calculations using starting values for c of 0.01 and of 100.

363

364 To also model the photobleaching of CDOM, we extended the concept of AQY to the light
365 dose-dependent decrease in CDOM absorption. We refer to this as $\phi_{CDOM}(\lambda)$, which is the
366 spectrally resolved AQY for the decrease in the volume-integrated CDOM absorption
367 coefficient, with units of $L m^{-1} (mol photons)^{-1} nm^{-1}$. We assumed that $\phi_{CDOM}(\lambda)$ resembles
368 $\phi_{DOC}(\lambda)$, decreasing exponentially with increasing wavelength λ :

369
$$\phi_{CDOM}(\lambda) = c' e^{-d'\lambda} \quad (3)$$

370 where c' ($L m^{-1} nm^{-1}$) and d' (nm^{-1}) are positive constants. Similar to DOC, the quantity of
371 lost CDOM is the product of AQY and number of absorbed photons $\Xi(\lambda)$:

372
$$\Delta CDOM = \int_{300nm}^{700nm} \phi_{CDOM}(\lambda) \Xi(\lambda) d\lambda \quad (4),$$

373 so the constants c' and d' of $\phi_{CDOM}(\lambda)$ were optimized by iteration until the smallest
374 difference between the left and the right side of Eqn. 4 was reached. The quantity of CDOM
375 is measured as the absorption coefficient times the sample volume, we therefore calculated
376 the AQY in terms of the measured decrease in absorption coefficient across the CDOM
377 absorption spectrum at 1-nm resolution from 250–700 nm. For Exp 1 – 3, we used a single
378 irradiance spectrum for the calculation of AQY; for Exp 4, we used the data from multiple
379 spectral treatments for the calculation of AQY. These calculations are essentially the same as
380 for DOC, but were carried out at every wavelength at which CDOM absorption was
381 measured (from a_{250} to a_{700}) and then concatenated, yielding spectrally-resolved AQY across
382 the CDOM absorption spectrum.

383

384 **2.5 Model simulation of tDOC photodegradation**

385 **2.5.1 Model overview**

386 Our model calculates the daily changes in tDOC concentration and CDOM absorption caused
387 by solar radiation for both regions. Our modeling approach was modified from Fichot &
388 Benner (2014) and Fichot & Miller (2010), but using spectrally resolved AQY as in (Koehler
389 et al., 2022) and extended to explicitly quantify the decrease in CDOM absorption due to

390 photobleaching. This allows a more accurate calculation of the number of absorbed photons
391 as the CDOM absorption decreases over time. The modeling approach is summarized in Fig.
392 2 and below, and is explained in detail in the Supporting Information.

393

394 Our model iteratively calculates (i) hourly solar irradiance just below the water surface based
395 on the above-water irradiance and solar zenith angle, (ii) underwater light attenuation, (iii)
396 daily total number of absorbed photons based on the real-time CDOM absorption, light
397 attenuation and water depth, (iv) daily decrease in DOC concentration and CDOM absorption
398 based on the total absorbed photons over 24 hours and the AQY, and (v) the DOC
399 concentration and CDOM absorption at the end of the day.

400

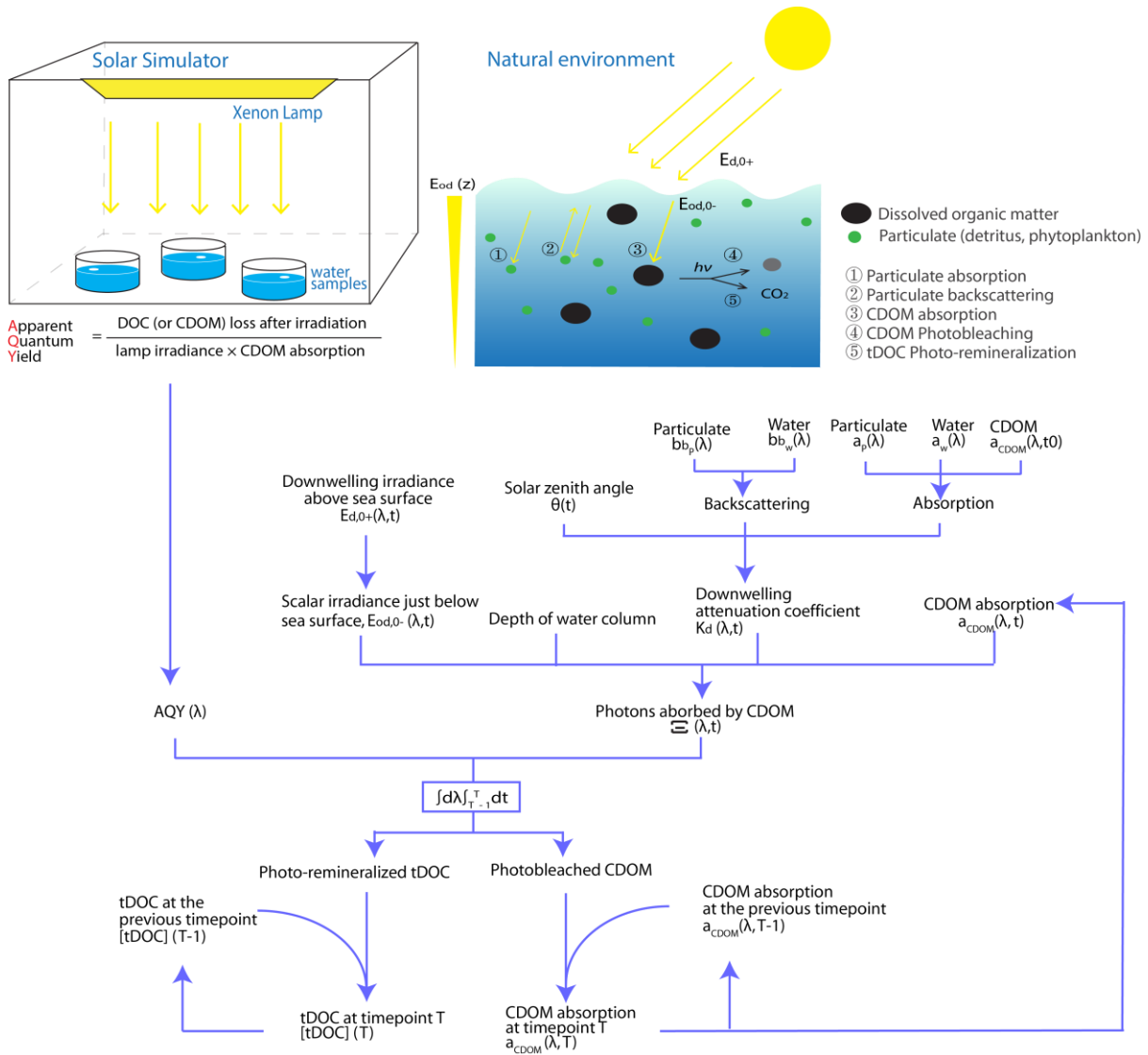
401 The model simulation was performed first using cloud-corrected solar irradiance to estimate
402 the most realistic photodegradation rates and extent, and then using clear-sky solar irradiance
403 to estimate the maximum possible extent of photodegradation. The uncertainty was estimated
404 by a Monte Carlo approach, where all input parameters were perturbed with a 1σ normally
405 distributed error, the model was recalculated 1,000 times, and the standard deviation of the
406 model outputs was then taken as the estimated uncertainty.

407

408 We used the spectrally resolved AQY calculated from our experimental data for the model
409 simulation, but we also ran the simulation using the broadband AQY for comparison. As we
410 discuss in Section 4.2, using the broadband AQY for our simulation appears to lead to a

411 significant overestimate of tDOC photoremineralization because of the spectral change in
 412 underwater irradiance with depth.

413



414

415 Figure 2. Schematic diagram of the model structure for photodegradation simulation. Input

416 variables, parameters, modeling steps, and the model output are shown here. Time-dependent

417 input variables are labeled with a time variable t . Variables are defined in Table S2.

418

419

420
421
422
423
424
425
426
427
428
429
430
431
432
433
434
435
436
437
438
439
440

2.5.2 Model input

We used the mean and standard deviation ($\pm 1SD$) of the four AQY spectra from Exp 1–4 as the model input AQY and its uncertainty, respectively. We obtained the hourly above-water solar irradiance for each month for both modeling regions from the Tropospheric Ultraviolet and Visible Radiation Model (TUV model), US National Center for Atmospheric Research, which were then converted to the irradiance just below the water surface following Fichot and Miller (2010) (Supporting Information). The mean water depth is 19.7 m for the Southern Malacca Strait area and 7.6 m for the Talang region, based on the GEBCO bathymetry (GEBCO Compilation Group, 2020). The areas of the two modeling regions for calculating the mean water depth are shown in Fig. 1b–c. The starting values (i.e., Day 0 values) of tDOC concentration and CDOM absorption were calculated by a two-endmember mixing model using the appropriate riverine endmember data from Wit et al. (2018) and Martin et al. (2018) for the two regions and marine endmember data from Zhou et al. (2021) (Supporting Information). The *in-situ* particulate absorption and backscattering data measured in the Singapore Strait and from the Talang Region were obtained from Martin et al. (2021) and Cherukuru et al. (2021), respectively, and were processed into spectra with 1-nm resolution (Supporting Information). The *in-situ* solar irradiance in each month, initial CDOM spectra (i.e., Day 0) and the particulate absorption and backscattering spectra with their associated

441 uncertainties are shown in Fig. S3 for both modeling regions. In particular, the Talang Region
442 showed pronounced seasonality in solar irradiance – the greater cloud cover during the NE
443 Monsoon (November to January) drives a decrease in the solar irradiance during that period.

444

445

446 **2.5.3 Photochemical decay constant for UniDOM**

447 Anderson et al. (2019) recently proposed the UniDOM framework to model large-scale tDOC
448 biogeochemical processing along the aquatic continuum. The photodegradation component of
449 UniDOM requires a maximum photochemical decay constant, ϕ^{ref} , which defines the
450 photo-remineralization rate of tDOC at the water surface, as the model input. The ϕ^{ref} is a
451 function of the tDOC photochemical properties and thus is region-specific. We calculated the
452 ϕ^{ref} for our two regions based on our modeling results. We first calculated the
453 depth-normalized photochemical decay constant, ϕ , based on the modeled loss of DOC over
454 time and then converted the ϕ to ϕ^{ref} based on equations in Anderson et al. (2019). Details
455 are given in Supporting Information.

456

457

458 **3 Results**

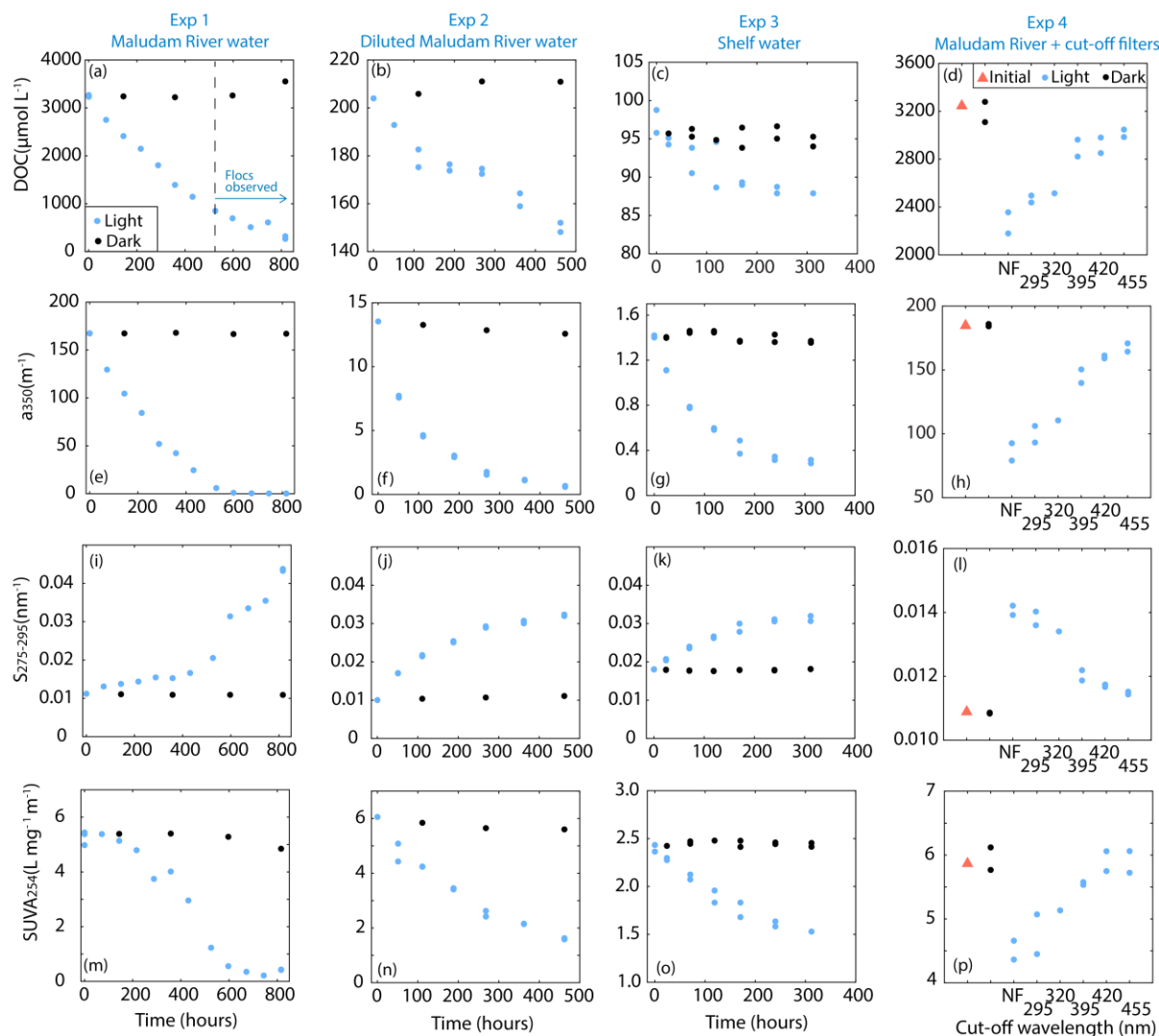
459 **3.1 Photodegradability of peatland-derived tDOC**

460 In all four experiments, we observed loss of DOC and CDOM (as absorption at 350nm, a_{350})
461 upon irradiation, but to different extents (Fig. 3). In Exp 1, flocs were observed at 525 h,

462 suggesting that some DOC was photo-flocculated (Chen et al., 2014; Helms, Mao, et al.,
 463 2013) rather than photo-remineralized; we therefore only used the data up to 416 h. The
 464 Maludam River water samples showed a greater loss of DOC (26–74% loss) compared to the
 465 shelf water sample (9% loss) despite similar duration of irradiation, but they both showed a
 466 near-complete removal of CDOM (Fig. 3 & Table S3). In Exp 4, greater loss of DOC and
 467 CDOM was observed in the spectral treatments with lower cut-off wavelengths.

468

469



470

471 Figure 3. Changes in DOC concentration and CDOM absorption over time (Exp 1,2, and 3)

472 and upon irradiation by different wavelength ranges (Exp 4). In Exp 4, the irradiance below
473 the respective cut-off wavelengths was blocked. *NF*: no optical cut-off filter was used.

474

475 In all experiments, the CDOM spectral slope between 275 nm and 295 nm ($S_{275-295}$) increased
476 while the DOC-specific absorbance at 254 nm ($SUVA_{254}$) decreased (Fig. 3 & Table S3),
477 indicating that compounds with high apparent molecular weight and aromatic moieties were
478 preferentially removed upon irradiation (Helms et al., 2008; Weishaar et al., 2003). In Exp 4,
479 the extent of these changes was greater in treatments exposed to lower wavelengths.

480

481 **3.2 Apparent quantum yield**

482 The broadband AQY was 42–95 $\mu\text{mol C (mol photons)}^{-1}$ for the Maludam River (Exp 1, 2,
483 and 4) and 85 $\mu\text{mol C (mol photons)}^{-1}$ for the shelf seawater tDOC from the Singapore Strait
484 (Exp. 4), which had experienced prior degradation. The AQY did not show a decreasing trend
485 over the course of the experiments (Table S4). Fig. 4a shows the individual AQY spectra for
486 DOC photo-remineralization that we calculated from Exp 1–4, and the mean spectrum. Some
487 previous studies report the AQY at 330 nm irradiance, $\phi_{DOC}(330nm)$, for comparison of the
488 photochemical efficiency between samples. From our data, the $\phi_{DOC}(330nm)$ was 129 –
489 440 $\mu\text{mol C (mol photons)}^{-1}$ for peatland tDOC from the Maludam River, and 200 $\mu\text{mol C}$
490 $(\text{mol photons})^{-1}$ for the tDOC in the shelf water from the Singapore Strait. To verify that the
491 optimization procedure for calculating spectrally resolved AQY was successful, we used the
492 calculated spectrally resolved AQY with the irradiance spectrum of the solar simulator to

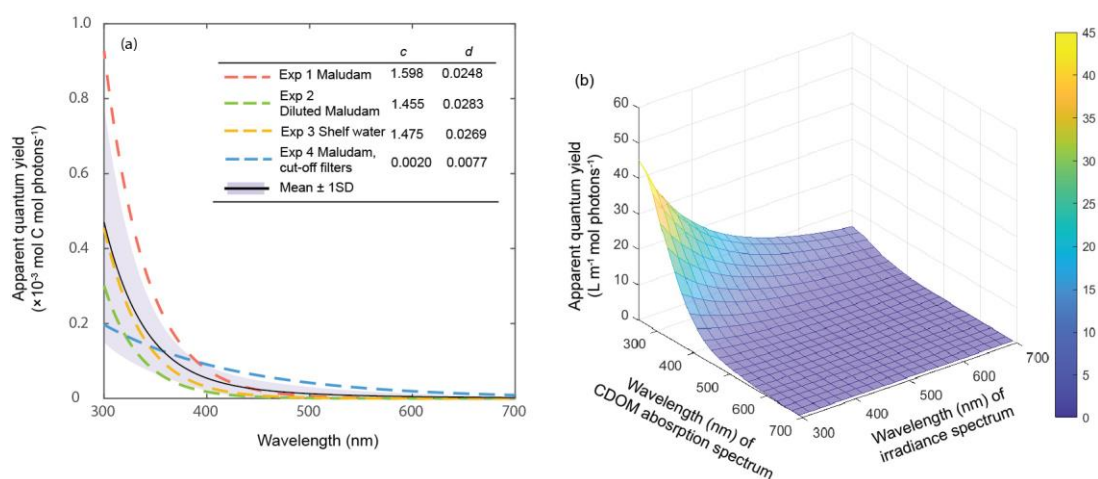
493 predict DOC loss, which well reproduced the DOC loss measured in our all four experiments
494 (Fig. S4).

495
496 The corresponding AQY spectra for CDOM photobleaching ($\phi_{CDOM}(\lambda)$) are shown in Fig. S2,
497 and the mean spectrum is shown in Fig. 4b. At any given irradiance wavelength, the AQY
498 was higher at shorter wavelengths of the CDOM absorption spectrum. In other words, one
499 mole of photons at a given irradiance wavelength causes a larger decrease in CDOM
500 absorption at a shorter absorption wavelength (for instance, a_{300}) compared to at a longer
501 absorption wavelength (for instance, a_{350}). At any given CDOM absorption wavelength, the
502 AQY decreases exponentially with increasing irradiance wavelength.

503

504

505



506
507 Figure 4. Spectrally resolved apparent quantum yield for (a) tDOC photo-remineralization
508 and (b) CDOM photobleaching (i.e. the AQY for reducing the volume-integrated absorption
509 coefficient). In (a), the individual data from Exp 1–4 are shown together with the mean

510 spectrum and its standard deviation. In (b), only the mean spectrum is shown for clarity, but
511 the standard deviation of the CDOM photobleaching AQY is included in Supplementary Data
512 Set 1.

513

514

515

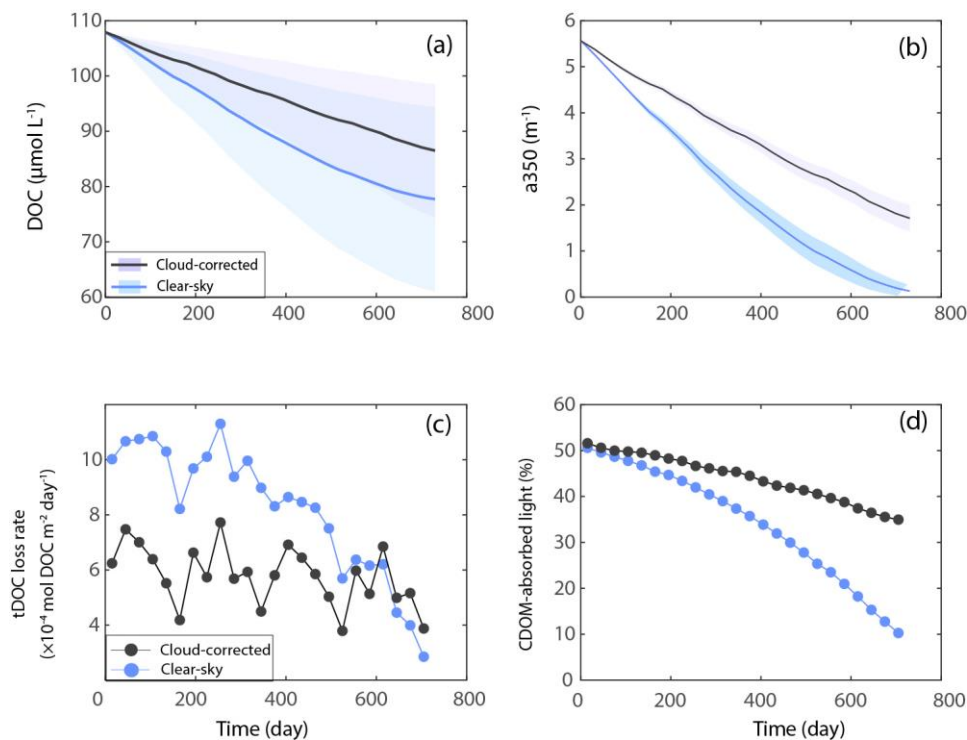
516 **3.4 Photodegradation in the southern Malacca Strait**

517 In the cloud-corrected simulation for the southern Malacca Strait, our model predicted that
518 photoremineralization over 2 years reduced the initial tDOC by $20 \pm 11\%$ from $108 \mu\text{mol L}^{-1}$
519 to $86 \pm 12 \mu\text{mol L}^{-1}$, while the initial CDOM a_{350} was reduced by $69 \pm 5\%$ from 5.6 m^{-1} to 1.7
520 $\pm 0.3 \text{ m}^{-1}$ (Fig. 5a–b, Table 2). Under clear-sky conditions, $28 \pm 16\%$ of tDOC was
521 photo-remineralized and $98 \pm 4\%$ of CDOM was photobleached, with a decrease in tDOC
522 concentration from initially $108 \mu\text{mol L}^{-1}$ to $78 \pm 17 \mu\text{mol L}^{-1}$ and a decrease in a_{350} from 5.6
523 m^{-1} to $0.13 \pm 0.2 \text{ m}^{-1}$ (Fig. 5a–b). Our clear-sky simulation represents a maximum possible
524 extent of tDOC photodegradation.

525

526 The areal rate of tDOC photo-remineralization (pr_{DOC}) showed seasonal variation according
527 to the seasonality in solar irradiance (Fig. 5c, Fig. S3c). Our results show that 51% of solar
528 irradiance (integrated over 300–700 nm) was absorbed by CDOM on Day 1, but this
529 percentage dropped to 34% (cloud-corrected conditions) and 8% (clear-sky conditions) by the
530 end of the 2-year simulation period (Fig. 5d).

531



533

534 Figure 5. Simulated photodegradation for the southern Malacca Strait. (a) Changes in DOC

535 concentration and (b) CDOM absorption (a_{350}) due to solar radiation under cloud-corrected

536 and clear-sky conditions over our 2-year simulation. The shading represents the model

537 uncertainty as estimated by Monte Carlo simulation. (c) Temporal changes in the

538 photo-remineralization rate. (d) Decrease in the percentage of irradiance (integrated over

539 300–700 nm) absorbed by CDOM over time due to CDOM photobleaching.

540

541 Using the results of Year 1 under the cloud-corrected conditions, we calculated the monthly

542 depth-normalized photochemical decay constant, ϕ , which was 0.0002–0.0003 day⁻¹. The543 maximum photochemical decay constant, or the decay constant at the water surface, ϕ^{ref} ,544 was 0.008–0.017 day⁻¹ with a mean of 0.012 day⁻¹ for the southern Malacca Strait. This value

545 could be used to parameterize the UniDOM framework when modeling tDOC turnover for

546 this region.

547

548 To provide a comparison, we also ran a simulation in which we used the broadband AQY
549 instead of the spectrally resolved AQY. The simulation with broadband AQY predicted
550 almost twice as much photodegradation as the simulation with spectrally resolved AQY, with
551 photochemical tDOC loss of 42% (cloud-corrected) and 58% (clear-sky) over two years
552 (Table S5), but we consider this to be an overestimate (see Section 4.2).

553

554 **3.5 The Talang Region**

555 We modeled tDOC photodegradation for four 3-month periods (i.e., February to April, May
556 to July, August to October, and November to January) for the Talang Region, which are the
557 periods showing greatest seasonal differences in solar irradiance (Fig. 6, Table 2). Our model
558 predicted that after 3 months under cloud-corrected conditions, DOC concentration decreased
559 from initially 181 $\mu\text{mol L}^{-1}$ to 173–176 $\mu\text{mol L}^{-1}$, or by 3–4%; the CDOM a_{350} decreased
560 from 10.3 m^{-1} to between 8.7–9.3 m^{-1} , or by 10–15%. Photobleaching of CDOM exhibited
561 pronounced seasonal variation: the early Southwest Monsoon (May to July, when solar
562 irradiance is highest) showed the greatest removal of CDOM (15% loss) while the Northeast
563 Monsoon (November to January) showed the smallest removal (10% loss). Under clear-sky
564 conditions, DOC concentration decreased from initially 181 $\mu\text{mol L}^{-1}$ to 167 $\mu\text{mol L}^{-1}$, or by
565 8%, and the a_{350} of CDOM decreased from 10.3 m^{-1} to 7.3–7.5 m^{-1} , or by 28%, after 3 months.
566 The uncertainty in the final DOC concentration and a_{350} as estimated from our Monte Carlo

567 approach was $\pm 2\text{--}4 \mu\text{mol L}^{-1}$ and $\pm 0.1 \text{ m}^{-1}$, respectively.

568

569 The areal rate of DOC photo-remineralization was $3\text{--}7.6 \times 10^{-4} \text{ mol m}^{-2} \text{ day}^{-1}$ under
570 cloud-corrected conditions and $10\text{--}12 \times 10^{-4} \text{ mol m}^{-2} \text{ day}^{-1}$ under clear-sky conditions
571 (Fig. 6i–l).. Seasonal variation in photoremineralization rate was greater in the
572 cloud-corrected simulation, and the rate was lowest during the NE Monsoon and highest
573 during the early SW Monsoon. The depth-normalized photochemical decay constant, \emptyset , was
574 $0.0003\text{--}0.0005 \text{ day}^{-1}$, which returned a photochemical decay constant at the water surface,
575 \emptyset^{ref} , of $0.007\text{--}0.018 \text{ day}^{-1}$ with a mean of 0.013 day^{-1} .

576

577

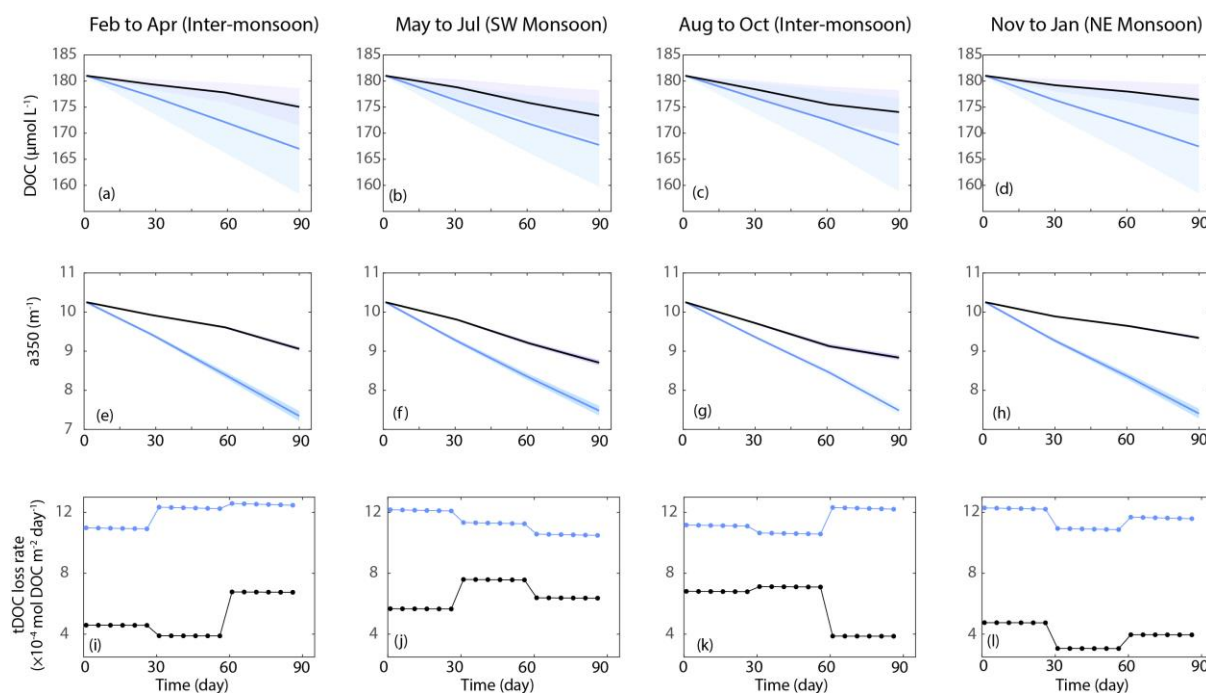
578

579

580

581

582



583

584 Figure 6. Simulated photodegradation for the Talang Region. (a)–(d) Changes in DOC
 585 concentrations and (e)–(h) Changes in the CDOM absorption (a_{350}) under cloud-corrected
 586 and clear-sky conditions for three months in different periods of the year. The grey shading
 587 represents the uncertainties as estimated from the Monte Carlo simulation. (i)–(l) Seasonal
 588 variation in the modeled *in-situ* photo-rem mineralization rates.

589

590 Table 2. Summary of simulated photodegradation under the cloud-corrected conditions. For
 591 the Talang Region, the range in results obtained for the four different time periods is given.

		Initial	Final	%loss
Southern	DOC ($\mu\text{mol L}^{-1}$)	108	86 ± 10	$20 \pm 9\%$
Malacca Strait (730 days)	CDOM a_{350} (m^{-1})	5.6	1.7 ± 0.2	$69 \pm 4\%$

Talang Region	DOC ($\mu\text{mol L}^{-1}$)	181	173–176	3–4%
(90 days)	CDOM a_{350} (m^{-1})	10.3	8.7–9.3	10–15%

592

593

594 4 Discussion

595 4.1 Photodegradability of Southeast Asian peat-tDOC

596 Our experimental results indicate that a high proportion of tDOC from Southeast Asian
597 peatlands is photo-labile, consistent with previous work on tDOC from the
598 peatland-influenced Congo River (Spencer et al., 2009; Stubbins et al., 2010). The shelf water
599 tDOC collected from the Singapore Strait contained a smaller photo-labile fraction (<8% loss
600 OF tDOC), which was expected because the more photo-labile fractions of tDOC had most
601 likely already been remineralized before reaching the Singapore Strait (Zhou et al., 2021).

602

603 We use the photo-remineralization efficiency $\phi_{DOC}(330nm)$ to compare our data to
604 previous literature. Our AQY for Southeast Asian peatland tDOC is comparable to that in
605 large rivers and estuaries globally, but much lower compared to boreal inland waters and
606 oceanic DOC (Table 3). Our AQY is similar to that of Congo River tDOC, which is also
607 partly derived from peatlands (Aarnos et al., 2018), suggesting that tropical peatland tDOC,
608 despite its high photo-lability due to the high aromatic content, is probably not amongst the
609 most efficient organic carbon pools worldwide in the photo-production of CO_2 .

610

611 Table 3. Comparison of apparent quantum yield at 330 nm irradiance for tDOC
 612 photo-remineralization from this study to values in previous literature.

Study site(s)	$\phi_{DOC}(330nm)$ $\mu\text{mol C mol photons}^{-1}$	Reference
Maludam River	440 (Exp 1, Maludam River)	This study
(Peatland-derived DOC)	129 (Exp 2, diluted Maludam river water)	
	156 (Exp 4, Maludam River)	
Singapore Strait (Southwest Monsoon during seasonal tDOC input)	203	This study
World's major rivers	172–335	Aarnos et al. (2018)
Congo River	286	Aarnos et al. (2018)
(Peatland-derived tDOC)		
Tropical and temperate lakes	250–750	Koehler et al. (2016)
Delaware Estuary	249	White et al. (2010)
Inshore waters	514	Powers & Miller (2015)
Boreal Lakes	300–2000	Koehler et al. (2014, 2016)
Humic Lake	708	Vähätalo et al. (2000)
Coastal Waters	989	Johannessen & Miller (2001)
Open Ocean	2900	Johannessen & Miller (2001)

613

614

615 **4.2 Limitations of the AQY determination**

616 Our approach for calculating spectrally resolved AQY from our experiments has limitations,
617 but as we show below, these limitations do not affect our modeling results and conclusion.

618 The limitations are: 1) the method assumes that AQY decreases exponentially with increasing
619 wavelength, and 2) the optimized AQY spectrum does not have a unique solution but varies
620 depending on the starting values chosen for the optimization.

621

622 The assumption that AQY spectra have an exponential shape has been validated by
623 measurements of AQY for pure organic molecules at multiple discrete wavelengths (Gao &
624 Zepp, 1998; C. A. Moore et al., 1993; Moran & Zepp, 1997) and is thus reasonable to be
625 extended to the natural organic matter pool (Aarnos et al., 2012; Koehler et al., 2016;
626 Vähätalo et al., 2000). Experiments using wavelength cut-off filters or monochromatic light
627 sources also confirm that AQYs for natural DOC show exponential spectra (Ward et al.,
628 2021).

629

630 To address the impact of the optimization parameters, we ran a sensitivity analysis in which
631 we changed the starting value of coefficient c in the AQY calculation from 1.0 (Aarnos et al.,
632 2012, 2018) to first 0.01 and then to 100, and then repeated our model simulation with each
633 of the two resulting AQY spectra. We found that changing the starting values for the

634 coefficients over this range of 4 orders of magnitude did indeed change the shape of the AQY
635 spectra (Fig. S5), but this only changed our final estimate of how much tDOC is
636 photo-remineralized by < 6% (Table S6). While this rather limited sensitivity of our model
637 result to the shape of the AQY spectrum may seem surprising, it is a consequence of the fact
638 that we are simulating photodegradation in a well-mixed water column that is optically thick,
639 i.e. the incoming solar radiation is nearly all absorbed within the water layer we are
640 simulating. Therefore, with a steeper AQY spectrum our model predicts more DOC loss close
641 to the surface where there is more UV light but less DOC loss deeper down; while with a
642 flatter AQY spectrum, there is less DOC loss at shallow depths but in turn more DOC loss in
643 deeper waters caused by visible wavelengths. It should be noted that if photodegradation is
644 being modeled for a water layer that is optically thinner (e.g. for a surface mixed layer that is
645 shallower than the euphotic zone depth) the uncertainty in AQY spectral shape associated
646 with this optimization calculation could be much more significant.

647

648 Despite these limitations, it is important to use a spectral AQY rather than applying a
649 broadband AQY when simulating photodegradation in an optically thick water layer because
650 the irradiance spectrum shifts strongly to longer wavelengths (with lower AQY) within just
651 1–2 m below the surface in these optically complex waters (Martin et al., 2021). However,
652 the broadband AQY in our experiments was necessarily determined by exposing optically
653 thin tDOC solutions to full-spectrum irradiance. This broadband AQY is only appropriate for
654 calculating photodegradation in a water layer that is similarly optically thin as in the

655 experimental conditions, such that the depth-integrated spectrum of photons absorbed by
656 CDOM has a similar shape between the model and the experiments – but if it is applied in
657 deeper waters where the irradiance spectrum (and the depth-integrated spectrum of photons
658 absorbed by CDOM) is shifted to longer wavelengths, it overestimates the photodegradation.
659 This is illustrated by the fact that when we used the broadband AQY from our experiments to
660 run our model, it predicted around twice as much tDOC loss compared to the simulation with
661 spectrally resolved AQY (see Table S5 and Section 3.3). This clearly represents an
662 overestimate of the tDOC photo-remineralization, because the depth-integrated spectrum of
663 photons absorbed by CDOM for our modeled water column is shifted considerably towards
664 blue and green wavelengths (that have lower AQY than UV light) relative to that in our
665 experiments that are used to calculate the AQY (Fig. S6).

666

667 Finally, our AQY spectra were derived from a limited number of samples. Although the
668 Maludam River and Singapore Strait samples are likely fairly well representative of the
669 peatland tDOC in Southeast Asia (Section 2.1.1), and our uncertainty analysis shows that the
670 variation between these AQY spectra does not result in substantial model uncertainties
671 (Sections 3.4 and 3.5), more AQY determinations should be made for this region.

672

673 **4.3 Contribution of photodegradation to total tDOC remineralization**

674 Previous work showed that at least 60–70% of tDOC exported from Sumatran peatlands is
675 remineralized in the coastal waters of the Sunda Shelf Sea (Wit et al., 2018; Zhou et al.,

2021). Given also that the direct microbial remineralization appears to be slow and therefore a minor sink for tDOC over the residence time of tDOC on the shelf, we previously hypothesized that photodegradation accounts for a significant part of this remineralization (Nichols & Martin 2021; Zhou et al. 2021). However, our cloud-corrected model simulation shows that solar radiation can only directly remineralize $20 \pm 11\%$ of the initial tDOC input during the 2-year residence time on the shelf. This would account for 31% of the total tDOC remineralization estimated by Zhou et al. (2021). While direct photo-remineralization thus appears to make an important contribution, it is clearly not the only important process. We therefore infer that photochemically enhanced microbial remineralization (Cory et al., 2007; Cory & Kling, 2018; Judd et al., 2007; Moran & Zepp, 1997) might be important in Southeast Asia. Such interactive remineralization was estimated to account for 32% of the total tDOC remineralization on the Louisiana Shelf (Fichot & Benner, 2014). Our photodegradation experiments suggested a preferential removal of tDOC compounds with high apparent molecular weight upon solar radiation, which would be consistent with increased bio-lability of the partially photodegraded tDOC (Miller & Moran, 1997; Moran et al., 2000; Moran & Zepp, 1997). However, photodegradation can also compete with biodegradation for the same tDOC fractions (Ward et al., 2017). Further research is therefore required to quantify the contribution of photo-enhanced bio-remineralization to the tDOC processing.

694

In the Talang Region, solar irradiation can only directly remineralize 3–4% of the initial tDOC input over 3 months (given the more open coastline in this region, tDOC will most

697 likely be removed by mixing and advection over time scales longer than 3 months). This low
698 photodegradation rate from our modeling is consistent with the conservative mixing behavior
699 and the limited degradation of tDOC across peatland-draining estuaries in Southeast Asia
700 reported previously (Alkhatib et al., 2007; Baum et al., 2007; Martin et al., 2018). However,
701 solar radiation removes 7–12% of the riverine CDOM in this region over three months.
702 Photobleaching can therefore remove a significant portion of CDOM over seasonal time
703 scales, as hypothesized by Kaushal et al. (2021). The seasonal variation in the extent of
704 photobleaching observed from our modeling (i.e., greater loss of CDOM during Southwest
705 Monsoon than Northeast Monsoon) is driven by the seasonal changes in irradiance in this
706 region, chiefly due to the seasonality of cloud cover (Fig. S3d), and might contribute to the
707 large seasonal decrease in CDOM after the NE Monsoon inferred from coral skeleton
708 luminescence (Kaushal et al., 2021).

709

710 Our modeling results also indicate that photodegradation might play a larger role in tDOC
711 processing in the Sunda Shelf Sea compared to regions at higher latitudes. On the Louisiana
712 Shelf, direct photo-remineralization appears to remove only 4% of the riverine tDOC input
713 within the surface mixed layer, accounting for only 8% of the total tDOC remineralization
714 (Fichot & Benner, 2014). On a global scale, Aarnos et al. (2018) estimated that if all riverine
715 CDOM is photobleached, 18% of the riverine tDOC flux is photo-remineralized in the ocean.
716 That estimate is close to our results that 20% of the Sumatran peatland tDOC is
717 photo-remineralized on the shelf, showing the quantitatively important role of

718 photo-remineralization in the tropical shelf sea in Southeast Asia. The greater relative
719 contribution from photo-remineralization here is likely due to the relatively long water
720 residence time in the shelf sea (2 years) (Mayer et al., 2015), the higher solar irradiance in the
721 tropics (Apell & McNeill, 2019) and the low bio-lability of the tDOC (Nichols & Martin,
722 2021).

723

724 **4.4 Decay constants for simplified photodegradation modeling**

725 Our spectrally resolved optical modeling can potentially inform the parameterization of
726 simplified model representations of terrestrial carbon cycling such as UniDOM (Anderson et
727 al., 2019), which was proposed as a modeling framework that is sufficiently simplified to be
728 included in large-scale Earth System Models. Specifically, we can use our results to estimate
729 the decay rate constants ϕ and ϕ^{ref} that are key input variables in UniDOM, so that tDOC
730 photo-remineralization can be modelled realistically in Southeast Asia. The ϕ^{ref} derived
731 from our modeling results ($0.008 - 0.017 \text{ day}^{-1}$) is much smaller than the default global value
732 used in UniDOM (0.13 day^{-1}), which was based on the observed decay rate in laboratory
733 photodegradation experiments. UniDOM applies a large age-dependent term to rapidly
734 decrease the very high initial maximum decay rate over time based on global observations of
735 the decreasing DOC turnover rate with the increasing DOC age (Catalán et al., 2016; Evans
736 et al., 2017) and to yield an overall realistic extent of photo-remineralization. In contrast, our
737 photodegradation experiments did not show a systematic decrease in the photochemical
738 efficiency (i.e., AQY) of tDOC over time (Table S4). This suggests that a large age-dependent

739 correction might not be the most appropriate way to parameterize photochemical tDOC,
740 provided that realistic *in-situ* values of ϕ^{ref} can be estimated.

741

742 Our data also show that high photo-lability as measured in experimental incubations does not
743 necessarily lead to a high *in-situ* photodegradation rate because the latter is also dependent on
744 the *in-situ* light dose, the depth-integrated total amount of tDOC and CDOM, and other
745 inherent optical properties (IOPs) in the water. For example, our Exp 1 showed that a 22-day
746 simulated solar radiation can cause a loss of 74% of the initial tDOC. However, the *in-situ*
747 solar irradiance ($35 \text{ mol photons m}^{-2} \text{ day}^{-1}$, integrated over 300–700nm) is only one-fifth of
748 the irradiance in the solar simulator ($181 \text{ mol photons m}^{-2} \text{ day}^{-1}$), while the tDOC amount to
749 be remineralized in the entire water column of the shelf sea (2.12 mol m^{-2}) is 35 times of that
750 in each cuvette used in the photodegradation experiments (0.06 mol m^{-2}). The extent of tDOC
751 photo-remineralization on the shelf is also constrained by its residence time. Regarding the
752 IOPs in the water, the particulate absorption and backscattering are lower than the CDOM
753 absorption for both modeled regions, partly because of the low chlorophyll-*a* concentrations
754 in the study region (Martin et al., 2018, 2022). The light attenuation coefficient, K_d , is
755 therefore dominated by CDOM absorption (Martin et al., 2021), especially at ultraviolet
756 wavelengths. Given the multiple controlling factors of *in-situ* photodegradation rates, we
757 recommend performing spectrally resolved optical modeling to obtain more accurate
758 estimates of the photochemical decay rate constant that can then be used by simplified
759 models across much larger scales.

760

761

762 **5 Conclusions**

763 Although the tDOC from Southeast Asian peatlands contains a large photolabile fraction, the
764 apparent quantum yields for tDOC remineralization are fairly low, which is consistent with
765 apparent quantum yields for tDOC reported from major rivers globally. Based on model
766 simulations, we found that (1) natural solar radiation can directly remineralize $20 \pm 11\%$ of
767 the tDOC flux from Sumatran peatlands in the shelf sea, but this process alone is insufficient
768 to account for the high reported extent of tDOC remineralization in this region; (2) seasonal
769 variation in photobleaching of terrestrial CDOM probably contributes to the strong
770 seasonality of coral core luminescence records in the Talang Region of northwestern Borneo
771 (Kaushal et al., 2021); (3) our modeled rates of tDOC photo-remineralization are equivalent
772 to using a photochemical decay constant, ϕ^{ref} , of $0.008 - 0.017 \text{ day}^{-1}$ in the UniDOM model,
773 but an age-dependent correction factor is not necessary. Our study demonstrates that
774 photochemical processing of peatland tDOC is important in Southeast Asia but falls far short
775 of explaining the extent of tDOC remineralization observed in the Sunda Shelf Sea. We
776 hypothesize that interactions between photochemical and microbial remineralization are
777 likely significant in this region and need to be quantified in future research.

778

779 **Acknowledgements**

780 We are grateful to the many students and research staff, especially from Nanyang

781 Technological University, Swinburne University of Science and Technology, and Universiti
782 Malaysia Sarawak, who helped with field and laboratory work. Permission for this research
783 was given by the National Parks Board, Singapore (permit NP/RP17-044-3), and by the
784 Sarawak Forestry Department and Sarawak Biodiversity Centre (permits
785 NPW.907.4.4(Jld.14)-161, WL83/2017, and SBC-RA-0097-MM). Patrick Martin
786 acknowledges funding by the Singapore Ministry of Education under the Academic Research
787 Fund Tier 2 programme (grant MOE-MOET2EP10121-0007) and by the National Research
788 Foundation Singapore, Prime Minister's Office, as part of the Marine Science Research and
789 Development Programme (grant MSRDP-P32). Moritz Müller was funded by MOHE FRGS
790 15 (grant FRGS/1/2015/WAB08/SWIN/02/1) and by the Newton-Ungku Omar Fund (grant
791 GL/F07/NUOF/01/2017). Nagur Cherukuru was funded by CSIRO Oceans and Atmosphere
792 and by the Regional Collaborations Programme (Australian Academy of Sciences).

793

794 **Open Research**

795 Raw experimental data and source codes for data processing and modeling are available
796 through the NTU data repository (<https://doi.org/10.21979/N9/XQSOEN>).

797

798 **Author Contributions**

799 Conceptualization: Y.Z., P.M.;

800 Methodology: Y.Z., P.M.;

801 Software: Y.Z.;

802 Formal analysis: Y.Z.;

803 Resources: P.M., M.M., N.C.;

804 Data curation: Y.Z., M.M., N.C., P.M.;

805 Investigation: Y.Z.;

806 Writing – original draft preparation: Y.Z.;

807 Writing – review and editing: Y.Z., M.M., N.C., P.M.;

808 Supervision: P.M.;

809 Project administration: P.M.;

810 Funding acquisition: P.M., M.M., N.C.

811

812

813 **References**

- 814 Aarnos, H., Ylöstalo, P., & Vähätalo, A. V. (2012). Seasonal phototransformation of dissolved
815 organic matter to ammonium, dissolved inorganic carbon, and labile substrates
816 supporting bacterial biomass across the Baltic Sea. *Journal of Geophysical Research:*
817 *Biogeosciences*, *117*(1), 1–14. <https://doi.org/10.1029/2010JG001633>
- 818 Aarnos, H., Gélinas, Y., Kasurinen, V., Gu, Y., Puupponen, V. M., & Vähätalo, A. V. (2018).
819 Photochemical Mineralization of Terrigenous DOC to Dissolved Inorganic Carbon in
820 Ocean. *Global Biogeochemical Cycles*, *32*(2), 250–266.
821 <https://doi.org/10.1002/2017GB005698>
- 822 Aksnes, D. L., Dupont, N., Staby, A., Fiksen, Ø., Kaartvedt, S., & Aure, J. (2009). Coastal

823 water darkening and implications for mesopelagic regime shifts in Norwegian fjords.
824 *Marine Ecology Progress Series*, 387(Jerlov 1968), 39–49.
825 <https://doi.org/10.3354/meps08120>

826 Alkhatib, M., Jennerjahn, T. C., & Samiaji, J. (2007). Biogeochemistry of the Dumai River
827 estuary, Sumatra, Indonesia, a tropical black-water river. *Limnology and Oceanography*,
828 52(6), 2410–2417. <https://doi.org/10.4319/lo.2007.52.6.2410>

829 Allesson, L., Koehler, B., Thrane, J. E., Andersen, T., & Hessen, D. O. (2021). The role of
830 photomineralization for CO₂ emissions in boreal lakes along a gradient of dissolved
831 organic matter. *Limnology and Oceanography*, 66(1), 158–170.
832 <https://doi.org/10.1002/lno.11594>

833 Anderson, T. R., Rowe, E. C., Polimene, L., Tipping, E., Evans, C. D., Barry, C. D. G., et al.
834 (2019). Unified concepts for understanding and modelling turnover of dissolved organic
835 matter from freshwaters to the ocean: the UniDOM model. *Biogeochemistry*, 146(2),
836 105–123. <https://doi.org/10.1007/s10533-019-00621-1>

837 Apell, J. N., & McNeill, K. (2019). Updated and validated solar irradiance reference spectra
838 for estimating environmental photodegradation rates. *Environmental Science: Processes
839 and Impacts*, 21(3), 427–437. <https://doi.org/10.1039/c8em00478a>

840 Baum, A., Rixen, T., & Samiaji, J. (2007). Relevance of peat draining rivers in central
841 Sumatra for the riverine input of dissolved organic carbon into the ocean. *Estuarine,
842 Coastal and Shelf Science*, 73(3–4), 563–570. <https://doi.org/10.1016/j.ecss.2007.02.012>

843 Beleites, C., & Sergio, V. (2012). hyperSpec: a package to handle hyperspectral data sets in R.

844 *Journal of Statistical Software.*

845 Cai, W.-J. (2011). Estuarine and Coastal Ocean Carbon Paradox: CO₂ Sinks or Sites of
846 Terrestrial Carbon Incineration? *Annual Review of Marine Science*, 3(1), 123–145.
847 <https://doi.org/10.1146/annurev-marine-120709-142723>

848 Catalán, N., Marcé, R., Kothawala, D. N., & Tranvik, L. J. (2016). Organic carbon
849 decomposition rates controlled by water retention time across inland waters. *Nature*
850 *Geoscience*, 9(7), 501–504. <https://doi.org/10.1038/ngeo2720>

851 Chen, H., Abdulla, H. A. N., Sanders, R. L., Myneni, S. C. B., Mopper, K., & Hatcher, P. G.
852 (2014). Production of Black Carbon-like and Aliphatic Molecules from Terrestrial
853 Dissolved Organic Matter in the Presence of Sunlight and Iron. *Environmental Science*
854 *and Technology Letters*, 1(10), 399–404. <https://doi.org/10.1021/ez5002598>

855 Cherukuru, N., Martin, P., Sanwlani, N., Mujahid, A., & Müller, M. (2021). A semi-analytical
856 optical remote sensing model to estimate suspended sediment and dissolved organic
857 carbon in tropical coastal waters influenced by peatland-draining river discharges off
858 sarawak, borneo. *Remote Sensing*, 13(1), 1–31. <https://doi.org/10.3390/rs13010099>

859 Ciais, P., Sabine, C., & Bala, G. (2013). Chapter 6: Carbon and other biogeochemical cycles.
860 *Climate Change 2013: The Physical Science Basis.*

861 Cory, R. M., & Kling, G. W. (2018). Interactions between sunlight and microorganisms
862 influence dissolved organic matter degradation along the aquatic continuum. *Limnology*
863 *and Oceanography Letters*, 3(3), 102–116. <https://doi.org/10.1002/lol2.10060>

864 Cory, R. M., McKnight, D. M., Chin, Y. P., Miller, P., & Jaros, C. L. (2007). Chemical

865 characteristics of fulvic acids from Arctic surface waters: Microbial contributions and
866 photochemical transformations. *Journal of Geophysical Research: Biogeosciences*,
867 *112*(4), 1–14. <https://doi.org/10.1029/2006JG000343>

868 Dittmar, T., Whitehead, K., Minor, E. C., & Koch, B. P. (2007). Tracing terrigenous dissolved
869 organic matter and its photochemical decay in the ocean by using liquid
870 chromatography/mass spectrometry. *Marine Chemistry*, *107*(3), 378–387.
871 <https://doi.org/10.1016/j.marchem.2007.04.006>

872 Evans, C. D., Futter, M. N., Moldan, F., Valinia, S., Frogbrook, Z., & Kothawala, D. N.
873 (2017). Variability in organic carbon reactivity across lake residence time and trophic
874 gradients. *Nature Geoscience*, *10*(11), 832–835. <https://doi.org/10.1038/NGEO3051>

875 Fichot, C. G., & Benner, R. (2014). The fate of terrigenous dissolved organic carbon in a
876 river-influenced ocean margin. *Global Biogeochemical Cycles*, *28*(3), 300–318.
877 <https://doi.org/10.1002/2013GB004670>

878 Fichot, C. G., & Miller, W. L. (2010). An approach to quantify depth-resolved marine
879 photochemical fluxes using remote sensing: Application to carbon monoxide (CO)
880 photoproduction. *Remote Sensing of Environment*, *114*(7), 1363–1377.
881 <https://doi.org/10.1016/j.rse.2010.01.019>

882 Gao, H., & Zepp, R. G. (1998). Factors influencing photoreactions of dissolved organic
883 matter in a coastal river of the southeastern United States. *Environmental Science and*
884 *Technology*, *32*(19), 2940–2946. <https://doi.org/10.1021/es9803660>

885 GEBCO Compilation Group. (2020). GEBCO 2020 Grid.

886 <https://doi.org/10.5285/a29c5465-b138-234d-e053-6c86abc040b9>

887 Giesen, W., Wijedasa, L. S., & Page, S. E. (2018). Unique Southeast Asian peat swamp forest
888 habitats have relatively few distinctive plant species. *Mires and Peat*, 22, 1–13.
889 <https://doi.org/10.19189/MaP.2017.OMB.287>

890 Gu, Y., Lensu, A., Perämäki, S., Ojala, A., & Vähätalo, A. V. (2017). Iron and pH Regulating
891 the Photochemical Mineralization of Dissolved Organic Carbon. *ACS Omega*, 2(5),
892 1905–1914. <https://doi.org/10.1021/acsomega.7b00453>

893 Helms, J. R., Stubbins, A., Ritchie, J. D., Minor, E. C., Kieber, D. J., & Mopper, K. (2008).
894 Absorption spectral slopes and slope ratios as indicators of molecular weight, source,
895 and photobleaching of chromophoric dissolved organic matter. *Limnology and*
896 *Oceanography*, 53(3), 955–969. <https://doi.org/10.4319/lo.2008.53.3.0955>

897 Helms, J. R., Stubbins, A., Perdue, E. M., Green, N. W., Chen, H., & Mopper, K. (2013).
898 Photochemical bleaching of oceanic dissolved organic matter and its effect on
899 absorption spectral slope and fluorescence. *Marine Chemistry*, 155, 81–91.
900 <https://doi.org/10.1016/j.marchem.2013.05.015>

901 Helms, J. R., Mao, J., Schmidt-Rohr, K., Abdulla, H., & Mopper, K. (2013). Photochemical
902 flocculation of terrestrial dissolved organic matter and iron. *Geochimica et*
903 *Cosmochimica Acta*, 121, 398–413. <https://doi.org/10.1016/j.gca.2013.07.025>

904 Jankowski, J. J., Kieber, D. J., & Mopper, K. (1999a). Nitrate and nitrite ultraviolet
905 actinometers. *Photochemistry and Photobiology*, 70(3), 319–328.
906 <https://doi.org/10.1111/j.1751-1097.1999.tb08143.x>

907 Jankowski, J. J., Kieber, D. J., & Mopper, K. (1999b). Nitrate and Nitrite Ultraviolet
908 Actinometers. *Photochemistry and Photobiology*, 70(3), 319–328.
909 <https://doi.org/10.1111/j.1751-1097.1999.tb08143.x>

910 Johannessen, S. C., & Miller, W. L. (2001). Quantum yield for the photochemical production
911 of dissolved inorganic carbon in seawater. *Marine Chemistry*, 76(4), 271–283.
912 [https://doi.org/10.1016/S0304-4203\(01\)00067-6](https://doi.org/10.1016/S0304-4203(01)00067-6)

913 Judd, K. E., Crump, B. C., & Kling, G. W. (2007). Bacterial responses in activity and
914 community composition to photo-oxidation of dissolved organic matter from soil and
915 surface waters. *Aquatic Sciences*, 69(1), 96–107.
916 <https://doi.org/10.1007/s00027-006-0908-4>

917 Kaiser, K., Benner, R., & Amon, R. M. W. (2017). The fate of terrigenous dissolved organic
918 carbon on the Eurasian shelves and export to the North Atlantic. *Journal of Geophysical*
919 *Research: Oceans*, 122(1), 4–22. <https://doi.org/10.1002/2016JC012380>

920 Kaushal, N., Sanwlani, N., Tanzil, J. T. I., Cherukuru, N., Sahar, S., Müller, M., et al. (2021).
921 Coral Skeletal Luminescence Records Changes in Terrestrial Chromophoric Dissolved
922 Organic Matter in Tropical Coastal Waters. *Geophysical Research Letters*, 48(8), 1–12.
923 <https://doi.org/10.1029/2020GL092130>

924 Kitidis, V., Shutler, J. D., Ashton, I., Warren, M., Brown, I., Findlay, H., et al. (2019). Winter
925 weather controls net influx of atmospheric CO₂ on the north-west European shelf.
926 *Scientific Reports*, 9(1), 1–11. <https://doi.org/10.1038/s41598-019-56363-5>

927 Koehler, B., Landelius, T., Weyhenmeyer, G. A., Machida, N., & Tranvik, L. J. (2014).

928 Sunlight-induced carbon dioxide emissions from inland waters. *Global Biogeochemical*
929 *Cycles*, 28(7), 696–711. <https://doi.org/10.1002/2014GB004850>

930 Koehler, B., Broman, E., & Tranvik, L. J. (2016). Apparent quantum yield of photochemical
931 dissolved organic carbon mineralization in lakes. *Limnology and Oceanography*, 61(6),
932 2207–2221. <https://doi.org/10.1002/lno.10366>

933 Koehler, B., Powers, L. C., Cory, R. M., Einarsdóttir, K., Gu, Y., Tranvik, L. J., et al. (2022).
934 Inter-laboratory differences in the apparent quantum yield for the photochemical
935 production of dissolved inorganic carbon in inland waters and implications for
936 photochemical rate modeling. *Limnology and Oceanography: Methods*, 320–337.
937 <https://doi.org/10.1002/lom3.10489>

938 Lee, Z. P., Du, K. P., & Arnone, R. (2005). A model for the diffuse attenuation coefficient of
939 downwelling irradiance. *Journal of Geophysical Research C: Oceans*, 110(2), 1–10.
940 <https://doi.org/10.1029/2004JC002275>

941 Martin, P., Cherukuru, N., Tan, A. S. Y., Sanwlan, N., Mujahid, A., & Müller, M. (2018).
942 Distribution and cycling of terrigenous dissolved organic carbon in peatland-draining
943 rivers and coastal waters of Sarawak, Borneo. *Biogeosciences*, 15(22), 6847–6865.
944 <https://doi.org/10.5194/bg-15-6847-2018>

945 Martin, P., Sanwlan, N., Lee, T., Wong, J., Chang, K., Wong, E., & Liew, S. (2021).
946 Dissolved organic matter from tropical peatlands reduces shelf sea light availability in
947 the Singapore Strait, Southeast Asia. *Marine Ecology Progress Series*.
948 <https://doi.org/10.3354/meps13776>

949 Martin, P., Moynihan, M. A., Chen, S., Woo, O. Y., Zhou, Y., Nichols, R. S., et al. (2022).
950 Monsoon-driven biogeochemical dynamics in an equatorial shelf sea: Time-series
951 observations in the Singapore Strait. *Estuarine, Coastal and Shelf Science*, 270(April),
952 107855. <https://doi.org/10.1016/j.ecss.2022.107855>

953 Massicotte, P., Asmala, E., Stedmon, C., & Markager, S. (2017). Global distribution of
954 dissolved organic matter along the aquatic continuum: Across rivers, lakes and oceans.
955 *Science of The Total Environment*, 609, 180–191.
956 <https://doi.org/10.1016/j.scitotenv.2017.07.076>

957 Mathis, M., Logemann, K., Maerz, J., Lacroix, F., Hagemann, S., Chegini, F., et al. (2022).
958 Seamless Integration of the Coastal Ocean in Global Marine Carbon Cycle Modeling.
959 *Journal of Advances in Modeling Earth Systems*, 14(8), 1–44.
960 <https://doi.org/10.1029/2021MS002789>

961 Mayer, B., Stacke, T., Stottmeister, I., & Pohlmann, T. (2015). Sunda Shelf Seas: flushing
962 rates and residence times. *Ocean Science Discussions*, 12(3), 863–895.
963 <https://doi.org/10.5194/osd-12-863-2015>

964 Mayer, B., Rixen, T., & Pohlmann, T. (2018). The spatial and temporal variability of air-sea
965 CO₂ fluxes and the effect of net coral reef calcification in the Indonesian Seas: A
966 numerical sensitivity study. *Frontiers in Marine Science*, 5(APR), 1–19.
967 <https://doi.org/10.3389/fmars.2018.00116>

968 Miller, W. L., & Moran, M. A. (1997). Interaction of photochemical and microbial processes
969 in the degradation of refractory dissolved organic matter from a coastal marine

970 environment. *Limnology and Oceanography*, 42(6), 1317–1324.
971 <https://doi.org/10.4319/lo.1997.42.6.1317>

972 Moore, C. A., Farmer, C. T., & Zika, R. G. (1993). Influence of the Orinoco River on
973 hydrogen peroxide distribution and production in the eastern Caribbean. *Journal of*
974 *Geophysical Research: Oceans*, 98(C2), 2289–2298. <https://doi.org/10.1029/92JC02767>

975 Moore, S., Gauci, V., Evans, C. D., & Page, S. E. (2011). Fluvial organic carbon losses from a
976 Bornean blackwater river. *Biogeosciences*, 8(4), 901–909.
977 <https://doi.org/10.5194/bg-8-901-2011>

978 Mopper, K., Zhou, X., Kieber, R. J., Kieber, D. J., Sikorski, R. J., & Jones, R. D. (1991).
979 Photochemical degradation of dissolved organic carbon and its impact on the oceanic
980 carbon cycle. *Nature*, 353(6339), 60–62. <https://doi.org/10.1038/353060a0>

981 Moran, M. A., & Zepp, R. G. (1997). Role of photoreactions in the formation of biologically
982 labile compounds from dissolved organic matter. *Limnology and Oceanography*, 42(6),
983 1307–1316. <https://doi.org/10.4319/lo.1997.42.6.1307>

984 Moran, M. A., Sheldon, W. M., & Zepp, R. G. (2000). Carbon loss and optical property
985 changes during long-term photochemical and biological degradation of estuarine
986 dissolved organic matter. *Limnology and Oceanography*, 45(6), 1254–1264.
987 <https://doi.org/10.4319/lo.2000.45.6.1254>

988 Müller, D., Warneke, T., Rixen, T., Müller, M., Jamahari, S., Denis, N., et al. (2015). Lateral
989 carbon fluxes and CO₂ outgassing from a tropical peat-draining river. *Biogeosciences*,
990 12(20), 5967–5979. <https://doi.org/10.5194/bg-12-5967-2015>

- 991 Nichols, R. S., & Martin, P. (2021). Low biodegradability of dissolved organic matter from
992 Southeast Asian peat-draining rivers. *Journal of Geophysical Research: Biogeosciences*.
993 <https://doi.org/10.1029/2020JG006182>
- 994 Painter, S. C., Lapworth, D. J., Woodward, E. M. S., Kroeger, S., Evans, C. D., Mayor, D. J.,
995 & Sanders, R. J. (2018). Terrestrial dissolved organic matter distribution in the North
996 Sea. *Science of the Total Environment*, 630, 630–647.
997 <https://doi.org/10.1016/j.scitotenv.2018.02.237>
- 998 Powers, L. C., & Miller, W. L. (2015). Photochemical production of CO and CO₂ in the
999 Northern Gulf of Mexico: Estimates and challenges for quantifying the impact of
1000 photochemistry on carbon cycles. *Marine Chemistry*, 171, 21–35.
1001 <https://doi.org/10.1016/j.marchem.2015.02.004>
- 1002 Powers, L. C., Brandes, J. A., Miller, W. L., & Stubbins, A. (2017). Using liquid
1003 chromatography-isotope ratio mass spectrometry to measure the $\delta^{13}\text{C}$ of dissolved
1004 inorganic carbon photochemically produced from dissolved organic carbon. *Limnology
1005 and Oceanography: Methods*, 15(1), 103–115. <https://doi.org/10.1002/lom3.10146>
- 1006 Rixen, T., Wit, F., Hutahaean, A. A., Schlüter, A., Baum, A., Klemme, A., et al. (2022). 4 -
1007 Carbon cycle in tropical peatlands and coastal seas. In T. C. Jennerjahn, T. Rixen, H. E.
1008 Irianto, & J. Samiaji (Eds.), *Science for the Protection of Indonesian Coastal
1009 Ecosystems (SPICE)* (pp. 83–142). Elsevier.
1010 <https://doi.org/https://doi.org/10.1016/B978-0-12-815050-4.00011-0>
- 1011 Semiletov, I., Pipko, I., Gustafsson, Ö., Anderson, L. G., Sergienko, V., Pugach, S., et al.

1012 (2016). Acidification of East Siberian Arctic Shelf waters through addition of freshwater
1013 and terrestrial carbon. *Nature Geoscience*, 9(5), 361–365.
1014 <https://doi.org/10.1038/NEGO2695>

1015 Spencer, R. G. M., Stubbins, A., Hernes, P. J., Baker, A., Mopper, K., Aufdenkampe, A. K., et
1016 al. (2009). Photochemical degradation of dissolved organic matter and dissolved lignin
1017 phenols from the Congo River. *Journal of Geophysical Research*, 114(G03010).
1018 <https://doi.org/10.1029/2009JG000968>

1019 Stubbins, A., Spencer, R. G. M., Chen, H., Hatcher, P. G., Mopper, K., Hernes, P. J., et al.
1020 (2010). Illuminated darkness: Molecular signatures of Congo River dissolved organic
1021 matter and its photochemical alteration as revealed by ultrahigh precision mass
1022 spectrometry. *Limnology and Oceanography*, 55(4), 1467–1477.
1023 <https://doi.org/10.4319/lo.2010.55.4.1467>

1024 Stubbins, A., Mann, P. J., Powers, L., Bittar, T. B., Dittmar, T., McIntyre, C. P., et al. (2017).
1025 Low photolability of yedoma permafrost dissolved organic carbon. *Journal of*
1026 *Geophysical Research: Biogeosciences*, 122(1), 200–211.
1027 <https://doi.org/10.1002/2016JG003688>

1028 Susanto, D., Wei, Z., Adi, R., Zhang, Q., Fang, G., Fan, B., et al. (2016). Oceanography
1029 Surrounding Krakatau Volcano in the Sunda Strait, Indonesia. *Oceanography*, 29(2), 0–
1030 29. <https://doi.org/10.5670/oceanog.2016.31>

1031 Tzortziou, M., Osburn, C. L., & Neale, P. J. (2007). Photobleaching of dissolved organic
1032 material from a tidal marsh-estuarine system of the Chesapeake Bay. *Photochemistry*

- 1033 *and Photobiology*, 83(4), 782–792. <https://doi.org/10.1111/j.1751-1097.2007.00142.x>
- 1034 Urtizberea, A., Dupont, N., Rosland, R., & Aksnes, D. L. (2013). Sensitivity of euphotic zone
1035 properties to CDOM variations in marine ecosystem models. *Ecological Modelling*, 256,
1036 16–22. <https://doi.org/10.1016/j.ecolmodel.2013.02.010>
- 1037 Vähätalo, A. V., Salkinoja-Salonen, M., Taalas, P., & Salonen, K. (2000). Spectrum of the
1038 quantum yield for photochemical mineralization of dissolved organic carbon in a humic
1039 lake. *Limnology and Oceanography*, 45(3), 664–676.
1040 <https://doi.org/10.4319/lo.2000.45.3.0664>
- 1041 Vähätalo, A. V., Salonen, K., Münster, U., Järvinen, M., & Wetzel, R. G. (2003).
1042 Photochemical transformation of allochthonous organic matter provides bioavailable
1043 nutrients in a humic lake. *Archiv Fur Hydrobiologie*, 156(3), 287–314.
1044 <https://doi.org/10.1127/0003-9136/2003/0156-0287>
- 1045 Ward, C. P., Nalven, S. G., Crump, B. C., Kling, G. W., & Cory, R. M. (2017). Photochemical
1046 alteration of organic carbon draining permafrost soils shifts microbial metabolic
1047 pathways and stimulates respiration. *Nature Communications*, 8(1), 1–7.
1048 <https://doi.org/10.1038/s41467-017-00759-2>
- 1049 Ward, C. P., Bowen, J. C., Freeman, D. H., & Sharpless, C. M. (2021). Rapid and
1050 reproducible characterization of the wavelength dependence of aquatic photochemical
1051 reactions using light-emitting diodes. *Environmental Science and Technology Letters*,
1052 8(5), 437–442. <https://doi.org/10.1021/acs.estlett.1c00172>
- 1053 Weishaar, J. L., Aiken, G. R., Bergamaschi, B. A., Fram, M. S., Fujii, R., & Mopper, K.

1054 (2003). Evaluation of Specific Ultraviolet Absorbance as an Indicator of the Chemical
1055 Composition and Reactivity of Dissolved Organic Carbon. *Environmental Science &*
1056 *Technology*, 37(20), 4702–4708. <https://doi.org/10.1021/es030360x>

1057 White, E. M., Kieber, D. J., Sherrard, J., Miller, W. L., & Mopper, K. (2010). Carbon dioxide
1058 and carbon monoxide photoproduction quantum yields in the Delaware Estuary. *Marine*
1059 *Chemistry*, 118(1–2), 11–21. <https://doi.org/10.1016/j.marchem.2009.10.001>

1060 Wit, F., Rixen, T., Baum, A., Pranowo, W. S., & Hutahaean, A. A. (2018). The Invisible
1061 Carbon Footprint as a hidden impact of peatland degradation inducing marine carbonate
1062 dissolution in Sumatra, Indonesia. *Scientific Reports*, 8(1), 17403.
1063 <https://doi.org/10.1038/s41598-018-35769-7>

1064 Zepp, R. G. (2007). Solar UVR and aquatic Carbon, nitrogen, sulfur and metals cycles. In E.
1065 W. Helbling & H. Zagarese (Eds.) (pp. 137–184). Cambridge: Royal Society of
1066 Chemistry. <https://doi.org/10.1039/9781847552266-00137>

1067 Zhou, Y., Martin, P., & Müller, M. (2019). Composition and cycling of dissolved organic
1068 matter from tropical peatlands of coastal Sarawak, Borneo, revealed by fluorescence
1069 spectroscopy and parallel factor analysis. *Biogeosciences*, 16(13), 2733–2749.
1070 <https://doi.org/10.5194/bg-16-2733-2019>

1071 Zhou, Y., Evans, C. D., Chen, Y., Chang, K. Y. W., & Martin, P. (2021). Extensive
1072 Remineralization of Peatland-Derived Dissolved Organic Carbon and Ocean
1073 Acidification in the Sunda Shelf Sea, Southeast Asia. *Journal of Geophysical Research:*
1074 *Oceans*, 126(6), 1–23. <https://doi.org/10.1029/2021JC017292>

1075 Zika, R. G. (1981). Chapter 10 Marine Organic Photochemistry. In *Elsevier Oceanography*

1076 *Series* (Vol. 31, pp. 299–325). [https://doi.org/10.1016/S0422-9894\(08\)70332-5](https://doi.org/10.1016/S0422-9894(08)70332-5)

1077

1078

1079

1080

1081

1082

1083

1084

1085

1086

1087

1088

1089

Supporting Information

1090 Photodegradation of dissolved organic carbon derived from tropical peatlands in

1091 the Sunda Shelf Sea, Southeast Asia

1092

1093 Yongli Zhou^{1,*},[†], Moritz Müller², Nagur Cherukuru³, Patrick Martin^{1,*}

1094

1095 ¹Asian School of the Environment, Nanyang Technological University, 639798 Singapore

1096 ²Faculty of Engineering, Computing and Science, Swinburne University of Science and

1097 Technology, 93350 Kuching, Sarawak, Malaysia

1098 ³CSIRO Oceans and Atmosphere Flagship, Canberra ACT 2601, Australia

1099 [†]Current address: Ecosystem Center, Marine Biological Laboratory, Woods Hole, 02543,

1100 United States

1101

1102 **A1 Apparent quantum yield (AQY) calculations**

1103 **A1.1 Broadband AQY**

1104 The broadband apparent quantum yield ($\phi_{broadband}$) (unit: mol C (mol photons)⁻¹) for tDOC

1105 photo-remineralization was calculated for Exp 1–4 based on the DOC loss and the amount of

1106 photons absorbed following Fichot & Benner (2014) with the wavelength range modified:

$$1107 \quad \phi_{broadband} = \frac{DOC_{initial} - DOC_{final}}{\int_{t_0}^{t_{final}} \int_{290nm}^{700nm} \Xi((\lambda, t)) d\lambda dt} \quad (S1)$$

1108 where DOC is the amount of DOC (mol) in the sample; $\Xi(\lambda, t)$ is the downwelling

1109 irradiance absorbed by CDOM in the quartz cell (mol photons nm⁻¹ s⁻¹); λ denotes

1110 wavelength (nm); t denotes time (s). $\Xi(\lambda, t)$ was calculated following Fichot & Benner
1111 (2014):

$$1112 \quad \Xi(\lambda, t) = E_d(\lambda) T S (1 - e^{-K_{d,cell}(\lambda, t) PL}) \frac{a_g(\lambda, t)}{K_{d,cell}(\lambda, t)} \quad (S2)$$

1113 where $E_d(\lambda)$ is the downwelling irradiance spectrum of the xenon lamp just above the
1114 quartz cell (mol photons $\text{nm}^{-1} \text{s}^{-1} \text{m}^{-2}$, kept constant during the experiments); T (unitless) is
1115 the transmittance of the quartz window (0.95); S is the surface area (m^2) of the cuvette; and
1116 PL is the thickness (m) of the sample solution in the quartz cell. $K_{d,cell}(\lambda, t)$ is the diffuse
1117 attenuation coefficient of downwelling irradiance (m^{-1}) in the sample solution, which is the
1118 sum of the absorption of CDOM ($a_{CDOM}(\lambda, t)$) (m^{-1}), the absorption of water ($a_w(\lambda)$) (m^{-1})
1119 and the backscattering of water ($bb_w(\lambda)$) (m^{-1}) following Fichot and Benner (2014):

$$1120 \quad K_{d,cell}(\lambda, t) \cong a_{CDOM}(\lambda, t) + a_w(\lambda) + bb_w(\lambda) \quad (S3).$$

1121 Because the samples were filtered, we did not include particulate absorption and
1122 backscattering here in the calculations. Note that the absorption of CDOM ($a_{CDOM}(\lambda, t)$)
1123 decreases over time due to photobleaching. It was measured at regular intervals during each
1124 experiment, and the mean absorption of every two consecutive time points was used to
1125 calculate the absorbed photons $\Xi(\lambda, t)$ for the corresponding time interval. $E_d(\lambda)$ was
1126 measured from 177 nm to 872 nm at 1 nm resolution with an Ocean Insights FLAME
1127 radiometer, and the spectrum between 290 nm and 318 nm was derived by linear
1128 interpolation assuming zero irradiance at ≤ 290 nm.

1129

1130

1131 **A1.2 Spectrally resolved AQY**

1132 The spectrally resolved AQY for tDOC photo-remineralization ($\phi_{DOC}(\lambda)$) was calculated for
1133 each experiment as in Aarnos et al. (2018). The $\phi_{DOC}(\lambda)$ was assumed to decrease
1134 exponentially with increasing wavelength (Gao & Zepp, 1998):

1135
$$\phi_{DOC}(\lambda) = c e^{-d\lambda} \quad (S4)$$

1136 where c (mol C (mol photons)⁻¹ nm⁻¹) and d (nm⁻¹) are positive constants. The amount of the
1137 photo-remineralized DOC can be related to the AQY spectrum $\phi_{DOC}(\lambda)$ and the absorbed
1138 irradiance $\Xi((\lambda, t)$:

1139
$$DOC_{initial} - DOC_{final} = \int_{t_{initial}}^{t_{final}} \int_{290nm}^{700nm} \phi_{DOC}(\lambda) \Xi((\lambda, t) d\lambda dt \quad (S5).$$

1140 Therefore, c and d in Eq. 4 were iterated until the right side of Eq. S5 was as close as possible
1141 to the measured DOC loss, i.e., the left side of Eq. 5 using the *fminsearch* function of
1142 MATLAB. Because the optimized values of c and d are dependent on the starting values
1143 provided for iteration, a Monte Carlo approach was used to perturb the starting values and
1144 generate multiple combinations of c and d (Gu et al., 2017). The combination that provided
1145 the best fit between the modeled DOC loss and the measured DOC loss was selected (see
1146 Supporting Information in Aarnos et al., (2018)).

1147

1148 The concept of AQY was extended to the dose-dependent decrease in CDOM absorption. We
1149 refer to this as $\phi_{CDOM}(\lambda)$, which is the spectrally resolved AQY for the decrease in the
1150 volume-integrated CDOM absorption coefficient, with units of L m⁻¹ (mol photons)⁻¹ nm⁻¹.
1151 For example, the decrease in the volume-integrated Napierian absorption coefficient at 350

1152 nm (a_{350}) can be related to its spectrally resolved AQY $\phi_{a_{350}}(\lambda)$ and the absorbed irradiance
1153 $\Xi(\lambda, t)$ as:

$$1154 \quad (a_{350,initial} - a_{350,final} V) = \int_{t_{initial}}^{t_{final}} \int_{290nm}^{700nm} \phi_{a_{350}}(\lambda) \Xi(\lambda, t) d\lambda dt \quad (S6)$$

1155 where V is the volume (in L) of the sample solution. To obtain the volume-integrated CDOM
1156 absorption, the measured absorption coefficient is multiplied by the volume of the water
1157 sample, yielding $L m^{-1}$. We assumed that, like $\phi_{DOC}(\lambda)$, the $\phi_a(\lambda)$ decreases exponentially
1158 with increasing wavelength. For a_{350} , we have:

$$1159 \quad \phi_{a_{350}}(\lambda) = c' e^{-d'\lambda} \quad (S7)$$

1160 where c' ($L m^{-1} nm^{-1}$) and d' (nm^{-1}) are positive constants, which were iterated until the
1161 right side of Eq. S6 was as close as possible to the left side of Eq. S6 using the *fminsearch*
1162 function of MATLAB. This calculation was repeated across the CDOM absorption spectrum
1163 at 1-nm resolution from 250–700 nm, which returned 451 respective AQY spectra, i.e., AQY
1164 spectrum for a_{250} , AQY spectrum for a_{251} , AQY spectrum for a_{252} , ..., AQY spectrum for a_{691} ,
1165 AQY spectrum for a_{700} . Concatenating all these 1-dimensional AQY spectra returned the
1166 2-dimensional AQY spectrum shown in Figure 4b.

1167

1168

1169

1170 **A2 Photodegradation model**

1171 **A2.1 Model calculations**

1172 The DOC concentration at time T was calculated from its value at time $T-I$ and the amount of

1173 DOC consumed during the period between $T-1$ and T as:

$$1174 \quad DOC_T = DOC_{T-1} - \frac{\int_{T-1}^T pr_{DOC}(t) dt}{V} S \quad (S8)$$

1175 where $pr_{DOC}(t)$ is the areal rate of photo-remineralization of tDOC ($\text{mol C m}^{-2} \text{s}^{-1}$), S is the
1176 surface area of the water column under consideration (i.e., 1 m^2) and V is the volume of the
1177 water column (m^3), which was calculated from the water depth (Section 2.5.3) and surface
1178 area (1 m^2 here). The $pr_{DOC}(t)$ was calculated from the AQY spectrum ($\phi_{DOC}(\lambda)$) and the
1179 number of photons absorbed by CDOM ($\Xi(\lambda, t)$) in the water column:

$$1180 \quad pr_{DOC}(t) = \int_{300nm}^{700nm} \phi_{DOC}(\lambda) \Xi(\lambda, t) d\lambda \quad (S9).$$

1181 The irradiance absorbed by CDOM, $\Xi(\lambda, t)$, was calculated as:

$$1182 \quad \Xi(\lambda, t) = E_{o,0^-}(\lambda, t) (1 - e^{-K_o(\lambda, t) D}) f_{CDOM}(\lambda, t) \quad (S10)$$

1183 where $E_{o,0^-}(\lambda, t)$ is the total (i.e. upwelling + downwelling) scalar irradiance just below the
1184 water surface, $K_o(\lambda, t)$ is the diffuse attenuation coefficient of scalar irradiance, D is the
1185 water depth and $f_{CDOM}(\lambda, t)$ is the wavelength- and time-specific fraction of irradiance that
1186 is absorbed by CDOM. The right side of Eq. 10, except the term $f_{CDOM}(\lambda, t)$, calculates the
1187 total absorbed irradiance in the water column. We neglected the irradiance below 300 nm
1188 because the particulate absorption spectra, which were used for the calculation of K_o (see
1189 below), were not available below 300 nm. To assess the error caused by neglecting the
1190 irradiance below 300 nm, we used the simulated solar irradiance spectrum from 300–700 nm,
1191 and the AQY spectra for DOC photo-remineralization and CDOM photobleaching to
1192 back-calculate the DOC loss for our photodegradation Exp 1. The results only differed by 1.6%
1193 from the measured DOC loss, which shows that neglecting the irradiance below 300 nm only

1194 introduces a minimal error.

1195

1196 Because the upwelling irradiance is generally very small in waters that are optically deep,
1197 $E_{o,0^-}(\lambda, t)$ was approximated as the downwelling scalar irradiance, $E_{od,0^-}(\lambda, t)$, which was
1198 derived from the total (i.e. diffuse + direct) downwelling irradiance just above the water
1199 surface, $E_{d,0^+}(\lambda, t)$ (see Section 2.5.3), following (Fichot & Miller, 2010). $K_o(\lambda, t)$ was
1200 approximated using the diffuse attenuation coefficient of downwelling irradiance, $K_d(\lambda, t)$
1201 (Fichot & Miller, 2010). Therefore, Eq. 10 can be rewritten as Eq. 11 and was used in our
1202 model:

$$1203 \quad \Xi(\lambda, t) = E_{od,0^-}(\lambda, t) (1 - e^{-K_d(\lambda, t) D}) f_{CDOM}(\lambda, t) \quad (S11).$$

1204

1205 Light attenuation $K_d(\lambda, t)$ was calculated following Lee et al. (2005):

$$1206 \quad K_d(\lambda, t) = (1 + 0.005 \theta(t)) a_{tot}(\lambda, t) + 1.48 (1 - 0.52 e^{-10.8 a_{tot}(\lambda, t)}) b_{b_{tot}}(\lambda) \quad (S12)$$

1207 where $\theta(t)$ is the solar zenith angle above the water surface (degrees), $a_{tot}(\lambda, t)$ is the
1208 total absorption coefficient and $b_{b_{tot}}(\lambda)$ is the total backscattering coefficient in the shelf
1209 waters:

$$1210 \quad a_{tot}(\lambda, t) = a_{CDOM}(\lambda, t) + a_p(\lambda) + a_w(\lambda) \quad (S13)$$

$$1211 \quad b_{b_{tot}}(\lambda) = b_{b_p}(\lambda) + b_{b_w}(\lambda) \quad (S14)$$

1212 where the subscripts $CDOM$, p , w denote CDOM, particulates, and water, respectively.

1213 Particulate absorption and backscattering spectra were taken from in-situ measurements in
1214 our two model regions and were assumed to be constant over time.

1215

1216 The fraction of irradiance absorbed by CDOM, $f_{CDOM}(\lambda, t)$, was calculated as:

1217
$$f_{CDOM}(\lambda, t) = \frac{(1+0.005 \theta(t)) a_{CDOM}(\lambda, t)}{K_d(\lambda, t)} \quad (S15)$$

1218 where the numerator is the diffuse attenuation coefficient of downwelling irradiance that is
1219 only caused by CDOM absorption, while the denominator is the actual K_d calculated from
1220 CDOM, particles, and water.

1221

1222 In Eq. S15, the CDOM spectrum at time point T , $a_{CDOM}(\lambda, T)$, can be calculated from the
1223 CDOM spectrum at time point $T-1$ and the amount of CDOM that was photobleached
1224 between $T-1$ and T . For example, for a_{350} :

1225
$$a_{350, T} = a_{350, T-1} - \frac{\int_{T-1}^T pr_{a_{350}}(t) dt}{V} S \quad (S16)$$

1226 where $pr_{a_{350}}(t)$ is the areal rate of decrease in the volume-integrated a_{350} , S is the surface
1227 area of the water column (i.e., 1 m²) and V is the volume of the water column. The $pr_{a_{350}}(t)$
1228 was calculated as:

1229
$$pr_{a_{350}}(t) = \int_{300nm}^{700nm} \phi_{a_{350}}(\lambda) \Xi(\lambda, t) d\lambda \quad (S17)$$

1230 where $\phi_{a_{350}}(\lambda)$ is the spectrally resolved AQY for the decrease in the volume-integrated
1231 a_{350} of CDOM (Eq. S7); $\Xi(\lambda, t)$ is the number of photons absorbed by CDOM (Eq. S11).

1232 Because $pr_{a_{350}}(t)$ needs to be calculated from $a_{350}(t)$, Eq. S16 cannot be solved. Thus, in
1233 practice, the $\int_{T-1}^T pr_{a_{350}}(t) dt$ in Eq. S16 was approximated as $pr_{a_{350, T-1}} \Delta T$. Our results
1234 show that the daily change in CDOM absorption coefficient is small enough to allow this
1235 approximation. This calculation was applied across the CDOM spectrum at 1nm resolution

1236 from 250–700 nm to obtain $a_{CDOM}(\lambda, t)$.

1237

1238

1239

1240 **A2.2 Model input data**

1241 **A2.2.1 Solar irradiance**

1242 The downwelling irradiance spectrum above the water surface, $E_{d,0^+}(\lambda, t)$, and the solar
1243 zenith angle, $\theta(t)$, for each time point were obtained from the Tropospheric Ultraviolet and
1244 Visible (TUV) Radiation Model (US National Center for Atmospheric Research,
1245 [https://www2.acom.ucar.edu/modeling/tropospheric-ultraviolet-and-visible-tuv-radiation-mo](https://www2.acom.ucar.edu/modeling/tropospheric-ultraviolet-and-visible-tuv-radiation-model)
1246 [del](https://www2.acom.ucar.edu/modeling/tropospheric-ultraviolet-and-visible-tuv-radiation-model)). Data were obtained on an hourly basis for the 15th day of each month of 2019 for two
1247 locations: 0.5°N 104.5°E, representative of the southern Malacca Strait, and 1.9°N 109.7°E,
1248 representative of the Talang Region. For both locations, $E_{d,0^+}(\lambda, t)$ under clear-sky and
1249 cloud-corrected conditions was obtained. The overhead ozone column, the optical depth of
1250 clouds, and the optical depth of aerosols as input parameters for the TUV model were
1251 obtained from NASA Earth Observations (<https://neo.sci.gsfc.nasa.gov/>).

1252

1253 **A2.2.2 Particulate absorption and backscattering**

1254 For the southern Malacca Strait, particulate absorption and backscattering coefficients were
1255 obtained from bi-monthly measurements in the Singapore Strait between December 2018 to
1256 December 2020 (Martin et al., 2021). For the Talang Region, particulate absorption and

1257 backscattering coefficients were measured in September 2017 at multiple stations between
1258 the estuary of the Samunsam River and the Talang Islands (Cherukuru et al., 2021). For both
1259 regions, the particulate absorption coefficients were measured on samples filtered onto glass
1260 fiber filters using an integrating sphere accessory on a spectrophotometer, while particulate
1261 backscattering coefficients were measured at 9 wavelengths using a Wetlabs BB9 lowered to
1262 1m depth below water surface. Detailed methods can be found in Martin et al. (2021) and
1263 Cherukuru et al. (2021).

1264

1265 We fit a power-law function to each sample particulate backscattering spectrum ($R^2 = 0.05$ –
1266 0.78 for the Southern Malacca Strait, samples with $R^2 < 0.34$ were neglected; $R^2 = 0.68$ – 0.80
1267 for Talang Region) to obtain spectra from 300–700 nm at 1-nm resolution. We calculated the
1268 mean and standard deviation of the particulate absorption and backscattering spectra as the
1269 model input parameters (i.e., $a_p(\lambda)$ and $b_{b_p}(\lambda)$).

1270

1271 **A2.2.3 Starting values of DOC concentration and CDOM absorption**

1272 The initial DOC concentration for the southern Malacca Strait was calculated by assuming
1273 conservative mixing between peatland-draining rivers on Sumatra and seawater to a salinity
1274 of 29, which is approximately the lowest salinity in the Singapore Strait during the periods
1275 with strong terrestrial input (Zhou et al., 2021):

$$1276 \quad \text{DOC}(t_0) = \text{DOC}_{\text{Sumatra}} \times f_{\text{river}} \quad (\text{S18})$$

1277 where $\text{DOC}_{\text{Sumatra}}$ is the discharge-weighted average of riverine endmember DOC

1278 concentration of the major rivers on Sumatra ($890 \mu\text{mol L}^{-1}$) (Wit et al., 2018), and f_{river} is
1279 the fraction of freshwater in the modeling regions. Note that a marine DOC component was
1280 not included in Eq. 18 because we only model the photodegradation of terrigenous DOC here.
1281 In addition, marine CDOM was found in very low concentration in these oligotrophic waters
1282 (Martin et al., 2021), so neglecting the marine CDOM does not affect our estimates of light
1283 absorption by CDOM.

1284

1285 The f_{river} was calculated from salinity:

$$1286 \quad f_{river} = \left(1 - \frac{sal_{mod}}{sal_{marine}}\right) \quad (\text{S19})$$

1287 where sal_{mod} is the salinity in the modeling region (i.e., 29) and sal_{marine} is the marine
1288 endmember salinity for the water from the open South China Sea, which is taken as 33
1289 following Zhou et al. (2021). These calculations returned an initial DOC concentration of 108
1290 $\mu\text{mol L}^{-1}$ for the modeling for the Southern Malacca Strait.

1291

1292 CDOM spectral data from Sumatran rivers are not available. The DOC-specific absorbance at
1293 254 nm (SUVA_{254}) of the Maludam River ($5\text{--}6 \text{ L mg}^{-1} \text{ m}^{-1}$) is comparable to that of other
1294 peatland-draining rivers in northwestern Borneo (Martin et al., 2018), and we take the
1295 CDOM-to-DOC ratio of the Maludam River as representative of peatland-draining rivers in
1296 Southeast Asia. Therefore, we calculated the initial CDOM spectrum for the Southern
1297 Malacca Strait based on the DOC-specific CDOM absorption spectrum of the Maludam River
1298 and our riverine end-member DOC concentration for Sumatra ($890 \mu\text{mol L}^{-1}$):

1299
$$a_{CDOM, initial}(\lambda) = \frac{a_{CDOM, Maludam}(\lambda)}{DOC_{Maludam}} \times DOC_{Sumatra} \times f_{river} \quad (S20)$$

1300 where $a_{CDOM, Maludam}(\lambda)$ and $DOC_{Maludam}$ is the CDOM spectrum and DOC
 1301 concentration, respectively, of the Maludam River water sample (collected in December
 1302 2017). The starting CDOM absorption spectrum in Day 1 for modeling is shown in Fig. S3e.

1303

1304 For the Talang Region, the starting DOC concentration and the CDOM absorption spectrum
 1305 in Day 1 were calculated by assuming conservative mixing between the Samunsam River
 1306 water and seawater to salinity of 29 using Eqns. S18–S20. Riverine endmember DOC
 1307 concentration and CDOM absorption in the Samunsam River were measured in March and
 1308 September 2017 (Martin et al., 2018). Calculations using the annual mean riverine DOC
 1309 concentration of $1493 \mu\text{mol L}^{-1}$ returned an initial DOC concentration of $181 \mu\text{mol L}^{-1}$ and an
 1310 initial CDOM absorption spectrum (Fig. S3f) for modeling for the Talang Region.

1311

1312 A2.3 Photochemical decay constant of UniDOM

1313 First, we calculated the depth-normalized photochemical decay constant, \emptyset , based on the
 1314 monthly loss of DOC of year 1 from our modeling results under the cloud-corrected
 1315 conditions:

1316
$$\emptyset = \frac{\ln(DOC_{t1}) - \ln(DOC_{t2})}{\Delta t} \quad (S21)$$

1317 where DOC_{t1} and DOC_{t2} is the DOC concentration in the first and the last day of the
 1318 month, respectively. We then converted the \emptyset to \emptyset^{ref} based on equations in Anderson et al.
 1319 (2019):

1320
$$\phi^{ref} = \frac{\phi \times D}{\frac{1}{k_{UV}} - \frac{e^{-k_{UV} D}}{k_{UV}}} \quad (S22)$$

1321 where D is the water depth and k_{UV} is the extinction coefficient, which was approximated
1322 using the water UV attenuation, k_{UVW} , (0.12 m⁻¹) and CDOM decadic absorption coefficient
1323 at 350nm, k_{350} :

1324
$$k_{UV} = k_{UVW} + k_{350} \quad (S23).$$

1325 This returned ϕ^{ref} for each month and we report the mean value to account for the seasonal
1326 variation in solar irradiance. A decline in the decay constant with age proposed by Anderson
1327 et al. (2019) was not considered in our calculation because we did not observe a decrease in
1328 the apparent quantum yield over the course of our photodegradation experiments (Table S4).

1329

1330

1331 **References in Supporting information**

1332 Aarnos, H., Ylöstalo, P., & Vähätalo, A. V. (2012). Seasonal phototransformation of dissolved
1333 organic matter to ammonium, dissolved inorganic carbon, and labile substrates
1334 supporting bacterial biomass across the Baltic Sea. *Journal of Geophysical Research:*
1335 *Biogeosciences*, 117(1), 1–14. <https://doi.org/10.1029/2010JG001633>

1336 Aarnos, H., Gélinas, Y., Kasurinen, V., Gu, Y., Puupponen, V. M., & Vähätalo, A. V. (2018).
1337 Photochemical Mineralization of Terrigenous DOC to Dissolved Inorganic Carbon in
1338 Ocean. *Global Biogeochemical Cycles*, 32(2), 250–266.
1339 <https://doi.org/10.1002/2017GB005698>

1340 Aksnes, D. L., Dupont, N., Staby, A., Fiksen, Ø., Kaartvedt, S., & Aure, J. (2009). Coastal

1341 water darkening and implications for mesopelagic regime shifts in Norwegian fjords.
1342 *Marine Ecology Progress Series*, 387(Jerlov 1968), 39–49.
1343 <https://doi.org/10.3354/meps08120>

1344 Alkhatib, M., Jennerjahn, T. C., & Samiaji, J. (2007). Biogeochemistry of the Dumai River
1345 estuary, Sumatra, Indonesia, a tropical black-water river. *Limnology and Oceanography*,
1346 52(6), 2410–2417. <https://doi.org/10.4319/lo.2007.52.6.2410>

1347 Alleson, L., Koehler, B., Thrane, J. E., Andersen, T., & Hessen, D. O. (2021). The role of
1348 photomineralization for CO₂ emissions in boreal lakes along a gradient of dissolved
1349 organic matter. *Limnology and Oceanography*, 66(1), 158–170.
1350 <https://doi.org/10.1002/lno.11594>

1351 Anderson, T. R., Rowe, E. C., Polimene, L., Tipping, E., Evans, C. D., Barry, C. D. G., et al.
1352 (2019). Unified concepts for understanding and modelling turnover of dissolved organic
1353 matter from freshwaters to the ocean: the UniDOM model. *Biogeochemistry*, 146(2),
1354 105–123. <https://doi.org/10.1007/s10533-019-00621-1>

1355 Apell, J. N., & McNeill, K. (2019). Updated and validated solar irradiance reference spectra
1356 for estimating environmental photodegradation rates. *Environmental Science: Processes
1357 and Impacts*, 21(3), 427–437. <https://doi.org/10.1039/c8em00478a>

1358 Baum, A., Rixen, T., & Samiaji, J. (2007). Relevance of peat draining rivers in central
1359 Sumatra for the riverine input of dissolved organic carbon into the ocean. *Estuarine,
1360 Coastal and Shelf Science*, 73(3–4), 563–570. <https://doi.org/10.1016/j.ecss.2007.02.012>

1361 Beleites, C., & Sergio, V. (2012). hyperSpec: a package to handle hyperspectral data sets in R.

- 1362 *Journal of Statistical Software.*
- 1363 Cai, W.-J. (2011). Estuarine and Coastal Ocean Carbon Paradox: CO₂ Sinks or Sites of
1364 Terrestrial Carbon Incineration? *Annual Review of Marine Science*, 3(1), 123–145.
1365 <https://doi.org/10.1146/annurev-marine-120709-142723>
- 1366 Catalán, N., Marcé, R., Kothawala, D. N., & Tranvik, L. J. (2016). Organic carbon
1367 decomposition rates controlled by water retention time across inland waters. *Nature*
1368 *Geoscience*, 9(7), 501–504. <https://doi.org/10.1038/ngeo2720>
- 1369 Chen, H., Abdulla, H. A. N., Sanders, R. L., Myneni, S. C. B., Mopper, K., & Hatcher, P. G.
1370 (2014). Production of Black Carbon-like and Aliphatic Molecules from Terrestrial
1371 Dissolved Organic Matter in the Presence of Sunlight and Iron. *Environmental Science*
1372 *and Technology Letters*, 1(10), 399–404. <https://doi.org/10.1021/ez5002598>
- 1373 Cherukuru, N., Martin, P., Sanwlani, N., Mujahid, A., & Müller, M. (2021). A semi-analytical
1374 optical remote sensing model to estimate suspended sediment and dissolved organic
1375 carbon in tropical coastal waters influenced by peatland-draining river discharges off
1376 sarawak, borneo. *Remote Sensing*, 13(1), 1–31. <https://doi.org/10.3390/rs13010099>
- 1377 Ciais, P., Sabine, C., & Bala, G. (2013). Chapter 6: Carbon and other biogeochemical cycles.
1378 *Climate Change 2013: The Physical Science Basis.*
- 1379 Cory, R. M., & Kling, G. W. (2018). Interactions between sunlight and microorganisms
1380 influence dissolved organic matter degradation along the aquatic continuum. *Limnology*
1381 *and Oceanography Letters*, 3(3), 102–116. <https://doi.org/10.1002/lol2.10060>
- 1382 Cory, R. M., McKnight, D. M., Chin, Y. P., Miller, P., & Jaros, C. L. (2007). Chemical

1383 characteristics of fulvic acids from Arctic surface waters: Microbial contributions and
1384 photochemical transformations. *Journal of Geophysical Research: Biogeosciences*,
1385 *112*(4), 1–14. <https://doi.org/10.1029/2006JG000343>

1386 Dittmar, T., Whitehead, K., Minor, E. C., & Koch, B. P. (2007). Tracing terrigenous dissolved
1387 organic matter and its photochemical decay in the ocean by using liquid
1388 chromatography/mass spectrometry. *Marine Chemistry*, *107*(3), 378–387.
1389 <https://doi.org/10.1016/j.marchem.2007.04.006>

1390 Evans, C. D., Futter, M. N., Moldan, F., Valinia, S., Frogbrook, Z., & Kothawala, D. N.
1391 (2017). Variability in organic carbon reactivity across lake residence time and trophic
1392 gradients. *Nature Geoscience*, *10*(11), 832–835. <https://doi.org/10.1038/NGEO3051>

1393 Fichot, C. G., & Benner, R. (2014). The fate of terrigenous dissolved organic carbon in a
1394 river-influenced ocean margin. *Global Biogeochemical Cycles*, *28*(3), 300–318.
1395 <https://doi.org/10.1002/2013GB004670>

1396 Fichot, C. G., & Miller, W. L. (2010). An approach to quantify depth-resolved marine
1397 photochemical fluxes using remote sensing: Application to carbon monoxide (CO)
1398 photoproduction. *Remote Sensing of Environment*, *114*(7), 1363–1377.
1399 <https://doi.org/10.1016/j.rse.2010.01.019>

1400 Gao, H., & Zepp, R. G. (1998). Factors influencing photoreactions of dissolved organic
1401 matter in a coastal river of the southeastern United States. *Environmental Science and*
1402 *Technology*, *32*(19), 2940–2946. <https://doi.org/10.1021/es9803660>

1403 GEBCO Compilation Group. (2020). GEBCO 2020 Grid.

1404 <https://doi.org/10.5285/a29c5465-b138-234d-e053-6c86abc040b9>

1405 Giesen, W., Wijedasa, L. S., & Page, S. E. (2018). Unique Southeast Asian peat swamp forest
1406 habitats have relatively few distinctive plant species. *Mires and Peat*, 22, 1–13.
1407 <https://doi.org/10.19189/MaP.2017.OMB.287>

1408 Gu, Y., Lensu, A., Perämäki, S., Ojala, A., & Vähätalo, A. V. (2017). Iron and pH Regulating
1409 the Photochemical Mineralization of Dissolved Organic Carbon. *ACS Omega*, 2(5),
1410 1905–1914. <https://doi.org/10.1021/acsomega.7b00453>

1411 Helms, J. R., Stubbins, A., Ritchie, J. D., Minor, E. C., Kieber, D. J., & Mopper, K. (2008).
1412 Absorption spectral slopes and slope ratios as indicators of molecular weight, source,
1413 and photobleaching of chromophoric dissolved organic matter. *Limnology and*
1414 *Oceanography*, 53(3), 955–969. <https://doi.org/10.4319/lo.2008.53.3.0955>

1415 Helms, J. R., Stubbins, A., Perdue, E. M., Green, N. W., Chen, H., & Mopper, K. (2013).
1416 Photochemical bleaching of oceanic dissolved organic matter and its effect on
1417 absorption spectral slope and fluorescence. *Marine Chemistry*, 155, 81–91.
1418 <https://doi.org/10.1016/j.marchem.2013.05.015>

1419 Helms, J. R., Mao, J., Schmidt-Rohr, K., Abdulla, H., & Mopper, K. (2013). Photochemical
1420 flocculation of terrestrial dissolved organic matter and iron. *Geochimica et*
1421 *Cosmochimica Acta*, 121, 398–413. <https://doi.org/10.1016/j.gca.2013.07.025>

1422 Jankowski, J. J., Kieber, D. J., & Mopper, K. (1999a). Nitrate and nitrite ultraviolet
1423 actinometers. *Photochemistry and Photobiology*, 70(3), 319–328.
1424 <https://doi.org/10.1111/j.1751-1097.1999.tb08143.x>

- 1425 Jankowski, J. J., Kieber, D. J., & Mopper, K. (1999b). Nitrate and Nitrite Ultraviolet
1426 Actinometers. *Photochemistry and Photobiology*, 70(3), 319–328.
1427 <https://doi.org/10.1111/j.1751-1097.1999.tb08143.x>
- 1428 Johannessen, S. C., & Miller, W. L. (2001). Quantum yield for the photochemical production
1429 of dissolved inorganic carbon in seawater. *Marine Chemistry*, 76(4), 271–283.
1430 [https://doi.org/10.1016/S0304-4203\(01\)00067-6](https://doi.org/10.1016/S0304-4203(01)00067-6)
- 1431 Judd, K. E., Crump, B. C., & Kling, G. W. (2007). Bacterial responses in activity and
1432 community composition to photo-oxidation of dissolved organic matter from soil and
1433 surface waters. *Aquatic Sciences*, 69(1), 96–107.
1434 <https://doi.org/10.1007/s00027-006-0908-4>
- 1435 Kaiser, K., Benner, R., & Amon, R. M. W. (2017). The fate of terrigenous dissolved organic
1436 carbon on the Eurasian shelves and export to the North Atlantic. *Journal of Geophysical*
1437 *Research: Oceans*, 122(1), 4–22. <https://doi.org/10.1002/2016JC012380>
- 1438 Kaushal, N., Sanwlani, N., Tanzil, J. T. I., Cherukuru, N., Sahar, S., Müller, M., et al. (2021).
1439 Coral Skeletal Luminescence Records Changes in Terrestrial Chromophoric Dissolved
1440 Organic Matter in Tropical Coastal Waters. *Geophysical Research Letters*, 48(8), 1–12.
1441 <https://doi.org/10.1029/2020GL092130>
- 1442 Kitidis, V., Shutler, J. D., Ashton, I., Warren, M., Brown, I., Findlay, H., et al. (2019). Winter
1443 weather controls net influx of atmospheric CO₂ on the north-west European shelf.
1444 *Scientific Reports*, 9(1), 1–11. <https://doi.org/10.1038/s41598-019-56363-5>
- 1445 Koehler, B., Landelius, T., Weyhenmeyer, G. A., Machida, N., & Tranvik, L. J. (2014).

1446 Sunlight-induced carbon dioxide emissions from inland waters. *Global Biogeochemical*
1447 *Cycles*, 28(7), 696–711. <https://doi.org/10.1002/2014GB004850>

1448 Koehler, B., Broman, E., & Tranvik, L. J. (2016). Apparent quantum yield of photochemical
1449 dissolved organic carbon mineralization in lakes. *Limnology and Oceanography*, 61(6),
1450 2207–2221. <https://doi.org/10.1002/lno.10366>

1451 Koehler, B., Powers, L. C., Cory, R. M., Einarsdóttir, K., Gu, Y., Tranvik, L. J., et al. (2022).
1452 Inter-laboratory differences in the apparent quantum yield for the photochemical
1453 production of dissolved inorganic carbon in inland waters and implications for
1454 photochemical rate modeling. *Limnology and Oceanography: Methods*, 320–337.
1455 <https://doi.org/10.1002/lom3.10489>

1456 Lee, Z. P., Du, K. P., & Arnone, R. (2005). A model for the diffuse attenuation coefficient of
1457 downwelling irradiance. *Journal of Geophysical Research C: Oceans*, 110(2), 1–10.
1458 <https://doi.org/10.1029/2004JC002275>

1459 Martin, P., Cherukuru, N., Tan, A. S. Y., Sanwlan, N., Mujahid, A., & Müller, M. (2018).
1460 Distribution and cycling of terrigenous dissolved organic carbon in peatland-draining
1461 rivers and coastal waters of Sarawak, Borneo. *Biogeosciences*, 15(22), 6847–6865.
1462 <https://doi.org/10.5194/bg-15-6847-2018>

1463 Martin, P., Sanwlan, N., Lee, T., Wong, J., Chang, K., Wong, E., & Liew, S. (2021).
1464 Dissolved organic matter from tropical peatlands reduces shelf sea light availability in
1465 the Singapore Strait, Southeast Asia. *Marine Ecology Progress Series*.
1466 <https://doi.org/10.3354/meps13776>

1467 Martin, P., Moynihan, M. A., Chen, S., Woo, O. Y., Zhou, Y., Nichols, R. S., et al. (2022).
1468 Monsoon-driven biogeochemical dynamics in an equatorial shelf sea: Time-series
1469 observations in the Singapore Strait. *Estuarine, Coastal and Shelf Science*, 270(April),
1470 107855. <https://doi.org/10.1016/j.ecss.2022.107855>

1471 Massicotte, P., Asmala, E., Stedmon, C., & Markager, S. (2017). Global distribution of
1472 dissolved organic matter along the aquatic continuum: Across rivers, lakes and oceans.
1473 *Science of The Total Environment*, 609, 180–191.
1474 <https://doi.org/10.1016/j.scitotenv.2017.07.076>

1475 Mathis, M., Logemann, K., Maerz, J., Lacroix, F., Hagemann, S., Chegini, F., et al. (2022).
1476 Seamless Integration of the Coastal Ocean in Global Marine Carbon Cycle Modeling.
1477 *Journal of Advances in Modeling Earth Systems*, 14(8), 1–44.
1478 <https://doi.org/10.1029/2021MS002789>

1479 Mayer, B., Stacke, T., Stottmeister, I., & Pohlmann, T. (2015). Sunda Shelf Seas: flushing
1480 rates and residence times. *Ocean Science Discussions*, 12(3), 863–895.
1481 <https://doi.org/10.5194/osd-12-863-2015>

1482 Mayer, B., Rixen, T., & Pohlmann, T. (2018). The spatial and temporal variability of air-sea
1483 CO₂ fluxes and the effect of net coral reef calcification in the Indonesian Seas: A
1484 numerical sensitivity study. *Frontiers in Marine Science*, 5(APR), 1–19.
1485 <https://doi.org/10.3389/fmars.2018.00116>

1486 Miller, W. L., & Moran, M. A. (1997). Interaction of photochemical and microbial processes
1487 in the degradation of refractory dissolved organic matter from a coastal marine

1488 environment. *Limnology and Oceanography*, 42(6), 1317–1324.
1489 <https://doi.org/10.4319/lo.1997.42.6.1317>

1490 Moore, C. A., Farmer, C. T., & Zika, R. G. (1993). Influence of the Orinoco River on
1491 hydrogen peroxide distribution and production in the eastern Caribbean. *Journal of*
1492 *Geophysical Research: Oceans*, 98(C2), 2289–2298. <https://doi.org/10.1029/92JC02767>

1493 Moore, S., Gauci, V., Evans, C. D., & Page, S. E. (2011). Fluvial organic carbon losses from a
1494 Bornean blackwater river. *Biogeosciences*, 8(4), 901–909.
1495 <https://doi.org/10.5194/bg-8-901-2011>

1496 Mopper, K., Zhou, X., Kieber, R. J., Kieber, D. J., Sikorski, R. J., & Jones, R. D. (1991).
1497 Photochemical degradation of dissolved organic carbon and its impact on the oceanic
1498 carbon cycle. *Nature*, 353(6339), 60–62. <https://doi.org/10.1038/353060a0>

1499 Moran, M. A., & Zepp, R. G. (1997). Role of photoreactions in the formation of biologically
1500 labile compounds from dissolved organic matter. *Limnology and Oceanography*, 42(6),
1501 1307–1316. <https://doi.org/10.4319/lo.1997.42.6.1307>

1502 Moran, M. A., Sheldon, W. M., & Zepp, R. G. (2000). Carbon loss and optical property
1503 changes during long-term photochemical and biological degradation of estuarine
1504 dissolved organic matter. *Limnology and Oceanography*, 45(6), 1254–1264.
1505 <https://doi.org/10.4319/lo.2000.45.6.1254>

1506 Müller, D., Warneke, T., Rixen, T., Müller, M., Jamahari, S., Denis, N., et al. (2015). Lateral
1507 carbon fluxes and CO₂ outgassing from a tropical peat-draining river. *Biogeosciences*,
1508 12(20), 5967–5979. <https://doi.org/10.5194/bg-12-5967-2015>

- 1509 Nichols, R. S., & Martin, P. (2021). Low biodegradability of dissolved organic matter from
1510 Southeast Asian peat-draining rivers. *Journal of Geophysical Research: Biogeosciences*.
1511 <https://doi.org/10.1029/2020JG006182>
- 1512 Painter, S. C., Lapworth, D. J., Woodward, E. M. S., Kroeger, S., Evans, C. D., Mayor, D. J.,
1513 & Sanders, R. J. (2018). Terrestrial dissolved organic matter distribution in the North
1514 Sea. *Science of the Total Environment*, 630, 630–647.
1515 <https://doi.org/10.1016/j.scitotenv.2018.02.237>
- 1516 Powers, L. C., & Miller, W. L. (2015). Photochemical production of CO and CO₂ in the
1517 Northern Gulf of Mexico: Estimates and challenges for quantifying the impact of
1518 photochemistry on carbon cycles. *Marine Chemistry*, 171, 21–35.
1519 <https://doi.org/10.1016/j.marchem.2015.02.004>
- 1520 Powers, L. C., Brandes, J. A., Miller, W. L., & Stubbins, A. (2017). Using liquid
1521 chromatography-isotope ratio mass spectrometry to measure the $\delta^{13}\text{C}$ of dissolved
1522 inorganic carbon photochemically produced from dissolved organic carbon. *Limnology
1523 and Oceanography: Methods*, 15(1), 103–115. <https://doi.org/10.1002/lom3.10146>
- 1524 Rixen, T., Wit, F., Hutahaean, A. A., Schlüter, A., Baum, A., Klemme, A., et al. (2022). 4 -
1525 Carbon cycle in tropical peatlands and coastal seas. In T. C. Jennerjahn, T. Rixen, H. E.
1526 Irianto, & J. Samiaji (Eds.), *Science for the Protection of Indonesian Coastal
1527 Ecosystems (SPICE)* (pp. 83–142). Elsevier.
1528 <https://doi.org/https://doi.org/10.1016/B978-0-12-815050-4.00011-0>
- 1529 Semiletov, I., Pipko, I., Gustafsson, Ö., Anderson, L. G., Sergienko, V., Pugach, S., et al.

1530 (2016). Acidification of East Siberian Arctic Shelf waters through addition of freshwater
1531 and terrestrial carbon. *Nature Geoscience*, 9(5), 361–365.
1532 <https://doi.org/10.1038/NEGO2695>

1533 Spencer, R. G. M., Stubbins, A., Hernes, P. J., Baker, A., Mopper, K., Aufdenkampe, A. K., et
1534 al. (2009). Photochemical degradation of dissolved organic matter and dissolved lignin
1535 phenols from the Congo River. *Journal of Geophysical Research*, 114(G03010).
1536 <https://doi.org/10.1029/2009JG000968>

1537 Stubbins, A., Spencer, R. G. M., Chen, H., Hatcher, P. G., Mopper, K., Hernes, P. J., et al.
1538 (2010). Illuminated darkness: Molecular signatures of Congo River dissolved organic
1539 matter and its photochemical alteration as revealed by ultrahigh precision mass
1540 spectrometry. *Limnology and Oceanography*, 55(4), 1467–1477.
1541 <https://doi.org/10.4319/lo.2010.55.4.1467>

1542 Stubbins, A., Mann, P. J., Powers, L., Bittar, T. B., Dittmar, T., McIntyre, C. P., et al. (2017).
1543 Low photolability of yedoma permafrost dissolved organic carbon. *Journal of*
1544 *Geophysical Research: Biogeosciences*, 122(1), 200–211.
1545 <https://doi.org/10.1002/2016JG003688>

1546 Susanto, D., Wei, Z., Adi, R., Zhang, Q., Fang, G., Fan, B., et al. (2016). Oceanography
1547 Surrounding Krakatau Volcano in the Sunda Strait, Indonesia. *Oceanography*, 29(2), 0–
1548 29. <https://doi.org/10.5670/oceanog.2016.31>

1549 Tzortziou, M., Osburn, C. L., & Neale, P. J. (2007). Photobleaching of dissolved organic
1550 material from a tidal marsh-estuarine system of the Chesapeake Bay. *Photochemistry*

- 1551 *and Photobiology*, 83(4), 782–792. <https://doi.org/10.1111/j.1751-1097.2007.00142.x>
- 1552 Urtizberea, A., Dupont, N., Rosland, R., & Aksnes, D. L. (2013). Sensitivity of euphotic zone
1553 properties to CDOM variations in marine ecosystem models. *Ecological Modelling*, 256,
1554 16–22. <https://doi.org/10.1016/j.ecolmodel.2013.02.010>
- 1555 Vähätalo, A. V., Salkinoja-Salonen, M., Taalas, P., & Salonen, K. (2000). Spectrum of the
1556 quantum yield for photochemical mineralization of dissolved organic carbon in a humic
1557 lake. *Limnology and Oceanography*, 45(3), 664–676.
1558 <https://doi.org/10.4319/lo.2000.45.3.0664>
- 1559 Vähätalo, A. V., Salonen, K., Münster, U., Järvinen, M., & Wetzel, R. G. (2003).
1560 Photochemical transformation of allochthonous organic matter provides bioavailable
1561 nutrients in a humic lake. *Archiv Fur Hydrobiologie*, 156(3), 287–314.
1562 <https://doi.org/10.1127/0003-9136/2003/0156-0287>
- 1563 Ward, C. P., Nalven, S. G., Crump, B. C., Kling, G. W., & Cory, R. M. (2017). Photochemical
1564 alteration of organic carbon draining permafrost soils shifts microbial metabolic
1565 pathways and stimulates respiration. *Nature Communications*, 8(1), 1–7.
1566 <https://doi.org/10.1038/s41467-017-00759-2>
- 1567 Ward, C. P., Bowen, J. C., Freeman, D. H., & Sharpless, C. M. (2021). Rapid and
1568 reproducible characterization of the wavelength dependence of aquatic photochemical
1569 reactions using light-emitting diodes. *Environmental Science and Technology Letters*,
1570 8(5), 437–442. <https://doi.org/10.1021/acs.estlett.1c00172>
- 1571 Weishaar, J. L., Aiken, G. R., Bergamaschi, B. A., Fram, M. S., Fujii, R., & Mopper, K.

1572 (2003). Evaluation of Specific Ultraviolet Absorbance as an Indicator of the Chemical
1573 Composition and Reactivity of Dissolved Organic Carbon. *Environmental Science &*
1574 *Technology*, 37(20), 4702–4708. <https://doi.org/10.1021/es030360x>

1575 White, E. M., Kieber, D. J., Sherrard, J., Miller, W. L., & Mopper, K. (2010). Carbon dioxide
1576 and carbon monoxide photoproduction quantum yields in the Delaware Estuary. *Marine*
1577 *Chemistry*, 118(1–2), 11–21. <https://doi.org/10.1016/j.marchem.2009.10.001>

1578 Wit, F., Rixen, T., Baum, A., Pranowo, W. S., & Hutahaean, A. A. (2018). The Invisible
1579 Carbon Footprint as a hidden impact of peatland degradation inducing marine carbonate
1580 dissolution in Sumatra, Indonesia. *Scientific Reports*, 8(1), 17403.
1581 <https://doi.org/10.1038/s41598-018-35769-7>

1582 Zepp, R. G. (2007). Solar UVR and aquatic Carbon, nitrogen, sulfur and metals cycles. In E.
1583 W. Helbling & H. Zagarese (Eds.) (pp. 137–184). Cambridge: Royal Society of
1584 Chemistry. <https://doi.org/10.1039/9781847552266-00137>

1585 Zhou, Y., Martin, P., & Müller, M. (2019). Composition and cycling of dissolved organic
1586 matter from tropical peatlands of coastal Sarawak, Borneo, revealed by fluorescence
1587 spectroscopy and parallel factor analysis. *Biogeosciences*, 16(13), 2733–2749.
1588 <https://doi.org/10.5194/bg-16-2733-2019>

1589 Zhou, Y., Evans, C. D., Chen, Y., Chang, K. Y. W., & Martin, P. (2021). Extensive
1590 Remineralization of Peatland-Derived Dissolved Organic Carbon and Ocean
1591 Acidification in the Sunda Shelf Sea, Southeast Asia. *Journal of Geophysical Research:*
1592 *Oceans*, 126(6), 1–23. <https://doi.org/10.1029/2021JC017292>

1593 Zika, R. G. (1981). Chapter 10 Marine Organic Photochemistry. In *Elsevier Oceanography*

1594 *Series* (Vol. 31, pp. 299–325). [https://doi.org/10.1016/S0422-9894\(08\)70332-5](https://doi.org/10.1016/S0422-9894(08)70332-5)

1595

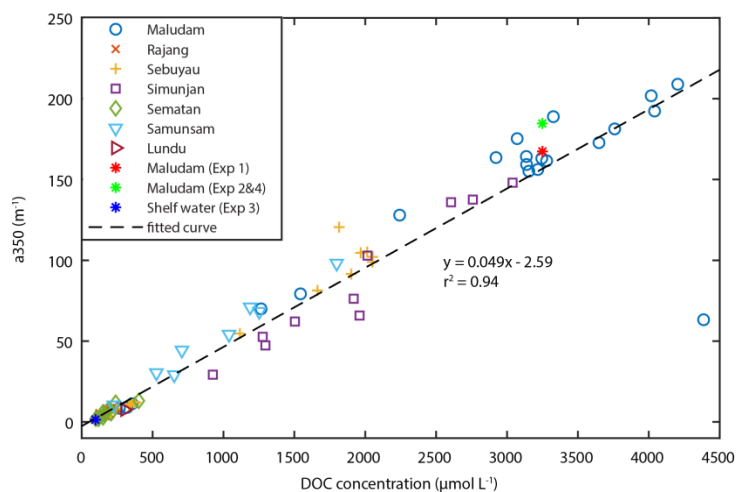
1596

1597

1598

1599

1600 **A3 Supplementary Figures and Tables**



1601

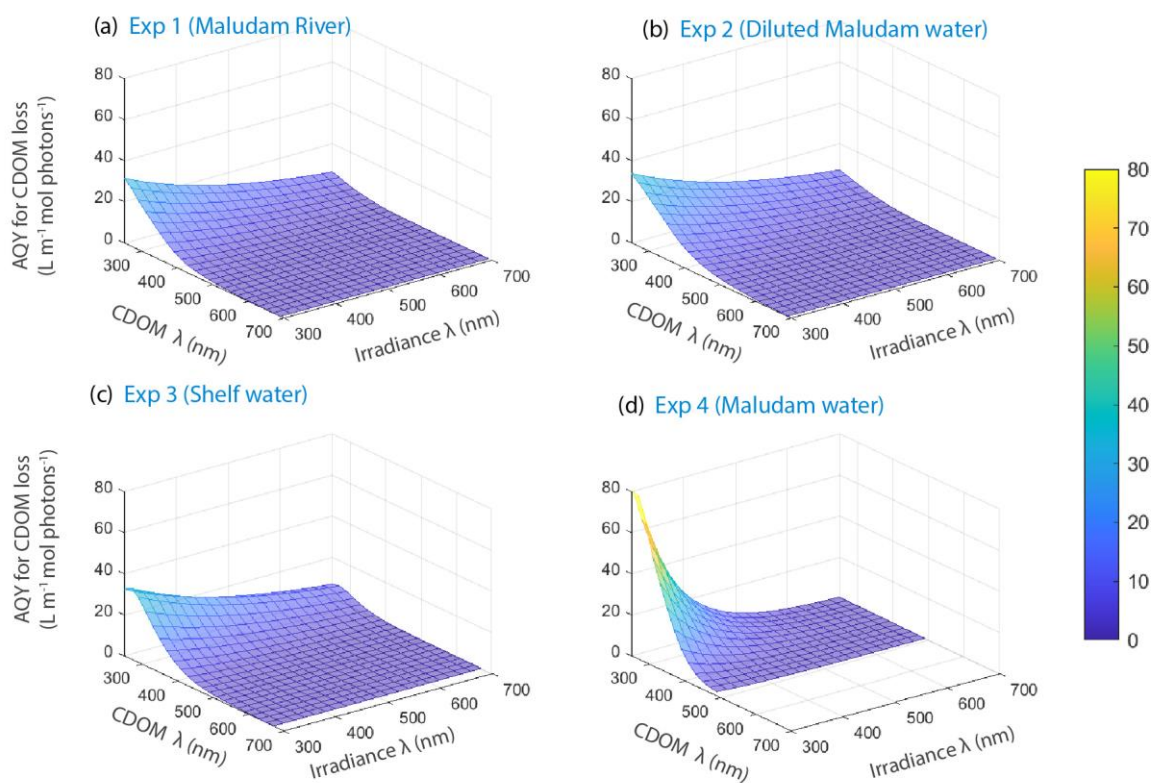
1602 Figure S1. Relationship between DOC concentration and CDOM absorption (a_{350}) across

1603 different rivers in Sarawak, Borneo (data from Martin et al. 2018), and in the shelf sea water

1604 sample collected in the Singapore Strait for Exp 3. Samples used to determine tDOC AQY in

1605 this study follow the relationship.

1606



1607

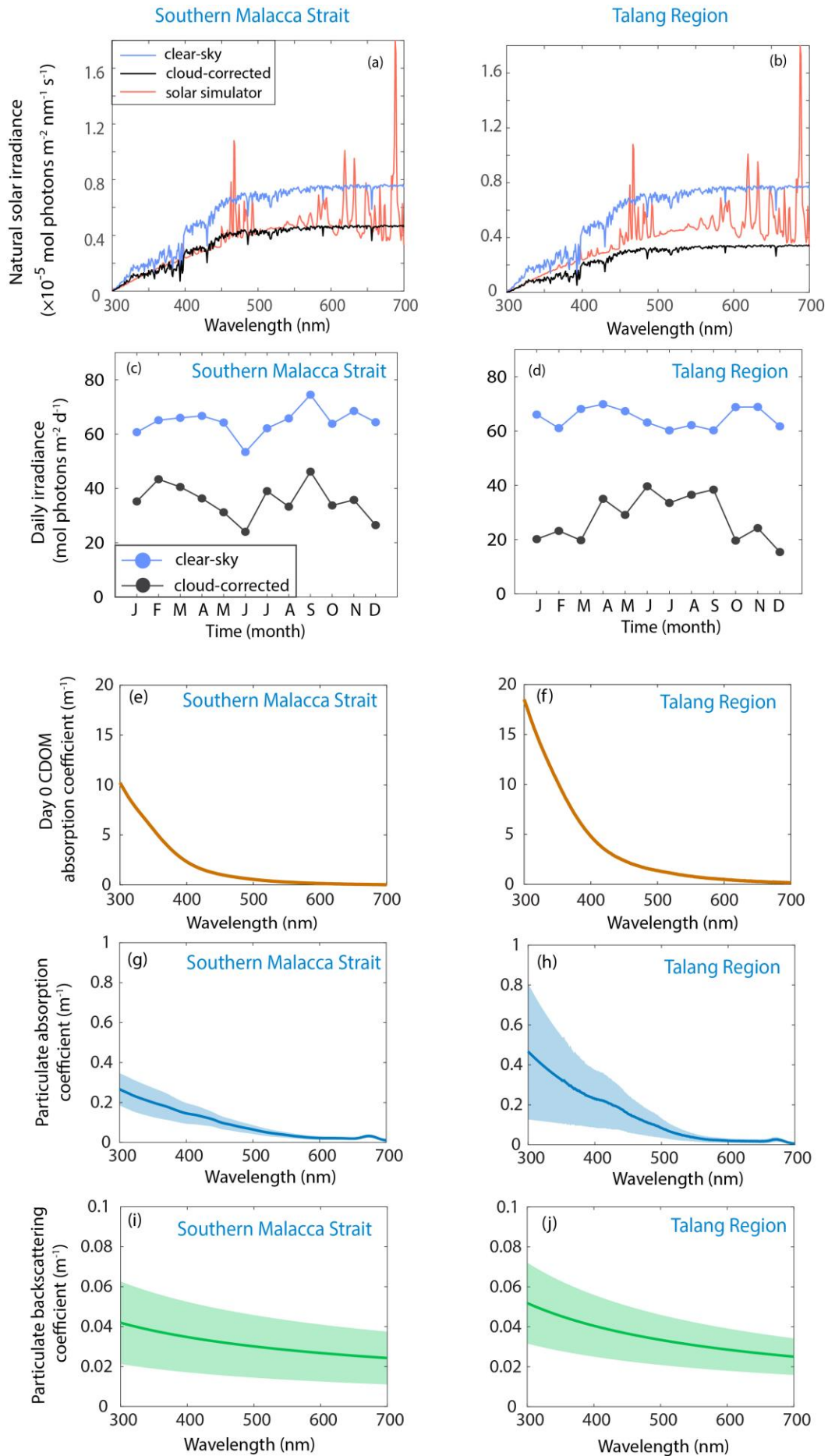
1608 Figure S2. Photochemical efficiency spectra for CDOM photobleaching, i.e. decrease in
 1609 volume-integrated absorption coefficient, calculated from data of Exp 1–4. In Exp 4, the
 1610 AQY for CDOM photobleaching above 500 nm of the CDOM absorption spectrum were
 1611 given in negative values, due to the measurement noise of CDOM absorption at the longer
 1612 wavelengths, and thus omitted.

1613

1614

1615

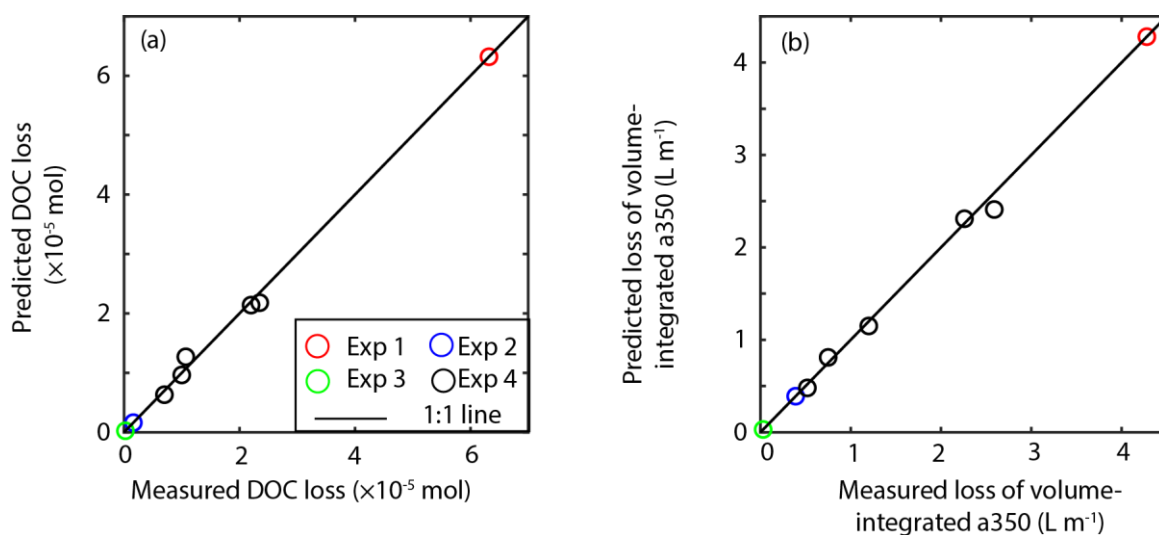
1616



1618 Figure S3. Model input data for both modeling regions. (a) – (b) Annual mean noon-time (12
 1619 pm local time) natural solar irradiance under clear-sky and cloud-corrected conditions for
 1620 both modeling regions, compared with the irradiance of the solar simulator for Exp 1–4. (c)–
 1621 (d) Seasonal variations in the daily irradiance under clear-sky and cloud-corrected conditions.
 1622 Daily irradiance for each month was integrated over 300 to 700 nm and 24 hours. (e)–(f)
 1623 Initial CDOM absorption spectra (i.e. in Day 0). (g)–(h) Particulate absorption spectrum. (i)–
 1624 (j) Particulate backscattering spectrum. The shading in panels g–j indicates the uncertainties
 1625 of the spectra calculated from all the spectrum for estimating the model output by Monte
 1626 Carlo simulation.

1627

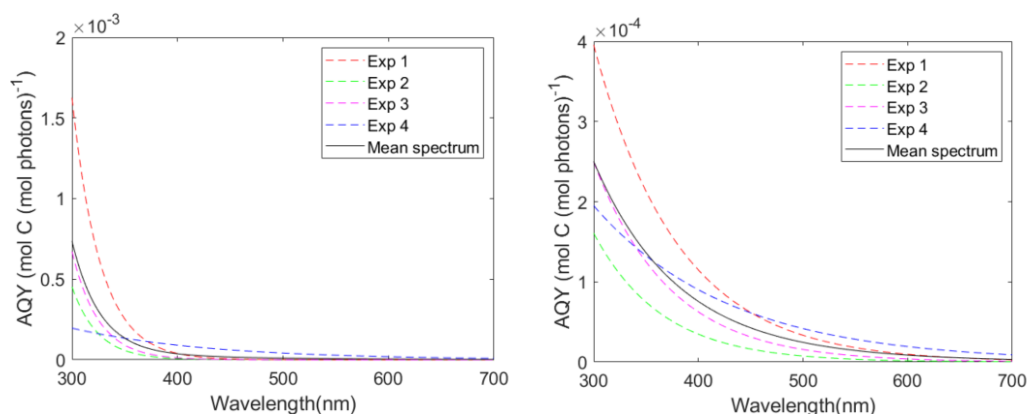
1628



1629

1630 Figure S4. Comparison of the measured and the optimized AQY-predicted (a) loss of DOC
 1631 and (b) loss of the volume-integrated a_{350} of CDOM of Exp 1 – 4. Data of Exp 4 were from
 1632 the multiple cut-off filters treatments.

1633



1634

1635

Figure S5. The AQY spectra of DOC photo-rem mineralization optimized using a

1636

starting value for c of 100 (left pane) and 0.01 (right pane). The AQY spectra in Fig.

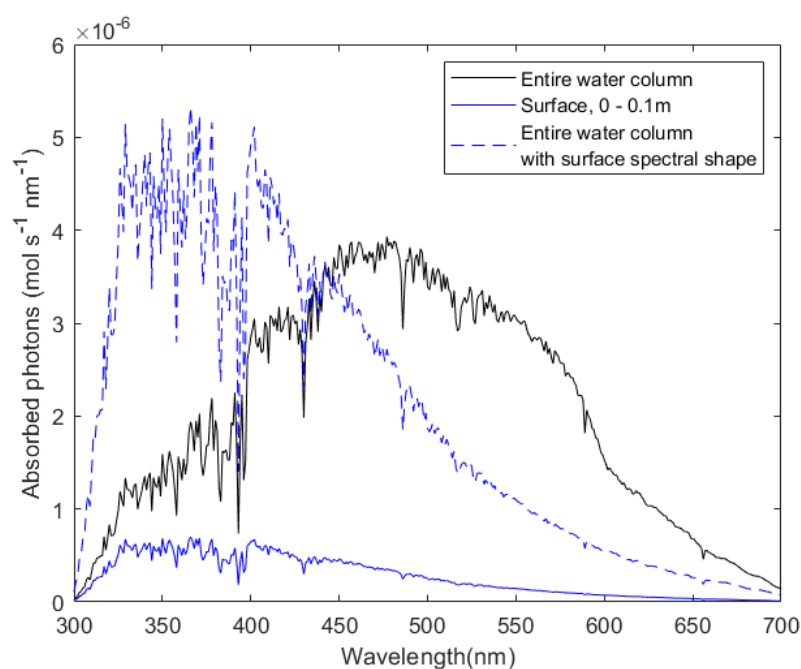
1637

4a in the original draft were optimized using a starting value of 1.0 as in Aarnos et al.,

1638

(2018).

1639



1640

1641 Figure S6. Spectra of photons absorbed by CDOM at the water surface (0 – 0.1m, solid blue
 1642 line) and depth-integrated for the entire water column (solid black line) in our model for a
 1643 1-m² grid in the Southern Malacca Strait region with irradiance spectrum at noon of July
 1644 2019. The dashed blue line shows a hypothetical absorbed photon spectrum for the same total
 1645 quantity of absorbed photons as for the black line, but with surface spectral shape (dashed
 1646 blue line). The broadband AQY from our photodegradation experiments could only be

1647 applied accurately to the whole water column if the spectrum of absorbed photons followed
1648 the dashed blue line, but in fact the absorbed photon spectrum is greatly shifted to longer
1649 wavelengths.

1650

1651

1652

1653 Table S1. Results from nitrite actinometry conducted following Jankowski et al., (1999). We
1654 measured the photo-production of salicylic acid in incubations in the Suntest solar simulator
1655 using experimental conditions as for our tDOC photodegradation experiments. The
1656 theoretically predicted photo-production of salicylic acid was calculated from the apparent
1657 quantum yield of salicylic acid production, the absorption spectrum of nitrite, and the
1658 irradiance spectrum of the test chamber as measured by the FLAME radiometer. The
1659 measured and predicted salicylic concentrations agree to within 6%, indicating that the
1660 irradiance spectrum measured by our radiometer can well represent the irradiance received
1661 inside the quartz cuvette we used for the photodegradation experiments.

1662

Cut-off wavelength of the optical filter used	Predicted salicylic acid concentration (nM)	Measured salicylic acid concentration (nM)	% difference
295nm	163	168	-2.97
320nm	151	160	-5.63

1663

1664

1665

1666

1667 Table S2. Variables in the photodegradation model.

Variable	Definition	Unit
a_{CDOM}	CDOM absorption coefficient	m^{-1}
a_w	Water absorption coefficient	m^{-1}
a_p	Particulate absorption coefficient	m^{-1}

bb_w	Water backscattering coefficient	m^{-1}
bb_p	Particulate backscattering coefficient	m^{-1}
K_d	Downwelling attenuation coefficient	m^{-1}
$E_{d,0+}$	Solar irradiance just above the sea surface	$mol\ photons\ m^{-2}\ s^{-1}$
$E_{d,0-}$	Solar irradiance just below the sea surface	$mol\ photons\ m^{-2}\ s^{-1}$
$\bar{\epsilon}$	Photons absorbed by CDOM	mol
λ	Wavelength	nm
θ	Solar zenith angle	degree
ϕ_{DOC}	Apparent quantum yield for photo-remineralization of DOC	$Mol\ DOC\ (mol\ photons)^{-1}$
ϕ_{CDOM}	Apparent quantum yield for photo-induced loss of volume-integrated CDOM absorption coefficient. For example ϕ_{a350} is the apparent quantum yield for the photo-induced loss of volume-integrated CDOM absorption coefficient at 350nm.	$L\ m^{-1}\ (mol\ photons)^{-1}$

1668

1669

1670

1671

1672 Table S3. Changes in DOC and CDOM parameters during photodegradation experiments.

	DOC ($\mu\text{mol L}^{-1}$)	a_{350} (m^{-1})	$S_{275-295}$ (nm^{-1})	SUVA ₂₅₄ (L mg^{-1} m^{-1})
Exp 1 (Maludam River water, 416 hours)				
Initial	3250	167.4	0.011	5.41
End	850	5.9	0.021	1.23
%loss	74%	96%		
Exp 2 (diluted Maludam water, 462 hours)				
Initial	204	13.5	0.010	6.06
End	150	0.6	0.032	1.61
%loss	26%	96%		
Exp 3 (Singapore water during tDOC input, 500 hours)				
Initial	97	1.4	0.018	2.40
End	88	0.3	0.032	1.53
%loss	9%	79%		
Exp 4 (Maludam River water, 144hours, no-optical-filer treatment)				
Initial	3249	184.7	0.011	5.87

End	2268	85.9	0.014	4.52
%loss	30%	54%		

1673

1674

1675

1676

1677 Table S4. The broadband Apparent Quantum Yield (AQY) for DOC photo-remineralization
 1678 calculated for different time intervals from Exp 1 – 3. We did not observe a steady decrease in
 1679 AQY over time. Only data before DOC concentration stopped to decrease were used to
 1680 calculate AQY.

Exp No.	Time Interval (hour)	DOC loss (μmol) within the quartz cell	Absorbed photons (mol) Integrated over 290–700 nm	Broadband AQY ($\mu\text{mol C mol photons}^{-1}$)
1 (Maludam Water)	0 – 72	15	0.15	100
	72 – 144	10	0.14	74
	144 – 216	8	0.12	64
	216 – 288	10	0.10	101
	288 – 258	12	0.08	153
	358 – 431	7	0.07	110
	0 – 431	63	0.66	95
2 (Maludam mixed with seawater)	0 – 51	0.33	0.014	25
	51 – 111	0.42	0.0087	48
	111 – 188	0.12	0.0069	16
	188 – 268	0.048	0.0044	11
	268 – 362	0.36	0.0028	128
	362 – 462	0.35	0.0019	178
	0 – 462	1.61	0.0383	42

3 (Singapore Strait)	0 – 24	0.078	0.00063	123
	24 – 70.5	0.075	0.00094	80
	70.5 – 119	0.017	0.00073	23
	119 – 170.5	0.074	0.00056	133
	0 – 170.5	0.24	0.0029	85

1681

1682

1683 Table S5. Simulation results of tDOC remineralization by photodegradation in the Southern
 1684 Malacca Strait using broadband AQY in the model, showing much larger tDOC loss
 1685 compared to the results based on spectrally-resolved AQY (summarized in Table 2).

Conditions	Initial ($\mu\text{mol L}^{-1}$)	Final ($\mu\text{mol L}^{-1}$)	%loss
Clear-sky	108	45	58%
Cloud-corrected	108	63	42%

1686

1687

1688

1689

1690

1691 Table S6. Comparison of modelling results between using different starting values of
 1692 coefficient c for optimizing AQY spectra.

	Initial DOC ($\mu\text{mol/L}$)	Final DOC ($\mu\text{mol/L}$)		
Starting value used		0.01	1.0	100
Southern Malacca Strait, cloud corrected	108	81	86	88
Talang Region, cloud corrected	181	173	174	176

1693

1 Quantifying photodegradation of peatland-derived dissolved organic carbon in
2 the coastal ocean of Southeast Asia

3

4 Yongli Zhou^{1,*}, Moritz Müller², Nagur Cherukuru³, Patrick Martin^{1,*}

5

6 ¹Asian School of the Environment, Nanyang Technological University, 639798 Singapore

7 ²Faculty of Engineering, Computing and Science, Swinburne University of Science and
8 Technology, 93350 Kuching, Sarawak, Malaysia

9 ³CSIRO Oceans and Atmosphere Flagship, Canberra ACT 2601, Australia

10 †Current address: the Ecosystems Center, Marine Biological Laboratory, Woods Hole, 02543,
11 United States

12

13 Email:

14 Yongli Zhou*: zhou0303@e.ntu.edu.sg

15 Moritz Müller: mmueller@swinburne.edu.my

16 Nagur Cherukuru: Nagur.Cherukuru@csiro.au

17 Patrick Martin*: pmartin@ntu.edu.sg

18 *Corresponding author(s)

19

20

21

22 **Abstract**

23 The terrigenous dissolved organic carbon (tDOC) exported from the peatlands in Southeast
24 Asia appears to be extensively remineralized in the shelf sea, but the processes that drive this
25 remineralization remain unclear. Here, we combined incubation experiments and model
26 simulations to quantify the rate and extent of photodegradation of tDOC in the Sunda Shelf
27 Sea. Laboratory photodegradation experiments indicate that up to 74% of the peatland tDOC
28 is potentially labile to photochemical remineralization. Based on our estimated apparent
29 quantum yield for tDOC remineralization, modeled *in-situ* solar irradiance, and measured
30 inherent optical properties of the water column, we simulated peatland tDOC
31 photoremineralization for two coastal regions of the Sunda Shelf Sea. These simulation
32 results show that natural solar radiation can directly remineralize $20\pm 11\%$ of tDOC over 2
33 years, which corresponds to the approximate residence time of water in the Sunda Shelf Sea,
34 and that significant photobleaching of tDOC can occur in coastal waters over shorter
35 time-scales. We further derived a simplified photochemical decay constant ϕ^{ref} of 0.008–
36 0.017day^{-1} for Southeast Asia's peatland-derived tDOC, which can be used to parameterize
37 the recently proposed UniDOM model framework. We conclude that direct photodegradation
38 may be a greater sink for tDOC in Southeast Asia's coastal ocean compared to higher
39 latitudes, although it is insufficient to account for the total tDOC remineralization observed in
40 the Sunda Shelf Sea.

41

42

43 **Plain Language Summary**

44 Tropical peatlands in Southeast Asia are contributing large quantity of organic carbon to the
45 coastal ocean. This organic carbon flux is rapidly decomposed to CO₂ but the mechanism of
46 this extensive remineralization is unclear. Organic carbon from peatlands appears to be easily
47 decomposed upon exposure to sunlight, known as photodegradation. In this study, we
48 conducted incubation experiments to collect data of photochemical decay efficiency of
49 peatland-derived organic carbon and developed model simulation to calculate, in natural
50 coastal waters, how much of the organic carbon is decomposed via the pathway of
51 photodegradation. Our data show that sunlight radiation can directly cause a loss of 20% of
52 the peatland-derived organic carbon input in the coastal ocean of Southeast Asia, indicating
53 that photodegradation contribute to a larger portion of the total organic carbon decomposition
54 in Southeast Asia than in coastal oceans at the higher latitudes. In addition, our data allowed
55 us to derive region-specific decay rates of photodegradation for coastal ocean of Southeast
56 Asia, which can be used to parameterize large-scale aquatic organic carbon biogeochemistry
57 model.

58

59

60

61

62

63

64 **1 Introduction**

65

66 The biogeochemical fate of terrigenous dissolved organic carbon (tDOC) in the ocean is still
67 poorly understood. This is important in the context of the global carbon cycle, because the
68 riverine input and the biogeochemical processing of tDOC can have significant impacts on
69 coastal marine environments. Intact tDOC can absorb sunlight and lead to ecologically
70 harmful “coastal darkening” by shoaling the euphotic zone and altering the spectral quality of
71 light underwater (Aksnes et al., 2009; Martin et al., 2021; Urtizberea et al., 2013). Moreover,
72 a significant fraction of tDOC may undergo remineralization in shelf seas, as shown for the
73 Eurasian Shelf (Kaiser et al., 2017), the North Sea (Painter et al., 2018), the Louisiana Shelf
74 (Fichot & Benner, 2014), and the Sunda Shelf (Wit et al., 2018; Zhou et al., 2021). In some
75 regions, remineralization of tDOC is sufficiently large to cause ocean acidification
76 (Semiletov et al., 2016; Wit et al., 2018; Zhou et al., 2021) and to drive strong sea-to-air CO₂
77 fluxes (Cai, 2011; Kitidis et al., 2019; Wit et al., 2018; Zhou et al., 2021). However, the
78 *in-situ* rates and extent of tDOC degradation that control these environmental impacts remain
79 poorly constrained.

80

81 The degradation of tDOC is influenced by its optical properties. Rich in colored dissolved
82 organic matter (CDOM) (Massicotte et al., 2017), tDOC can absorb ultraviolet and visible
83 solar radiation (Zepp, 2007). Meanwhile, the abundant unsaturated bonds of the tDOC pool
84 are subject to cleavage upon absorbing radiant energy, leading to a series of photochemical

85 reactions (Zika, 1981). These reactions can cause removal of CDOM (i.e., photobleaching)
86 (Helms, Stubbins, et al., 2013; Tzortziou et al., 2007), complete oxidation of tDOC into CO₂
87 (i.e., photo-remineralization) (Allesson et al., 2021; Mopper et al., 1991; Moran et al., 2000),
88 and chemically alter tDOC molecules (i.e., photo-modification) in a way that renders them
89 more labile to microbial degradation (Dittmar et al., 2007; Stubbins et al., 2010, 2017). The
90 findings that tDOC derived from peatlands of the Congo Basin (Spencer et al., 2009;
91 Stubbins et al., 2010) and of Southeast Asia (Martin et al., 2018; Zhou et al., 2021) is highly
92 photo-labile imply that photodegradation can play an important role in the biogeochemical
93 cycling of tropical peatland tDOC.

94

95 Recently, Aarnos et al. (2018) estimated that direct photo-remineralization can cause a loss of
96 18% of the global riverine tDOC flux in the ocean, based on the relationship between tDOC
97 loss and CDOM loss derived from incubation experiments, and the assumption that all
98 riverine CDOM is photochemically destroyed. However, quantification of the *in-situ* rates
99 and the extent of tDOC photodegradation via realistic modeling is challenging because it
100 requires data for the inherent photochemical properties of the tDOC (i.e., photo-lability and
101 apparent quantum yield), the *in-situ* solar irradiance, and the underwater light field; this
102 requires combining data from incubation experiments, field measurements, satellite
103 observations and meteorological models. To date, such modelling has only been performed in
104 a few cases, such as the Louisiana Shelf (Fichot & Benner, 2014) and the Baltic Sea (Aarnos
105 et al., 2012). Fichot & Benner (2014) concluded that direct photo-remineralisation only

106 consumes 8% of the riverine tDOC input. In contrast, Aarnos et al. (2012) found that the
107 annual DOC photoremineralization exceeds the riverine DOC supply in the Baltic, and
108 concluded that photoremineralization is likely an important tDOC sink in the Baltic Sea.
109 However, for most shelf sea regions we have little understanding of *in-situ* tDOC
110 photo-remineralization, which limits our ability to predict how anthropogenically driven
111 changes to tDOC fluxes might impact coastal ecosystems (Ciais et al., 2013). Although
112 modeling frameworks are being developed to represent the biogeochemistry of tDOC across
113 the land-ocean aquatic continuum (Anderson et al., 2019) and to integrate coastal carbon
114 cycling processes in global ocean models (Mathis et al., 2022), appropriate rate constants for
115 tDOC remineralization are still very poorly constrained.

116

117 In this study, we attempt to estimate *in-situ* photodegradation rates for one of the world's
118 hotspots of riverine tDOC export: Southeast Asia. Rivers draining the peatlands in this region
119 deliver ~21 Tg C of tDOC to the Sunda Shelf Sea annually, which could account for ~10% of
120 the global fluvial tDOC flux (Baum et al., 2007; S. Moore et al., 2011). It appears that at least
121 60–70% of this peatland-derived tDOC is rapidly remineralized in the Sunda Shelf Sea after
122 estuarine mixing (Wit et al., 2018; Zhou et al., 2021). Photodegradation might play an
123 important role here because Southeast Asia's peatland tDOC appears to be highly photo-labile
124 (>70% photo-remineralizable) (Martin et al., 2018; Zhou et al., 2021) but much less
125 bio-labile (Nichols & Martin, 2021). In addition, because of the greater solar irradiance
126 year-round in the tropics (Apell & McNeill, 2019), photodegradation might be a stronger

127 tDOC sink in the Sunda Shelf Sea compared to higher latitudes.

128

129 We incubated riverine and shelf water samples with simulated sunlight to determine the
130 photo-degradability and photochemical efficiency (apparent quantum yield) of tDOC
131 remineralization. We then developed a spectrally resolved optical model based on previous
132 work (Aarnos et al., 2012, 2018; Fichot & Benner, 2014) to estimate the *in-situ* rates and
133 extent of tDOC photo-remineralization, and CDOM photobleaching, for two coastal regions
134 of the Sunda Shelf Sea. We further used our results to estimate a simplified photochemical
135 decay constant that can be applied in ocean biogeochemical models using the recently
136 proposed Unified Model of Dissolved Organic Matter model (Anderson et al., 2019). This
137 will assist to integrate tDOC processing into larger-scale carbon cycle models, especially in
138 Southeast Asia.

139

140

141 **2 Materials and Methods**

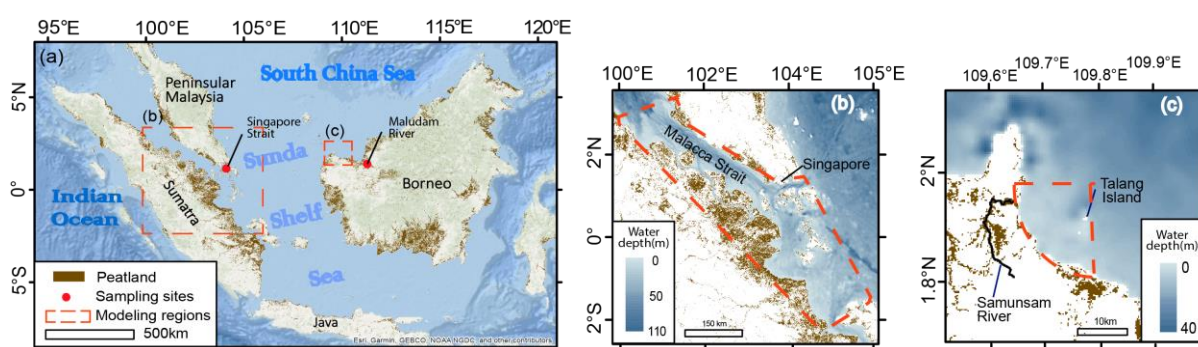
142 **2.1 Overview of study area**

143 Southeast Asia's peatlands are found mainly in the coastal lowlands of Sumatra and Borneo
144 (Fig. 1a). The peat-draining rivers deliver tDOC into the Sunda Shelf Sea, where the oceanic
145 currents and movement of tDOC are controlled by the monsoon (Mayer et al., 2018; Susanto
146 et al., 2016). During the Northeast Monsoon (November to February), water flows from the
147 South China Sea into the central shelf sea and flows towards the Java Sea and the Malacca

148 Strait; during the Southwest Monsoon (May to August), the currents reverse and carry the
149 tDOC input from the Sumatran rivers into the central Sunda Shelf. After a residence for 1–2
150 years in the shelf sea, the tDOC exits into the open Indian Ocean through the Malacca Strait,
151 the Sunda Strait, or the Lombok Strait.

152

153



154

155 Figure 1. (a) Distribution of peatlands in Southeast Asia and locations of water sampling sites
156 (the Maludam River and the Singapore Strait) and modeling regions. (b) – (c) Red dashed
157 lines encircle the modeling regions, with bathymetry shown: (b) the Southern Malacca Strait
158 (receives input from the Sumatran peatlands) and (c) the Talang Region (receives tDOC input
159 from the Samunsam River). Peatland distribution was obtained from the Center for
160 International Forestry Research, Indonesia (<https://www2.cifor.org/global-wetlands/>).
161 Bathymetry data were obtained from the GEBCO_2020 grid (GEBCO Compilation Group,
162 2020).

163

164 2.1.1 Sampling sites and water collection for photodegradation experiments

165 To obtain photochemical data of peatland tDOC, we collected two surface water samples (0–

166 1 m depth) from the Maludam River (1.636°N 111.049°E) in Sarawak, Borneo in December
167 2017 and June 2019 and one from the Singapore Strait (1.226°N, 103.860°E) in the coastal
168 Sunda Shelf Sea in July 2020 (Figure 1). The Maludam River samples were gravity-filtered
169 through pre-rinsed 0.22 µm pore-size Whatman Polycap filters on the day of collection and
170 filtered again through pre-rinsed 0.22 µm pore-size polyethersulfone membrane filters upon
171 arrival at Nanyang Technological University, Singapore. The Singapore Strait shelf water
172 sample was filtered through pre-rinsed 0.22 µm pore-size polyethersulfone membrane filters
173 on the day of collection. All filtered water samples were kept at 4°C in the dark and filtered
174 again through pre-rinsed 0.22 µm pore-size polyethersulfone membrane filters before
175 experiments.

176

177 Samples from these two sites are representative of the tDOC exported from peatlands into our
178 modeling regions of the coastal ocean, because multiple lines of evidence suggest that the
179 underlying optical and photochemical characteristics of tDOC are similar across the peatlands
180 of Southeast Asia. The Maludam River drains one of the largest remaining intact peatlands in
181 Malaysia, and its catchment consists exclusively of peatlands (Müller et al., 2015). The
182 Maludam samples therefore allow us to obtain AQY estimates for tDOC that is freshly
183 released from a peatland, and that are not influenced by contributions of DOC from other soil
184 types or anthropogenic input. In contrast, the Singapore Strait receives substantial tDOC
185 input from Sumatran peatlands between May and September when tDOC comprises ~50% of
186 the bulk DOC pool, but this tDOC has already undergone fairly extensive remineralization

187 prior to reaching the Singapore Strait (Zhou et al. 2021). This allows us to estimate the AQY
188 for peatland tDOC that has already undergone some degree of biogeochemical processing in
189 the shelf sea. As a purely peatland-draining river, the Maludam has high DOC concentrations
190 (3000–4000 $\mu\text{mol l}^{-1}$). Although different rivers across Sumatra and Borneo can vary around
191 10-fold in DOC concentration, the DOC concentration is linearly related to the proportion of
192 catchment area that is peatland (Rixen et al., 2022). Moreover, across multiple rivers in
193 northwestern Borneo draining catchments with varying peatland proportions and DOC
194 concentrations, there is a strong and linear relationship between DOC concentration and
195 CDOM absorption (Fig. S1, data from (Martin et al., 2018)). This suggests that the
196 concentration of tDOC varies according to the extent of peatland cover in a catchment, but
197 that the optical properties of the tDOC pool are then very similar across rivers, including the
198 Maludam. In addition, the stable carbon isotope composition of DOC ($\delta^{13}\text{C}_{\text{DOC}}$) is very
199 similar across peatland-draining rivers on Sumatra, Borneo, and Peninsular Malaysia, mostly
200 between -28‰ and -30‰ (data compiled in (Zhou et al., 2021)), and these peatlands share
201 many similarities in plant species (Giesen et al., 2018) and climatic conditions. This further
202 suggests that the photochemical and optical characteristics of the peat-derived tDOC pool
203 should be similar between rivers across the region. This is also supported by our data (see
204 below) that the photochemical efficiency (i.e., apparent quantum yield) of DOC is similar
205 between the Singapore Strait water and the Maludam River water.

206

207

208 **2.1.2 Modeling regions**

209 Using our experimental data, we simulated photo-remineralization of tDOC and
210 photobleaching of CDOM for two regions of the Sunda Shelf Sea: the southern Malacca
211 Strait and the Talang Region in Sarawak, Borneo (Fig. 1). Selection of the modeling regions
212 was based on the following considerations. First, both regions receive large riverine input of
213 tDOC from peatlands (Martin et al., 2018; Wit et al., 2018; Zhou et al., 2019, 2021). Second,
214 previous work has indicated the possibility of a significant contribution of photodegradation
215 in both regions: it potentially drives a major part of the tDOC remineralization observed in
216 the shelf sea (Zhou et al., 2021) and the removal of terrigenous CDOM (Kaushal et al., 2021).
217 Third, measurements of the water column inherent optical properties (i.e., particulate
218 absorption and backscattering) are available for both regions (Cherukuru et al., 2021; Martin
219 et al., 2021).

220

221 We ran simulations over different durations for the two regions to accomplish two different
222 objectives. The simulation for the southern Malacca Strait aimed to quantify the contribution
223 of photodegradation to the total quantity of tDOC remineralization observed in this region of
224 the shelf sea, where the water residence time is up to approximately 2 years (Mayer et al.,
225 2015). In contrast, the simulation for the Talang Region aimed to test whether photobleaching
226 of tDOC is sufficiently rapid to contribute to the seasonal variability of CDOM observed at
227 the Talang Islands (Kaushal et al., 2021), where the water residence time is much shorter
228 (Mayer et al., 2015).

229

230 The southern Malacca Strait encompasses the shelf waters near the largest peatland area on
231 Sumatra, including the southern part of the Malacca Strait, the Singapore Strait, and the
232 waters to the north of Bangka Island, Indonesia (Fig. 1b). It receives substantial terrestrial
233 input from the Sumatran peatlands by riverine runoff, and it was found that 60–70% of the
234 tDOC is remineralized on the shelf (Wit et al., 2018; Zhou et al., 2021). Based on the water
235 residence time of 1–2 years within this region of the Sunda Shelf (Mayer et al., 2015), we
236 simulated photodegradation for 2 years to quantify a likely upper boundary for the
237 photochemical contribution to the total quantity of tDOC remineralization.

238

239 Waters in the Talang Region in Sarawak receive peatland tDOC input carried by the
240 Samunsam River (Fig. 1c). Skeletal luminescence in a coral core from the Talang Island
241 showed seasonal variability terrigenous CDOM levels, with very low values during the
242 Southwest Monsoon (May to August) (Kaushal et al., 2021). This seasonal decrease in the
243 CDOM signal in coral skeletons was argued to be greater than the expected seasonal decrease
244 in the riverine CDOM flux, but closely matched the seasonal changes in solar irradiance
245 (higher during Southwest Monsoon, Fig. S2d). This might indicate a significant role for
246 photodegradation in removing more tDOC and CDOM in the coastal waters during
247 Southwest Monsoon (Kaushal et al., 2021). To test this hypothesis, we estimated the
248 photo-remineralization and photobleaching for different periods of the year.

249

250

251 **2.2 Photodegradation experiments for AQY determination**

252 We performed four photodegradation experiments (Exp 1, 2, 3, and 4 below, Table 1) with the
253 water samples from the Maludam River and the Singapore Strait. The changes in DOC
254 concentration and CDOM during Exp 1 and Exp 3 were reported previously (Zhou et al.,
255 2021). Here, we use the data further to calculate the AQY.

256

257 In Exp 1, we aimed to quantify the proportion of the peatland-derived tDOC that is
258 photo-remineralizable and to calculate the AQY. We incubated the Maludam sample collected
259 in December 2017 with simulated sunlight, monitored the DOC concentration and CDOM
260 absorption over time, and terminated the experiment when no additional DOC loss was
261 observed (after 816 hours). However, photo-flocculation of DOC was observed at 525 hours,
262 so we only used the data up until the previous time point at 416 hours to calculate the AQY.

263

264 In Exp 2, we aimed to quantify the AQY after simulating the mixing of tDOC into the coastal
265 ocean. We diluted 65 ml of the Maludam sample collected in June 2019 with 935 ml of
266 artificial seawater (0.2 g NaHCO₃ [Sigma-Aldrich S6014] and 32.09 g NaCl [Sigma-Aldrich
267 S9888] in 1 L ultrapure deionized water [18.2 MΩ cm⁻¹]), achieving a salinity of ~29. We
268 exposed the mixed sample to simulated sunlight, monitored the changes in DOC and CDOM,
269 and terminated the experiment after >25% of DOC was lost (462 hours).

270

271 In Exp 3, we aimed to quantify the proportion of tDOC in the shelf water that was still
 272 photo-remineralizable after it had already experienced extensive prior degradation in the
 273 environment (Zhou et al., 2021). We incubated the Singapore Strait sample with simulated
 274 sunlight until no additional DOC loss was observed, which was after 500 hours. Because we
 275 previously found that a marine DOC-dominated sample of shelf seawater from Singapore
 276 Strait (sample collected in January when there was little tDOC input) showed no
 277 photochemical loss of DOC (Fig. 7i in Zhou et al. 2021), the loss of DOC observed in Exp 3
 278 was attributed entirely to photochemical loss of tDOC.

279

280 In Exp 4, we aimed to further constrain the AQY of tDOC with a spectrally resolved
 281 experiment. We incubated the Maludam sample collected in June 2019 with simulated
 282 sunlight under Schott long-pass filters with cut-offs at 295nm, 320nm, 395nm, 420nm, and
 283 455nm. We terminated the experiment after 144 hours, once the DOC and CDOM loss were
 284 sufficiently large to calculate the AQY.

285

286

287 Table 1. Summary of the four photodegradation experiments.

	Sample	Duration (hour)
Exp 1	Maludam River water (Dec 2017)	416
Exp 2	Maludam River water (June 2019) diluted with artificial seawater	462

Exp 3	Shelf water during tDOC input (July 2020)	500
Exp 4	Maludam River water (June 2019) with optical cut-off filters	144

288

289

290 In all four experiments, water samples (30 ml) were filled into 14 replicate cylindrical quartz
291 cells (Starna Cells, 50 mm pathlength, 50 mm diameter, with Teflon screw caps) and
292 irradiated in an Atlas Suntest CPS+ solar simulator with a daylight optical filter with
293 integrated irradiance of 40 W m⁻² between 300–400 nm; the chamber temperature was
294 fan-cooled to below 40°C (the lowest-possible temperature setting). The vertical walls of the
295 quartz cells and bottom of the chamber were covered with black cardboard. A dark control
296 sample was placed in the chamber in a glass bottle wrapped in aluminum foil. At regular time
297 intervals, one or two of the 14 replicates were sacrificed to measure DOC and CDOM to give
298 a time series for each experiment. The long total duration of our experiments was designed
299 for our specific goal of quantifying what proportion of an initial input of tDOC is
300 photo-remineralized cumulatively over its residence time of up to 2 years in the shelf sea (see
301 Section 2.5). We therefore needed the AQY that corresponds to a similar proportion of tDOC
302 loss to what the model ultimately predicts (which is around 20%, Section 3.3), but not the
303 initial AQY determined from very short exposure times (which would be needed to predict
304 instantaneous daily rates of photochemical CO₂ production, which is not our objective).
305 Because each experiment yielded a time series of DOC and CDOM loss we could also test

306 whether the AQY changed systematically over time, which was not the case.

307

308 The irradiance spectrum of the solar simulator was measured with an Ocean Insights FLAME

309 radiometer from 177 nm to 872 nm at 1 nm resolution. We conducted nitrite actinometry

310 following Jankowski et al. (1999) using the same experimental conditions as for our tDOC

311 samples, and found <6% difference between measured and predicted salicylic acid production

312 (Table S1). This showed that the irradiance measured by the radiometer and used for our

313 AQY determination provided an accurate estimate of the irradiance received by our tDOC

314 samples.

315

316 **2.3 Sample analysis**

317 CDOM absorbance was measured from 230 – 900 nm at room temperature on a Thermo

318 Evolution300 dual-beam spectrophotometer against ultrapure deionized water as a reference

319 using quartz cuvettes with pathlengths of 2, 10 or 100 mm, depending on sample absorbance.

320 The spectra were baseline-corrected, smoothed, and converted to Napierian absorption

321 coefficients using the R package hyperSpec (Beleites & Sergio, 2012). We report the

322 absorption coefficient at 350 nm (a_{350}) as a measure of the CDOM concentration. The

323 spectral slope between 275–295 nm ($S_{275-295}$) and the specific ultraviolet absorption at 254

324 nm ($SUVA_{254}$) were used as proxies for DOC apparent molecular weight (Helms et al., 2008)

325 and aromaticity (Weishaar et al., 2003), respectively.

326

327 DOC samples (30 ml) were acidified with 100 μl 50% H_2SO_4 and analyzed on a Shimadzu
328 TOC-L system with a high-salt combustion kit as previously described in Zhou et al. (2021).
329 The analytical accuracy was monitored using deep-sea water certified reference material
330 (CRM) (42–45 $\mu\text{mol L}^{-1}$ DOC, University of Miami, USA; long-term mean and standard
331 deviation were $48.0 \pm 3.9 \mu\text{mol L}^{-1}$).

332

333 **2.4 Apparent quantum yield calculations**

334 The apparent quantum yield (AQY) can be reported either as a broadband AQY or a
335 spectrally resolved AQY. The broadband AQY is a single value representing the quantity of
336 lost reactant divided by the number of absorbed photons across a specific wavelength range
337 (between 290 and 700 nm in this study), so it shows the “average” photochemical efficiency
338 across this wavelength range. However, the photochemical efficiency varies spectrally. Hence,
339 the spectrally resolved AQY is also frequently reported (Aarnos et al., 2018; Vähätalo et al.,
340 2000, 2003; Zepp, 2007). We calculated both the broadband and spectrally resolved AQY for
341 tDOC and CDOM as summarized below (full details in the Supporting Information).

342

343 The spectrally resolved AQY for tDOC photo-remineralization, $\phi_{DOC}(\lambda)$, was assumed to
344 decrease exponentially with increasing wavelength λ (Gao & Zepp, 1998; Koehler et al.,
345 2022; Vähätalo et al., 2000):

$$346 \quad \phi_{DOC}(\lambda) = c e^{-d\lambda} \quad (1)$$

347 where c ($\text{mol C (mol photons)}^{-1} \text{ nm}^{-1}$) and d (nm^{-1}) are positive constants. Because the

348 quantity of photo-remineralized DOC is the product of AQY and the number of absorbed
349 photons $\Xi(\lambda)$:

$$350 \quad \Delta DOC = \int_{300nm}^{700nm} \phi_{DOC}(\lambda) \Xi(\lambda) d\lambda \quad (2),$$

351 the constants c and d of $\phi_{DOC}(\lambda)$ can be optimized by iteration until the smallest difference
352 between the left (i.e., the measured DOC loss after irradiation) and the right side (i.e., the
353 predicted DOC loss) of Eqn. 2 is reached. For Exp 1, 2 and 3, the AQY was optimized using
354 data of a single irradiance spectrum and a single value of measured DOC loss following
355 Aarnos et al. (2018) and Aarnos et al. (2012). For Exp 4 where multiple spectral treatments
356 were applied, the AQY was optimized when the smallest sum of squared error between the
357 predicted and the measured DOC loss of all spectral treatments was achieved following
358 Powers et al. (2017). We note that in cases where only a single measurement of DOC loss is
359 available (i.e. Exp 1–3), the shape of the calculated AQY spectrum is sensitive to the choice
360 of starting values for constant c . We selected a starting value of 1.0 following Aarnos et al.
361 (2012, 2018), but we also performed a sensitivity analysis in which we repeated our AQY and
362 model calculations using starting values for c of 0.01 and of 100.

363

364 To also model the photobleaching of CDOM, we extended the concept of AQY to the light
365 dose-dependent decrease in CDOM absorption. We refer to this as $\phi_{CDOM}(\lambda)$, which is the
366 spectrally resolved AQY for the decrease in the volume-integrated CDOM absorption
367 coefficient, with units of $L m^{-1} (mol photons)^{-1} nm^{-1}$. We assumed that $\phi_{CDOM}(\lambda)$ resembles
368 $\phi_{DOC}(\lambda)$, decreasing exponentially with increasing wavelength λ :

369
$$\phi_{CDOM}(\lambda) = c' e^{-d'\lambda} \quad (3)$$

370 where c' ($L m^{-1} nm^{-1}$) and d' (nm^{-1}) are positive constants. Similar to DOC, the quantity of
371 lost CDOM is the product of AQY and number of absorbed photons $\Xi(\lambda)$:

372
$$\Delta CDOM = \int_{300nm}^{700nm} \phi_{CDOM}(\lambda) \Xi(\lambda) d\lambda \quad (4),$$

373 so the constants c' and d' of $\phi_{CDOM}(\lambda)$ were optimized by iteration until the smallest
374 difference between the left and the right side of Eqn. 4 was reached. The quantity of CDOM
375 is measured as the absorption coefficient times the sample volume, we therefore calculated
376 the AQY in terms of the measured decrease in absorption coefficient across the CDOM
377 absorption spectrum at 1-nm resolution from 250–700 nm. For Exp 1 – 3, we used a single
378 irradiance spectrum for the calculation of AQY; for Exp 4, we used the data from multiple
379 spectral treatments for the calculation of AQY. These calculations are essentially the same as
380 for DOC, but were carried out at every wavelength at which CDOM absorption was
381 measured (from a_{250} to a_{700}) and then concatenated, yielding spectrally-resolved AQY across
382 the CDOM absorption spectrum.

383

384 **2.5 Model simulation of tDOC photodegradation**

385 **2.5.1 Model overview**

386 Our model calculates the daily changes in tDOC concentration and CDOM absorption caused
387 by solar radiation for both regions. Our modeling approach was modified from Fichot &
388 Benner (2014) and Fichot & Miller (2010), but using spectrally resolved AQY as in (Koehler
389 et al., 2022) and extended to explicitly quantify the decrease in CDOM absorption due to

390 photobleaching. This allows a more accurate calculation of the number of absorbed photons
391 as the CDOM absorption decreases over time. The modeling approach is summarized in Fig.
392 2 and below, and is explained in detail in the Supporting Information.

393

394 Our model iteratively calculates (i) hourly solar irradiance just below the water surface based
395 on the above-water irradiance and solar zenith angle, (ii) underwater light attenuation, (iii)
396 daily total number of absorbed photons based on the real-time CDOM absorption, light
397 attenuation and water depth, (iv) daily decrease in DOC concentration and CDOM absorption
398 based on the total absorbed photons over 24 hours and the AQY, and (v) the DOC
399 concentration and CDOM absorption at the end of the day.

400

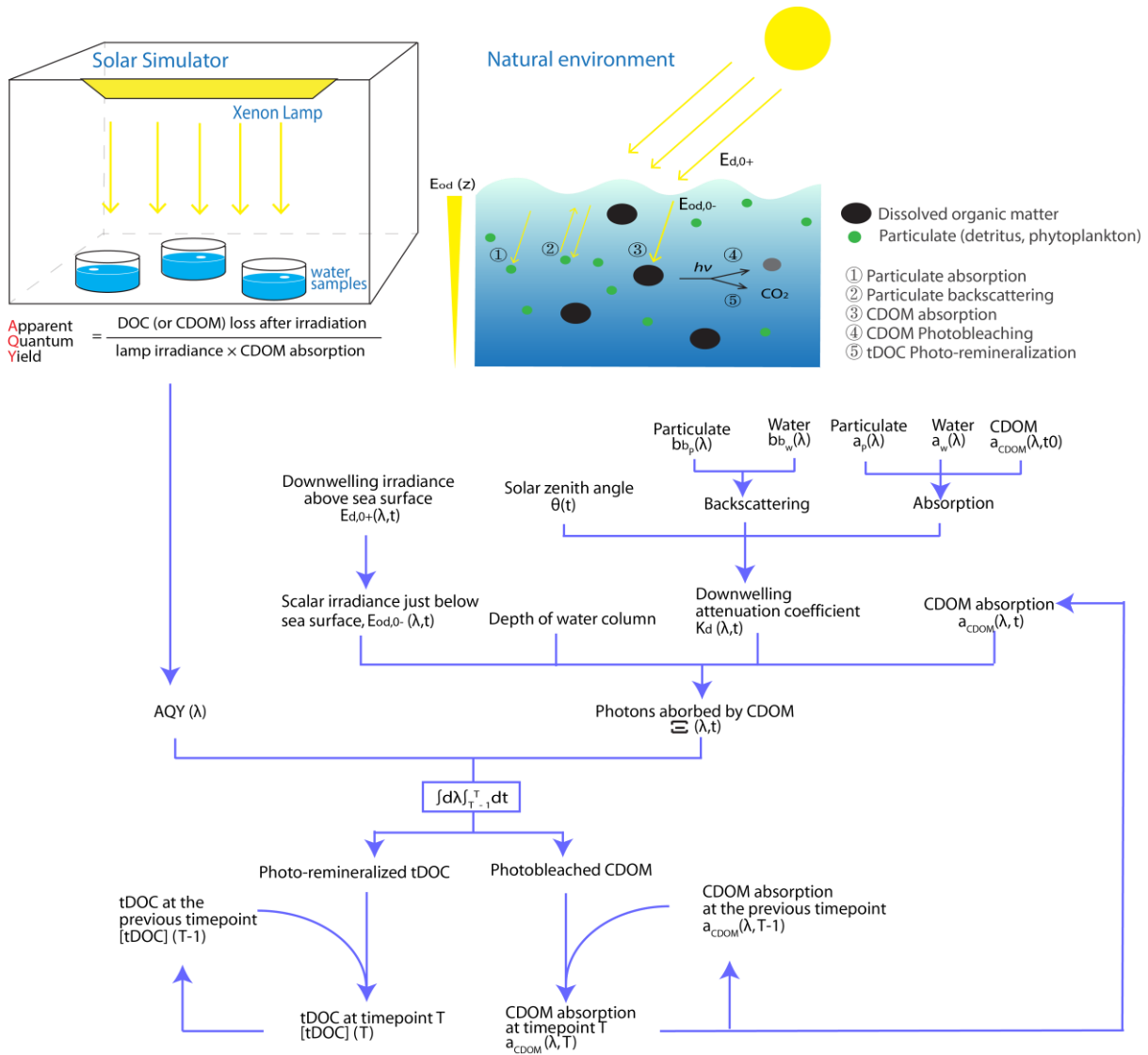
401 The model simulation was performed first using cloud-corrected solar irradiance to estimate
402 the most realistic photodegradation rates and extent, and then using clear-sky solar irradiance
403 to estimate the maximum possible extent of photodegradation. The uncertainty was estimated
404 by a Monte Carlo approach, where all input parameters were perturbed with a 1σ normally
405 distributed error, the model was recalculated 1,000 times, and the standard deviation of the
406 model outputs was then taken as the estimated uncertainty.

407

408 We used the spectrally resolved AQY calculated from our experimental data for the model
409 simulation, but we also ran the simulation using the broadband AQY for comparison. As we
410 discuss in Section 4.2, using the broadband AQY for our simulation appears to lead to a

411 significant overestimate of tDOC photoremineralization because of the spectral change in
 412 underwater irradiance with depth.

413



414

415 Figure 2. Schematic diagram of the model structure for photodegradation simulation. Input

416 variables, parameters, modeling steps, and the model output are shown here. Time-dependent

417 input variables are labeled with a time variable t . Variables are defined in Table S2.

418

419

420
421
422
423
424
425
426
427
428
429
430
431
432
433
434
435
436
437
438
439
440

2.5.2 Model input

We used the mean and standard deviation ($\pm 1SD$) of the four AQY spectra from Exp 1–4 as the model input AQY and its uncertainty, respectively. We obtained the hourly above-water solar irradiance for each month for both modeling regions from the Tropospheric Ultraviolet and Visible Radiation Model (TUV model), US National Center for Atmospheric Research, which were then converted to the irradiance just below the water surface following Fichot and Miller (2010) (Supporting Information). The mean water depth is 19.7 m for the Southern Malacca Strait area and 7.6 m for the Talang region, based on the GEBCO bathymetry (GEBCO Compilation Group, 2020). The areas of the two modeling regions for calculating the mean water depth are shown in Fig. 1b–c. The starting values (i.e., Day 0 values) of tDOC concentration and CDOM absorption were calculated by a two-endmember mixing model using the appropriate riverine endmember data from Wit et al. (2018) and Martin et al. (2018) for the two regions and marine endmember data from Zhou et al. (2021) (Supporting Information). The *in-situ* particulate absorption and backscattering data measured in the Singapore Strait and from the Talang Region were obtained from Martin et al. (2021) and Cherukuru et al. (2021), respectively, and were processed into spectra with 1-nm resolution (Supporting Information). The *in-situ* solar irradiance in each month, initial CDOM spectra (i.e., Day 0) and the particulate absorption and backscattering spectra with their associated

441 uncertainties are shown in Fig. S3 for both modeling regions. In particular, the Talang Region
442 showed pronounced seasonality in solar irradiance – the greater cloud cover during the NE
443 Monsoon (November to January) drives a decrease in the solar irradiance during that period.

444

445

446 **2.5.3 Photochemical decay constant for UniDOM**

447 Anderson et al. (2019) recently proposed the UniDOM framework to model large-scale tDOC
448 biogeochemical processing along the aquatic continuum. The photodegradation component of
449 UniDOM requires a maximum photochemical decay constant, ϕ^{ref} , which defines the
450 photo-remineralization rate of tDOC at the water surface, as the model input. The ϕ^{ref} is a
451 function of the tDOC photochemical properties and thus is region-specific. We calculated the
452 ϕ^{ref} for our two regions based on our modeling results. We first calculated the
453 depth-normalized photochemical decay constant, ϕ , based on the modeled loss of DOC over
454 time and then converted the ϕ to ϕ^{ref} based on equations in Anderson et al. (2019). Details
455 are given in Supporting Information.

456

457

458 **3 Results**

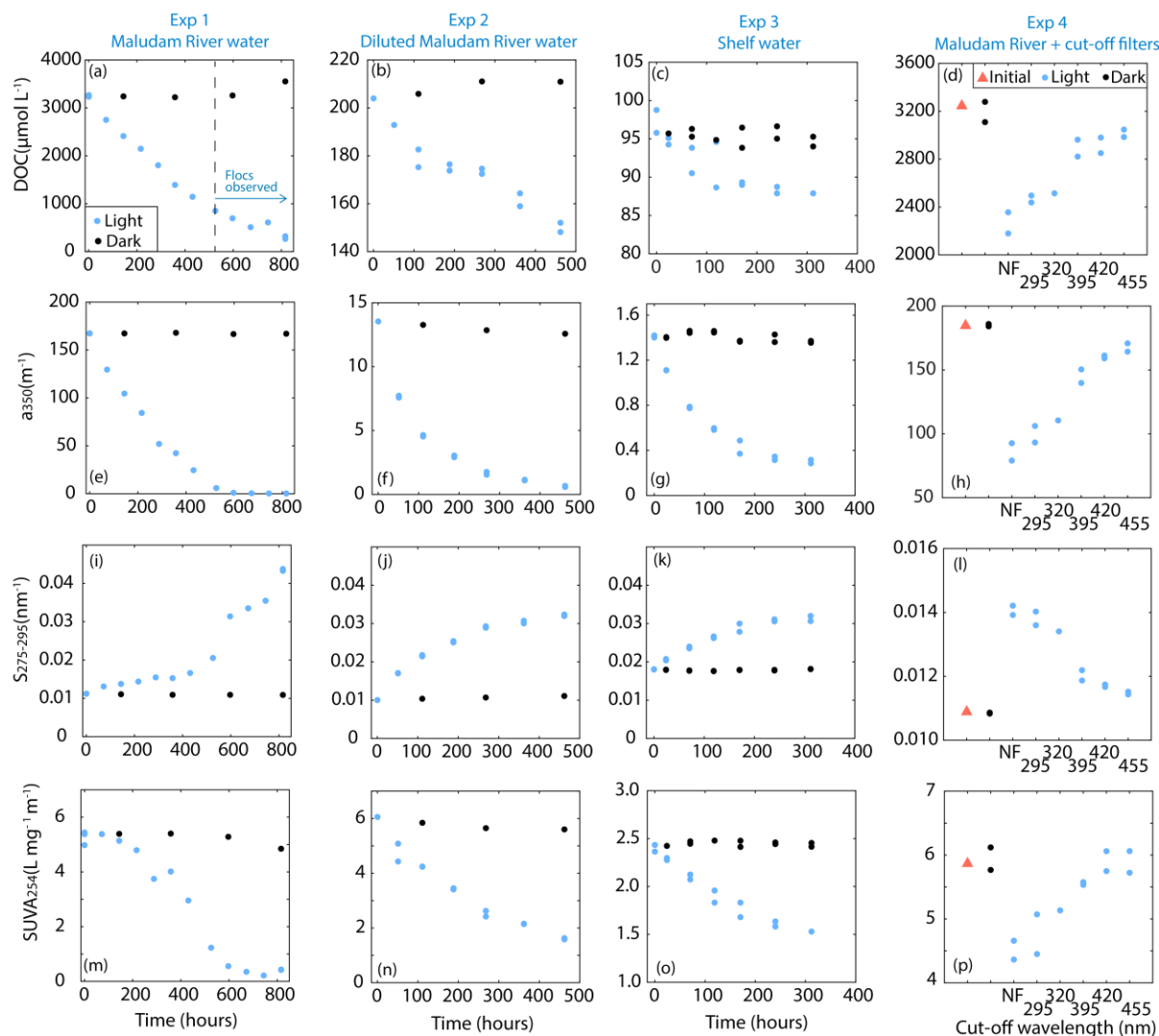
459 **3.1 Photodegradability of peatland-derived tDOC**

460 In all four experiments, we observed loss of DOC and CDOM (as absorption at 350nm, a_{350})
461 upon irradiation, but to different extents (Fig. 3). In Exp 1, flocs were observed at 525 h,

462 suggesting that some DOC was photo-flocculated (Chen et al., 2014; Helms, Mao, et al.,
 463 2013) rather than photo-remineralized; we therefore only used the data up to 416 h. The
 464 Maludam River water samples showed a greater loss of DOC (26–74% loss) compared to the
 465 shelf water sample (9% loss) despite similar duration of irradiation, but they both showed a
 466 near-complete removal of CDOM (Fig. 3 & Table S3). In Exp 4, greater loss of DOC and
 467 CDOM was observed in the spectral treatments with lower cut-off wavelengths.

468

469



470

471 Figure 3. Changes in DOC concentration and CDOM absorption over time (Exp 1,2, and 3)

472 and upon irradiation by different wavelength ranges (Exp 4). In Exp 4, the irradiance below
473 the respective cut-off wavelengths was blocked. *NF*: no optical cut-off filter was used.

474

475 In all experiments, the CDOM spectral slope between 275 nm and 295 nm ($S_{275-295}$) increased
476 while the DOC-specific absorbance at 254 nm ($SUVA_{254}$) decreased (Fig. 3 & Table S3),
477 indicating that compounds with high apparent molecular weight and aromatic moieties were
478 preferentially removed upon irradiation (Helms et al., 2008; Weishaar et al., 2003). In Exp 4,
479 the extent of these changes was greater in treatments exposed to lower wavelengths.

480

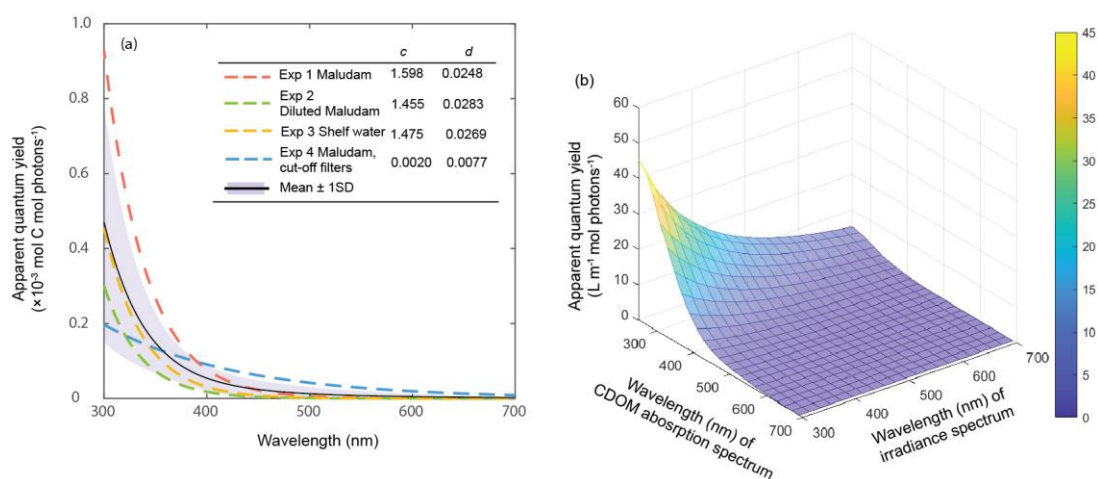
481 **3.2 Apparent quantum yield**

482 The broadband AQY was 42–95 $\mu\text{mol C (mol photons)}^{-1}$ for the Maludam River (Exp 1, 2,
483 and 4) and 85 $\mu\text{mol C (mol photons)}^{-1}$ for the shelf seawater tDOC from the Singapore Strait
484 (Exp. 4), which had experienced prior degradation. The AQY did not show a decreasing trend
485 over the course of the experiments (Table S4). Fig. 4a shows the individual AQY spectra for
486 DOC photo-remineralization that we calculated from Exp 1–4, and the mean spectrum. Some
487 previous studies report the AQY at 330 nm irradiance, $\phi_{DOC}(330nm)$, for comparison of the
488 photochemical efficiency between samples. From our data, the $\phi_{DOC}(330nm)$ was 129 –
489 440 $\mu\text{mol C (mol photons)}^{-1}$ for peatland tDOC from the Maludam River, and 200 $\mu\text{mol C}$
490 $(\text{mol photons})^{-1}$ for the tDOC in the shelf water from the Singapore Strait. To verify that the
491 optimization procedure for calculating spectrally resolved AQY was successful, we used the
492 calculated spectrally resolved AQY with the irradiance spectrum of the solar simulator to

493 predict DOC loss, which well reproduced the DOC loss measured in our all four experiments
 494 (Fig. S4).

495
 496 The corresponding AQY spectra for CDOM photobleaching ($\phi_{CDOM}(\lambda)$) are shown in Fig. S2,
 497 and the mean spectrum is shown in Fig. 4b. At any given irradiance wavelength, the AQY
 498 was higher at shorter wavelengths of the CDOM absorption spectrum. In other words, one
 499 mole of photons at a given irradiance wavelength causes a larger decrease in CDOM
 500 absorption at a shorter absorption wavelength (for instance, a_{300}) compared to at a longer
 501 absorption wavelength (for instance, a_{350}). At any given CDOM absorption wavelength, the
 502 AQY decreases exponentially with increasing irradiance wavelength.

503
 504
 505



506
 507 Figure 4. Spectrally resolved apparent quantum yield for (a) tDOC photo-remineralization
 508 and (b) CDOM photobleaching (i.e. the AQY for reducing the volume-integrated absorption
 509 coefficient). In (a), the individual data from Exp 1–4 are shown together with the mean

510 spectrum and its standard deviation. In (b), only the mean spectrum is shown for clarity, but
511 the standard deviation of the CDOM photobleaching AQY is included in Supplementary Data
512 Set 1.

513

514

515

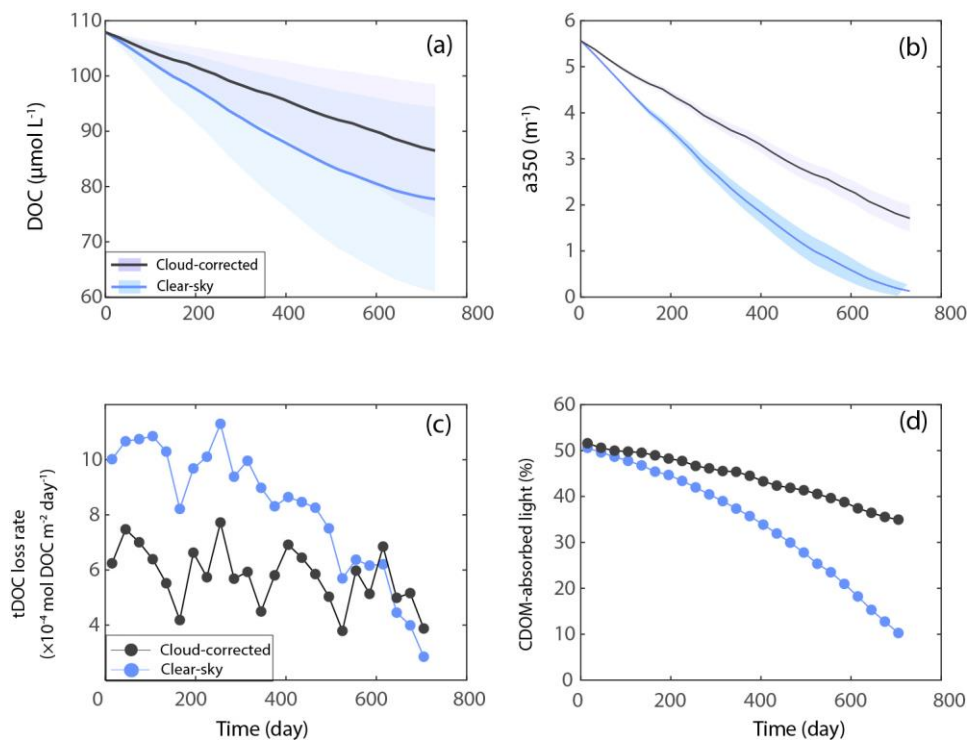
516 **3.4 Photodegradation in the southern Malacca Strait**

517 In the cloud-corrected simulation for the southern Malacca Strait, our model predicted that
518 photoremineralization over 2 years reduced the initial tDOC by $20 \pm 11\%$ from $108 \mu\text{mol L}^{-1}$
519 to $86 \pm 12 \mu\text{mol L}^{-1}$, while the initial CDOM a_{350} was reduced by $69 \pm 5\%$ from 5.6 m^{-1} to 1.7
520 $\pm 0.3 \text{ m}^{-1}$ (Fig. 5a–b, Table 2). Under clear-sky conditions, $28 \pm 16\%$ of tDOC was
521 photo-remineralized and $98 \pm 4\%$ of CDOM was photobleached, with a decrease in tDOC
522 concentration from initially $108 \mu\text{mol L}^{-1}$ to $78 \pm 17 \mu\text{mol L}^{-1}$ and a decrease in a_{350} from 5.6
523 m^{-1} to $0.13 \pm 0.2 \text{ m}^{-1}$ (Fig. 5a–b). Our clear-sky simulation represents a maximum possible
524 extent of tDOC photodegradation.

525

526 The areal rate of tDOC photo-remineralization (pr_{DOC}) showed seasonal variation according
527 to the seasonality in solar irradiance (Fig. 5c, Fig. S3c). Our results show that 51% of solar
528 irradiance (integrated over 300–700 nm) was absorbed by CDOM on Day 1, but this
529 percentage dropped to 34% (cloud-corrected conditions) and 8% (clear-sky conditions) by the
530 end of the 2-year simulation period (Fig. 5d).

531



533

534 Figure 5. Simulated photodegradation for the southern Malacca Strait. (a) Changes in DOC

535 concentration and (b) CDOM absorption (a_{350}) due to solar radiation under cloud-corrected

536 and clear-sky conditions over our 2-year simulation. The shading represents the model

537 uncertainty as estimated by Monte Carlo simulation. (c) Temporal changes in the

538 photo-remineralization rate. (d) Decrease in the percentage of irradiance (integrated over

539 300–700 nm) absorbed by CDOM over time due to CDOM photobleaching.

540

541 Using the results of Year 1 under the cloud-corrected conditions, we calculated the monthly

542 depth-normalized photochemical decay constant, ϕ , which was 0.0002–0.0003 day⁻¹. The543 maximum photochemical decay constant, or the decay constant at the water surface, ϕ^{ref} ,544 was 0.008–0.017 day⁻¹ with a mean of 0.012 day⁻¹ for the southern Malacca Strait. This value

545 could be used to parameterize the UniDOM framework when modeling tDOC turnover for

546 this region.

547

548 To provide a comparison, we also ran a simulation in which we used the broadband AQY
549 instead of the spectrally resolved AQY. The simulation with broadband AQY predicted
550 almost twice as much photodegradation as the simulation with spectrally resolved AQY, with
551 photochemical tDOC loss of 42% (cloud-corrected) and 58% (clear-sky) over two years
552 (Table S5), but we consider this to be an overestimate (see Section 4.2).

553

554 **3.5 The Talang Region**

555 We modeled tDOC photodegradation for four 3-month periods (i.e., February to April, May
556 to July, August to October, and November to January) for the Talang Region, which are the
557 periods showing greatest seasonal differences in solar irradiance (Fig. 6, Table 2). Our model
558 predicted that after 3 months under cloud-corrected conditions, DOC concentration decreased
559 from initially 181 $\mu\text{mol L}^{-1}$ to 173–176 $\mu\text{mol L}^{-1}$, or by 3–4%; the CDOM a_{350} decreased
560 from 10.3 m^{-1} to between 8.7–9.3 m^{-1} , or by 10–15%. Photobleaching of CDOM exhibited
561 pronounced seasonal variation: the early Southwest Monsoon (May to July, when solar
562 irradiance is highest) showed the greatest removal of CDOM (15% loss) while the Northeast
563 Monsoon (November to January) showed the smallest removal (10% loss). Under clear-sky
564 conditions, DOC concentration decreased from initially 181 $\mu\text{mol L}^{-1}$ to 167 $\mu\text{mol L}^{-1}$, or by
565 8%, and the a_{350} of CDOM decreased from 10.3 m^{-1} to 7.3–7.5 m^{-1} , or by 28%, after 3 months.
566 The uncertainty in the final DOC concentration and a_{350} as estimated from our Monte Carlo

567 approach was $\pm 2\text{--}4 \mu\text{mol L}^{-1}$ and $\pm 0.1 \text{ m}^{-1}$, respectively.

568

569 The areal rate of DOC photo-remineralization was $3\text{--}7.6 \times 10^{-4} \text{ mol m}^{-2} \text{ day}^{-1}$ under
570 cloud-corrected conditions and $10\text{--}12 \times 10^{-4} \text{ mol m}^{-2} \text{ day}^{-1}$ under clear-sky conditions
571 (Fig. 6i–l).. Seasonal variation in photoremineralization rate was greater in the
572 cloud-corrected simulation, and the rate was lowest during the NE Monsoon and highest
573 during the early SW Monsoon. The depth-normalized photochemical decay constant, \emptyset , was
574 $0.0003\text{--}0.0005 \text{ day}^{-1}$, which returned a photochemical decay constant at the water surface,
575 \emptyset^{ref} , of $0.007\text{--}0.018 \text{ day}^{-1}$ with a mean of 0.013 day^{-1} .

576

577

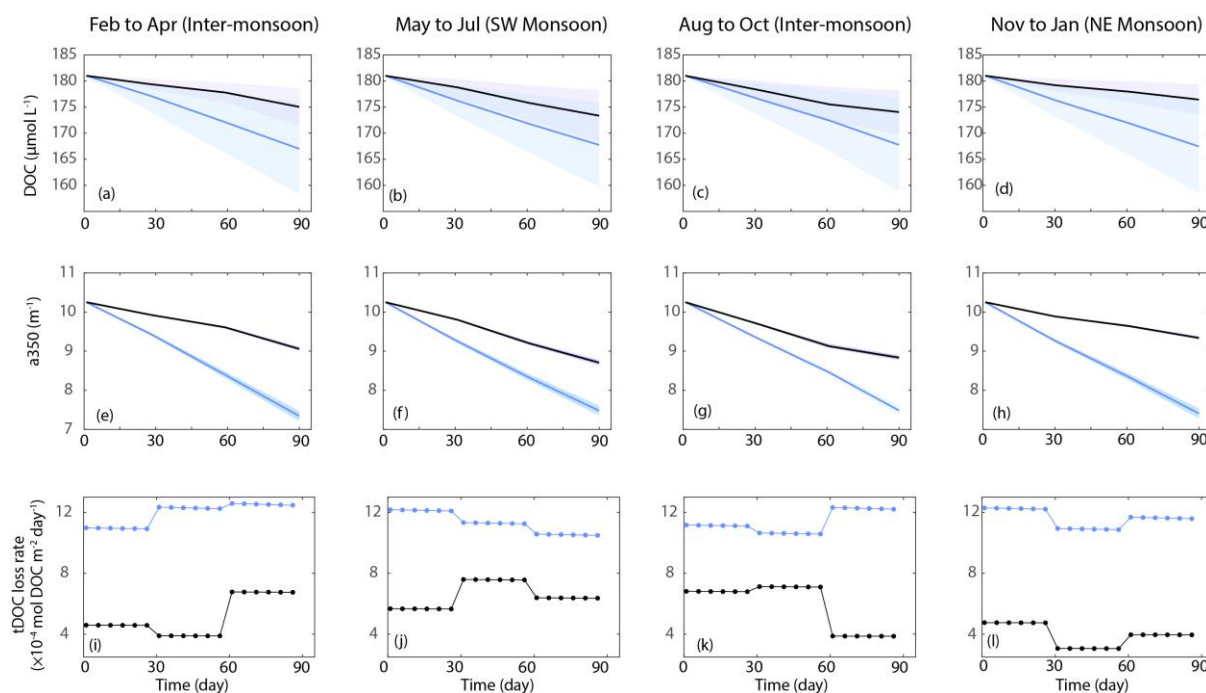
578

579

580

581

582



583

584 Figure 6. Simulated photodegradation for the Talang Region. (a)–(d) Changes in DOC
 585 concentrations and (e)–(h) Changes in the CDOM absorption (a_{350}) under cloud-corrected
 586 and clear-sky conditions for three months in different periods of the year. The grey shading
 587 represents the uncertainties as estimated from the Monte Carlo simulation. (i)–(l) Seasonal
 588 variation in the modeled *in-situ* photo-rem mineralization rates.

589

590 Table 2. Summary of simulated photodegradation under the cloud-corrected conditions. For
 591 the Talang Region, the range in results obtained for the four different time periods is given.

		Initial	Final	%loss
Southern	DOC ($\mu\text{mol L}^{-1}$)	108	86 ± 10	$20 \pm 9\%$
Malacca Strait	CDOM a_{350}	5.6	1.7 ± 0.2	$69 \pm 4\%$
(730 days)	(m^{-1})			

Talang Region	DOC ($\mu\text{mol L}^{-1}$)	181	173–176	3–4%
(90 days)	CDOM a_{350} (m^{-1})	10.3	8.7–9.3	10–15%

592

593

594 4 Discussion

595 4.1 Photodegradability of Southeast Asian peat-tDOC

596 Our experimental results indicate that a high proportion of tDOC from Southeast Asian
597 peatlands is photo-labile, consistent with previous work on tDOC from the
598 peatland-influenced Congo River (Spencer et al., 2009; Stubbins et al., 2010). The shelf water
599 tDOC collected from the Singapore Strait contained a smaller photo-labile fraction (<8% loss
600 OF tDOC), which was expected because the more photo-labile fractions of tDOC had most
601 likely already been remineralized before reaching the Singapore Strait (Zhou et al., 2021).

602

603 We use the photo-remineralization efficiency $\phi_{DOC}(330nm)$ to compare our data to
604 previous literature. Our AQY for Southeast Asian peatland tDOC is comparable to that in
605 large rivers and estuaries globally, but much lower compared to boreal inland waters and
606 oceanic DOC (Table 3). Our AQY is similar to that of Congo River tDOC, which is also
607 partly derived from peatlands (Aarnos et al., 2018), suggesting that tropical peatland tDOC,
608 despite its high photo-lability due to the high aromatic content, is probably not amongst the
609 most efficient organic carbon pools worldwide in the photo-production of CO_2 .

610

611 Table 3. Comparison of apparent quantum yield at 330 nm irradiance for tDOC
 612 photo-remineralization from this study to values in previous literature.

Study site(s)	$\phi_{DOC}(330nm)$ $\mu\text{mol C mol photons}^{-1}$	Reference
Maludam River	440 (Exp 1, Maludam River)	This study
(Peatland-derived DOC)	129 (Exp 2, diluted Maludam river water)	
	156 (Exp 4, Maludam River)	
Singapore Strait (Southwest Monsoon during seasonal tDOC input)	203	This study
World's major rivers	172–335	Aarnos et al. (2018)
Congo River	286	Aarnos et al. (2018)
(Peatland-derived tDOC)		
Tropical and temperate lakes	250–750	Koehler et al. (2016)
Delaware Estuary	249	White et al. (2010)
Inshore waters	514	Powers & Miller (2015)
Boreal Lakes	300–2000	Koehler et al. (2014, 2016)
Humic Lake	708	Vähätalo et al. (2000)
Coastal Waters	989	Johannessen & Miller (2001)
Open Ocean	2900	Johannessen & Miller (2001)

613

614

615 **4.2 Limitations of the AQY determination**

616 Our approach for calculating spectrally resolved AQY from our experiments has limitations,
617 but as we show below, these limitations do not affect our modeling results and conclusion.

618 The limitations are: 1) the method assumes that AQY decreases exponentially with increasing
619 wavelength, and 2) the optimized AQY spectrum does not have a unique solution but varies
620 depending on the starting values chosen for the optimization.

621

622 The assumption that AQY spectra have an exponential shape has been validated by
623 measurements of AQY for pure organic molecules at multiple discrete wavelengths (Gao &
624 Zepp, 1998; C. A. Moore et al., 1993; Moran & Zepp, 1997) and is thus reasonable to be
625 extended to the natural organic matter pool (Aarnos et al., 2012; Koehler et al., 2016;
626 Vähätalo et al., 2000). Experiments using wavelength cut-off filters or monochromatic light
627 sources also confirm that AQYs for natural DOC show exponential spectra (Ward et al.,
628 2021).

629

630 To address the impact of the optimization parameters, we ran a sensitivity analysis in which
631 we changed the starting value of coefficient c in the AQY calculation from 1.0 (Aarnos et al.,
632 2012, 2018) to first 0.01 and then to 100, and then repeated our model simulation with each
633 of the two resulting AQY spectra. We found that changing the starting values for the

634 coefficients over this range of 4 orders of magnitude did indeed change the shape of the AQY
635 spectra (Fig. S5), but this only changed our final estimate of how much tDOC is
636 photo-remineralized by < 6% (Table S6). While this rather limited sensitivity of our model
637 result to the shape of the AQY spectrum may seem surprising, it is a consequence of the fact
638 that we are simulating photodegradation in a well-mixed water column that is optically thick,
639 i.e. the incoming solar radiation is nearly all absorbed within the water layer we are
640 simulating. Therefore, with a steeper AQY spectrum our model predicts more DOC loss close
641 to the surface where there is more UV light but less DOC loss deeper down; while with a
642 flatter AQY spectrum, there is less DOC loss at shallow depths but in turn more DOC loss in
643 deeper waters caused by visible wavelengths. It should be noted that if photodegradation is
644 being modeled for a water layer that is optically thinner (e.g. for a surface mixed layer that is
645 shallower than the euphotic zone depth) the uncertainty in AQY spectral shape associated
646 with this optimization calculation could be much more significant.

647

648 Despite these limitations, it is important to use a spectral AQY rather than applying a
649 broadband AQY when simulating photodegradation in an optically thick water layer because
650 the irradiance spectrum shifts strongly to longer wavelengths (with lower AQY) within just
651 1–2 m below the surface in these optically complex waters (Martin et al., 2021). However,
652 the broadband AQY in our experiments was necessarily determined by exposing optically
653 thin tDOC solutions to full-spectrum irradiance. This broadband AQY is only appropriate for
654 calculating photodegradation in a water layer that is similarly optically thin as in the

655 experimental conditions, such that the depth-integrated spectrum of photons absorbed by
656 CDOM has a similar shape between the model and the experiments – but if it is applied in
657 deeper waters where the irradiance spectrum (and the depth-integrated spectrum of photons
658 absorbed by CDOM) is shifted to longer wavelengths, it overestimates the photodegradation.
659 This is illustrated by the fact that when we used the broadband AQY from our experiments to
660 run our model, it predicted around twice as much tDOC loss compared to the simulation with
661 spectrally resolved AQY (see Table S5 and Section 3.3). This clearly represents an
662 overestimate of the tDOC photo-remineralization, because the depth-integrated spectrum of
663 photons absorbed by CDOM for our modeled water column is shifted considerably towards
664 blue and green wavelengths (that have lower AQY than UV light) relative to that in our
665 experiments that are used to calculate the AQY (Fig. S6).

666

667 Finally, our AQY spectra were derived from a limited number of samples. Although the
668 Maludam River and Singapore Strait samples are likely fairly well representative of the
669 peatland tDOC in Southeast Asia (Section 2.1.1), and our uncertainty analysis shows that the
670 variation between these AQY spectra does not result in substantial model uncertainties
671 (Sections 3.4 and 3.5), more AQY determinations should be made for this region.

672

673 **4.3 Contribution of photodegradation to total tDOC remineralization**

674 Previous work showed that at least 60–70% of tDOC exported from Sumatran peatlands is
675 remineralized in the coastal waters of the Sunda Shelf Sea (Wit et al., 2018; Zhou et al.,

2021). Given also that the direct microbial remineralization appears to be slow and therefore a minor sink for tDOC over the residence time of tDOC on the shelf, we previously hypothesized that photodegradation accounts for a significant part of this remineralization (Nichols & Martin 2021; Zhou et al. 2021). However, our cloud-corrected model simulation shows that solar radiation can only directly remineralize $20 \pm 11\%$ of the initial tDOC input during the 2-year residence time on the shelf. This would account for 31% of the total tDOC remineralization estimated by Zhou et al. (2021). While direct photo-remineralization thus appears to make an important contribution, it is clearly not the only important process. We therefore infer that photochemically enhanced microbial remineralization (Cory et al., 2007; Cory & Kling, 2018; Judd et al., 2007; Moran & Zepp, 1997) might be important in Southeast Asia. Such interactive remineralization was estimated to account for 32% of the total tDOC remineralization on the Louisiana Shelf (Fichot & Benner, 2014). Our photodegradation experiments suggested a preferential removal of tDOC compounds with high apparent molecular weight upon solar radiation, which would be consistent with increased bio-lability of the partially photodegraded tDOC (Miller & Moran, 1997; Moran et al., 2000; Moran & Zepp, 1997). However, photodegradation can also compete with biodegradation for the same tDOC fractions (Ward et al., 2017). Further research is therefore required to quantify the contribution of photo-enhanced bio-remineralization to the tDOC processing.

694

In the Talang Region, solar irradiation can only directly remineralize 3–4% of the initial tDOC input over 3 months (given the more open coastline in this region, tDOC will most

697 likely be removed by mixing and advection over time scales longer than 3 months). This low
698 photodegradation rate from our modeling is consistent with the conservative mixing behavior
699 and the limited degradation of tDOC across peatland-draining estuaries in Southeast Asia
700 reported previously (Alkhatib et al., 2007; Baum et al., 2007; Martin et al., 2018). However,
701 solar radiation removes 7–12% of the riverine CDOM in this region over three months.
702 Photobleaching can therefore remove a significant portion of CDOM over seasonal time
703 scales, as hypothesized by Kaushal et al. (2021). The seasonal variation in the extent of
704 photobleaching observed from our modeling (i.e., greater loss of CDOM during Southwest
705 Monsoon than Northeast Monsoon) is driven by the seasonal changes in irradiance in this
706 region, chiefly due to the seasonality of cloud cover (Fig. S3d), and might contribute to the
707 large seasonal decrease in CDOM after the NE Monsoon inferred from coral skeleton
708 luminescence (Kaushal et al., 2021).

709
710 Our modeling results also indicate that photodegradation might play a larger role in tDOC
711 processing in the Sunda Shelf Sea compared to regions at higher latitudes. On the Louisiana
712 Shelf, direct photo-remineralization appears to remove only 4% of the riverine tDOC input
713 within the surface mixed layer, accounting for only 8% of the total tDOC remineralization
714 (Fichot & Benner, 2014). On a global scale, Aarnos et al. (2018) estimated that if all riverine
715 CDOM is photobleached, 18% of the riverine tDOC flux is photo-remineralized in the ocean.
716 That estimate is close to our results that 20% of the Sumatran peatland tDOC is
717 photo-remineralized on the shelf, showing the quantitatively important role of

718 photo-remineralization in the tropical shelf sea in Southeast Asia. The greater relative
719 contribution from photo-remineralization here is likely due to the relatively long water
720 residence time in the shelf sea (2 years) (Mayer et al., 2015), the higher solar irradiance in the
721 tropics (Apell & McNeill, 2019) and the low bio-lability of the tDOC (Nichols & Martin,
722 2021).

723

724 **4.4 Decay constants for simplified photodegradation modeling**

725 Our spectrally resolved optical modeling can potentially inform the parameterization of
726 simplified model representations of terrestrial carbon cycling such as UniDOM (Anderson et
727 al., 2019), which was proposed as a modeling framework that is sufficiently simplified to be
728 included in large-scale Earth System Models. Specifically, we can use our results to estimate
729 the decay rate constants ϕ and ϕ^{ref} that are key input variables in UniDOM, so that tDOC
730 photo-remineralization can be modelled realistically in Southeast Asia. The ϕ^{ref} derived
731 from our modeling results ($0.008 - 0.017 \text{ day}^{-1}$) is much smaller than the default global value
732 used in UniDOM (0.13 day^{-1}), which was based on the observed decay rate in laboratory
733 photodegradation experiments. UniDOM applies a large age-dependent term to rapidly
734 decrease the very high initial maximum decay rate over time based on global observations of
735 the decreasing DOC turnover rate with the increasing DOC age (Catalán et al., 2016; Evans
736 et al., 2017) and to yield an overall realistic extent of photo-remineralization. In contrast, our
737 photodegradation experiments did not show a systematic decrease in the photochemical
738 efficiency (i.e., AQY) of tDOC over time (Table S4). This suggests that a large age-dependent

739 correction might not be the most appropriate way to parameterize photochemical tDOC,
740 provided that realistic *in-situ* values of ϕ^{ref} can be estimated.

741

742 Our data also show that high photo-lability as measured in experimental incubations does not
743 necessarily lead to a high *in-situ* photodegradation rate because the latter is also dependent on
744 the *in-situ* light dose, the depth-integrated total amount of tDOC and CDOM, and other
745 inherent optical properties (IOPs) in the water. For example, our Exp 1 showed that a 22-day
746 simulated solar radiation can cause a loss of 74% of the initial tDOC. However, the *in-situ*
747 solar irradiance ($35 \text{ mol photons m}^{-2} \text{ day}^{-1}$, integrated over 300–700nm) is only one-fifth of
748 the irradiance in the solar simulator ($181 \text{ mol photons m}^{-2} \text{ day}^{-1}$), while the tDOC amount to
749 be remineralized in the entire water column of the shelf sea (2.12 mol m^{-2}) is 35 times of that
750 in each cuvette used in the photodegradation experiments (0.06 mol m^{-2}). The extent of tDOC
751 photo-remineralization on the shelf is also constrained by its residence time. Regarding the
752 IOPs in the water, the particulate absorption and backscattering are lower than the CDOM
753 absorption for both modeled regions, partly because of the low chlorophyll-*a* concentrations
754 in the study region (Martin et al., 2018, 2022). The light attenuation coefficient, K_d , is
755 therefore dominated by CDOM absorption (Martin et al., 2021), especially at ultraviolet
756 wavelengths. Given the multiple controlling factors of *in-situ* photodegradation rates, we
757 recommend performing spectrally resolved optical modeling to obtain more accurate
758 estimates of the photochemical decay rate constant that can then be used by simplified
759 models across much larger scales.

760

761

762 **5 Conclusions**

763 Although the tDOC from Southeast Asian peatlands contains a large photolabile fraction, the
764 apparent quantum yields for tDOC remineralization are fairly low, which is consistent with
765 apparent quantum yields for tDOC reported from major rivers globally. Based on model
766 simulations, we found that (1) natural solar radiation can directly remineralize $20 \pm 11\%$ of
767 the tDOC flux from Sumatran peatlands in the shelf sea, but this process alone is insufficient
768 to account for the high reported extent of tDOC remineralization in this region; (2) seasonal
769 variation in photobleaching of terrestrial CDOM probably contributes to the strong
770 seasonality of coral core luminescence records in the Talang Region of northwestern Borneo
771 (Kaushal et al., 2021); (3) our modeled rates of tDOC photo-remineralization are equivalent
772 to using a photochemical decay constant, ϕ^{ref} , of $0.008 - 0.017 \text{ day}^{-1}$ in the UniDOM model,
773 but an age-dependent correction factor is not necessary. Our study demonstrates that
774 photochemical processing of peatland tDOC is important in Southeast Asia but falls far short
775 of explaining the extent of tDOC remineralization observed in the Sunda Shelf Sea. We
776 hypothesize that interactions between photochemical and microbial remineralization are
777 likely significant in this region and need to be quantified in future research.

778

779 **Acknowledgements**

780 We are grateful to the many students and research staff, especially from Nanyang

781 Technological University, Swinburne University of Science and Technology, and Universiti
782 Malaysia Sarawak, who helped with field and laboratory work. Permission for this research
783 was given by the National Parks Board, Singapore (permit NP/RP17-044-3), and by the
784 Sarawak Forestry Department and Sarawak Biodiversity Centre (permits
785 NPW.907.4.4(Jld.14)-161, WL83/2017, and SBC-RA-0097-MM). Patrick Martin
786 acknowledges funding by the Singapore Ministry of Education under the Academic Research
787 Fund Tier 2 programme (grant MOE-MOET2EP10121-0007) and by the National Research
788 Foundation Singapore, Prime Minister's Office, as part of the Marine Science Research and
789 Development Programme (grant MSRDP-P32). Moritz Müller was funded by MOHE FRGS
790 15 (grant FRGS/1/2015/WAB08/SWIN/02/1) and by the Newton-Ungku Omar Fund (grant
791 GL/F07/NUOF/01/2017). Nagur Cherukuru was funded by CSIRO Oceans and Atmosphere
792 and by the Regional Collaborations Programme (Australian Academy of Sciences).

793

794 **Open Research**

795 Raw experimental data and source codes for data processing and modeling are available
796 through the NTU data repository (<https://doi.org/10.21979/N9/XQSOEN>).

797

798 **Author Contributions**

799 Conceptualization: Y.Z., P.M.;

800 Methodology: Y.Z., P.M.;

801 Software: Y.Z.;

802 Formal analysis: Y.Z.;

803 Resources: P.M., M.M., N.C.;

804 Data curation: Y.Z., M.M., N.C., P.M.;

805 Investigation: Y.Z.;

806 Writing – original draft preparation: Y.Z.;

807 Writing – review and editing: Y.Z., M.M., N.C., P.M.;

808 Supervision: P.M.;

809 Project administration: P.M.;

810 Funding acquisition: P.M., M.M., N.C.

811

812

813 **References**

- 814 Aarnos, H., Ylöstalo, P., & Vähätalo, A. V. (2012). Seasonal phototransformation of dissolved
815 organic matter to ammonium, dissolved inorganic carbon, and labile substrates
816 supporting bacterial biomass across the Baltic Sea. *Journal of Geophysical Research:*
817 *Biogeosciences*, *117*(1), 1–14. <https://doi.org/10.1029/2010JG001633>
- 818 Aarnos, H., Gélinas, Y., Kasurinen, V., Gu, Y., Puupponen, V. M., & Vähätalo, A. V. (2018).
819 Photochemical Mineralization of Terrigenous DOC to Dissolved Inorganic Carbon in
820 Ocean. *Global Biogeochemical Cycles*, *32*(2), 250–266.
821 <https://doi.org/10.1002/2017GB005698>
- 822 Aksnes, D. L., Dupont, N., Staby, A., Fiksen, Ø., Kaartvedt, S., & Aure, J. (2009). Coastal

823 water darkening and implications for mesopelagic regime shifts in Norwegian fjords.
824 *Marine Ecology Progress Series*, 387(Jerlov 1968), 39–49.
825 <https://doi.org/10.3354/meps08120>

826 Alkhatib, M., Jennerjahn, T. C., & Samiaji, J. (2007). Biogeochemistry of the Dumai River
827 estuary, Sumatra, Indonesia, a tropical black-water river. *Limnology and Oceanography*,
828 52(6), 2410–2417. <https://doi.org/10.4319/lo.2007.52.6.2410>

829 Allesson, L., Koehler, B., Thrane, J. E., Andersen, T., & Hessen, D. O. (2021). The role of
830 photomineralization for CO₂ emissions in boreal lakes along a gradient of dissolved
831 organic matter. *Limnology and Oceanography*, 66(1), 158–170.
832 <https://doi.org/10.1002/lno.11594>

833 Anderson, T. R., Rowe, E. C., Polimene, L., Tipping, E., Evans, C. D., Barry, C. D. G., et al.
834 (2019). Unified concepts for understanding and modelling turnover of dissolved organic
835 matter from freshwaters to the ocean: the UniDOM model. *Biogeochemistry*, 146(2),
836 105–123. <https://doi.org/10.1007/s10533-019-00621-1>

837 Apell, J. N., & McNeill, K. (2019). Updated and validated solar irradiance reference spectra
838 for estimating environmental photodegradation rates. *Environmental Science: Processes
839 and Impacts*, 21(3), 427–437. <https://doi.org/10.1039/c8em00478a>

840 Baum, A., Rixen, T., & Samiaji, J. (2007). Relevance of peat draining rivers in central
841 Sumatra for the riverine input of dissolved organic carbon into the ocean. *Estuarine,
842 Coastal and Shelf Science*, 73(3–4), 563–570. <https://doi.org/10.1016/j.ecss.2007.02.012>

843 Beleites, C., & Sergio, V. (2012). hyperSpec: a package to handle hyperspectral data sets in R.

844 *Journal of Statistical Software.*

845 Cai, W.-J. (2011). Estuarine and Coastal Ocean Carbon Paradox: CO₂ Sinks or Sites of
846 Terrestrial Carbon Incineration? *Annual Review of Marine Science*, 3(1), 123–145.
847 <https://doi.org/10.1146/annurev-marine-120709-142723>

848 Catalán, N., Marcé, R., Kothawala, D. N., & Tranvik, L. J. (2016). Organic carbon
849 decomposition rates controlled by water retention time across inland waters. *Nature*
850 *Geoscience*, 9(7), 501–504. <https://doi.org/10.1038/ngeo2720>

851 Chen, H., Abdulla, H. A. N., Sanders, R. L., Myneni, S. C. B., Mopper, K., & Hatcher, P. G.
852 (2014). Production of Black Carbon-like and Aliphatic Molecules from Terrestrial
853 Dissolved Organic Matter in the Presence of Sunlight and Iron. *Environmental Science*
854 *and Technology Letters*, 1(10), 399–404. <https://doi.org/10.1021/ez5002598>

855 Cherukuru, N., Martin, P., Sanwlani, N., Mujahid, A., & Müller, M. (2021). A semi-analytical
856 optical remote sensing model to estimate suspended sediment and dissolved organic
857 carbon in tropical coastal waters influenced by peatland-draining river discharges off
858 sarawak, borneo. *Remote Sensing*, 13(1), 1–31. <https://doi.org/10.3390/rs13010099>

859 Ciais, P., Sabine, C., & Bala, G. (2013). Chapter 6: Carbon and other biogeochemical cycles.
860 *Climate Change 2013: The Physical Science Basis.*

861 Cory, R. M., & Kling, G. W. (2018). Interactions between sunlight and microorganisms
862 influence dissolved organic matter degradation along the aquatic continuum. *Limnology*
863 *and Oceanography Letters*, 3(3), 102–116. <https://doi.org/10.1002/lol2.10060>

864 Cory, R. M., McKnight, D. M., Chin, Y. P., Miller, P., & Jaros, C. L. (2007). Chemical

865 characteristics of fulvic acids from Arctic surface waters: Microbial contributions and
866 photochemical transformations. *Journal of Geophysical Research: Biogeosciences*,
867 *112*(4), 1–14. <https://doi.org/10.1029/2006JG000343>

868 Dittmar, T., Whitehead, K., Minor, E. C., & Koch, B. P. (2007). Tracing terrigenous dissolved
869 organic matter and its photochemical decay in the ocean by using liquid
870 chromatography/mass spectrometry. *Marine Chemistry*, *107*(3), 378–387.
871 <https://doi.org/10.1016/j.marchem.2007.04.006>

872 Evans, C. D., Futter, M. N., Moldan, F., Valinia, S., Frogbrook, Z., & Kothawala, D. N.
873 (2017). Variability in organic carbon reactivity across lake residence time and trophic
874 gradients. *Nature Geoscience*, *10*(11), 832–835. <https://doi.org/10.1038/NGEO3051>

875 Fichot, C. G., & Benner, R. (2014). The fate of terrigenous dissolved organic carbon in a
876 river-influenced ocean margin. *Global Biogeochemical Cycles*, *28*(3), 300–318.
877 <https://doi.org/10.1002/2013GB004670>

878 Fichot, C. G., & Miller, W. L. (2010). An approach to quantify depth-resolved marine
879 photochemical fluxes using remote sensing: Application to carbon monoxide (CO)
880 photoproduction. *Remote Sensing of Environment*, *114*(7), 1363–1377.
881 <https://doi.org/10.1016/j.rse.2010.01.019>

882 Gao, H., & Zepp, R. G. (1998). Factors influencing photoreactions of dissolved organic
883 matter in a coastal river of the southeastern United States. *Environmental Science and*
884 *Technology*, *32*(19), 2940–2946. <https://doi.org/10.1021/es9803660>

885 GEBCO Compilation Group. (2020). GEBCO 2020 Grid.

886 <https://doi.org/10.5285/a29c5465-b138-234d-e053-6c86abc040b9>

887 Giesen, W., Wijedasa, L. S., & Page, S. E. (2018). Unique Southeast Asian peat swamp forest
888 habitats have relatively few distinctive plant species. *Mires and Peat*, 22, 1–13.
889 <https://doi.org/10.19189/MaP.2017.OMB.287>

890 Gu, Y., Lensu, A., Perämäki, S., Ojala, A., & Vähätalo, A. V. (2017). Iron and pH Regulating
891 the Photochemical Mineralization of Dissolved Organic Carbon. *ACS Omega*, 2(5),
892 1905–1914. <https://doi.org/10.1021/acsomega.7b00453>

893 Helms, J. R., Stubbins, A., Ritchie, J. D., Minor, E. C., Kieber, D. J., & Mopper, K. (2008).
894 Absorption spectral slopes and slope ratios as indicators of molecular weight, source,
895 and photobleaching of chromophoric dissolved organic matter. *Limnology and*
896 *Oceanography*, 53(3), 955–969. <https://doi.org/10.4319/lo.2008.53.3.0955>

897 Helms, J. R., Stubbins, A., Perdue, E. M., Green, N. W., Chen, H., & Mopper, K. (2013).
898 Photochemical bleaching of oceanic dissolved organic matter and its effect on
899 absorption spectral slope and fluorescence. *Marine Chemistry*, 155, 81–91.
900 <https://doi.org/10.1016/j.marchem.2013.05.015>

901 Helms, J. R., Mao, J., Schmidt-Rohr, K., Abdulla, H., & Mopper, K. (2013). Photochemical
902 flocculation of terrestrial dissolved organic matter and iron. *Geochimica et*
903 *Cosmochimica Acta*, 121, 398–413. <https://doi.org/10.1016/j.gca.2013.07.025>

904 Jankowski, J. J., Kieber, D. J., & Mopper, K. (1999a). Nitrate and nitrite ultraviolet
905 actinometers. *Photochemistry and Photobiology*, 70(3), 319–328.
906 <https://doi.org/10.1111/j.1751-1097.1999.tb08143.x>

907 Jankowski, J. J., Kieber, D. J., & Mopper, K. (1999b). Nitrate and Nitrite Ultraviolet
908 Actinometers. *Photochemistry and Photobiology*, 70(3), 319–328.
909 <https://doi.org/10.1111/j.1751-1097.1999.tb08143.x>

910 Johannessen, S. C., & Miller, W. L. (2001). Quantum yield for the photochemical production
911 of dissolved inorganic carbon in seawater. *Marine Chemistry*, 76(4), 271–283.
912 [https://doi.org/10.1016/S0304-4203\(01\)00067-6](https://doi.org/10.1016/S0304-4203(01)00067-6)

913 Judd, K. E., Crump, B. C., & Kling, G. W. (2007). Bacterial responses in activity and
914 community composition to photo-oxidation of dissolved organic matter from soil and
915 surface waters. *Aquatic Sciences*, 69(1), 96–107.
916 <https://doi.org/10.1007/s00027-006-0908-4>

917 Kaiser, K., Benner, R., & Amon, R. M. W. (2017). The fate of terrigenous dissolved organic
918 carbon on the Eurasian shelves and export to the North Atlantic. *Journal of Geophysical*
919 *Research: Oceans*, 122(1), 4–22. <https://doi.org/10.1002/2016JC012380>

920 Kaushal, N., Sanwlani, N., Tanzil, J. T. I., Cherukuru, N., Sahar, S., Müller, M., et al. (2021).
921 Coral Skeletal Luminescence Records Changes in Terrestrial Chromophoric Dissolved
922 Organic Matter in Tropical Coastal Waters. *Geophysical Research Letters*, 48(8), 1–12.
923 <https://doi.org/10.1029/2020GL092130>

924 Kitidis, V., Shutler, J. D., Ashton, I., Warren, M., Brown, I., Findlay, H., et al. (2019). Winter
925 weather controls net influx of atmospheric CO₂ on the north-west European shelf.
926 *Scientific Reports*, 9(1), 1–11. <https://doi.org/10.1038/s41598-019-56363-5>

927 Koehler, B., Landelius, T., Weyhenmeyer, G. A., Machida, N., & Tranvik, L. J. (2014).

928 Sunlight-induced carbon dioxide emissions from inland waters. *Global Biogeochemical*
929 *Cycles*, 28(7), 696–711. <https://doi.org/10.1002/2014GB004850>

930 Koehler, B., Broman, E., & Tranvik, L. J. (2016). Apparent quantum yield of photochemical
931 dissolved organic carbon mineralization in lakes. *Limnology and Oceanography*, 61(6),
932 2207–2221. <https://doi.org/10.1002/lno.10366>

933 Koehler, B., Powers, L. C., Cory, R. M., Einarsdóttir, K., Gu, Y., Tranvik, L. J., et al. (2022).
934 Inter-laboratory differences in the apparent quantum yield for the photochemical
935 production of dissolved inorganic carbon in inland waters and implications for
936 photochemical rate modeling. *Limnology and Oceanography: Methods*, 320–337.
937 <https://doi.org/10.1002/lom3.10489>

938 Lee, Z. P., Du, K. P., & Arnone, R. (2005). A model for the diffuse attenuation coefficient of
939 downwelling irradiance. *Journal of Geophysical Research C: Oceans*, 110(2), 1–10.
940 <https://doi.org/10.1029/2004JC002275>

941 Martin, P., Cherukuru, N., Tan, A. S. Y., Sanwlan, N., Mujahid, A., & Müller, M. (2018).
942 Distribution and cycling of terrigenous dissolved organic carbon in peatland-draining
943 rivers and coastal waters of Sarawak, Borneo. *Biogeosciences*, 15(22), 6847–6865.
944 <https://doi.org/10.5194/bg-15-6847-2018>

945 Martin, P., Sanwlan, N., Lee, T., Wong, J., Chang, K., Wong, E., & Liew, S. (2021).
946 Dissolved organic matter from tropical peatlands reduces shelf sea light availability in
947 the Singapore Strait, Southeast Asia. *Marine Ecology Progress Series*.
948 <https://doi.org/10.3354/meps13776>

949 Martin, P., Moynihan, M. A., Chen, S., Woo, O. Y., Zhou, Y., Nichols, R. S., et al. (2022).
950 Monsoon-driven biogeochemical dynamics in an equatorial shelf sea: Time-series
951 observations in the Singapore Strait. *Estuarine, Coastal and Shelf Science*, 270(April),
952 107855. <https://doi.org/10.1016/j.ecss.2022.107855>

953 Massicotte, P., Asmala, E., Stedmon, C., & Markager, S. (2017). Global distribution of
954 dissolved organic matter along the aquatic continuum: Across rivers, lakes and oceans.
955 *Science of The Total Environment*, 609, 180–191.
956 <https://doi.org/10.1016/j.scitotenv.2017.07.076>

957 Mathis, M., Logemann, K., Maerz, J., Lacroix, F., Hagemann, S., Chegini, F., et al. (2022).
958 Seamless Integration of the Coastal Ocean in Global Marine Carbon Cycle Modeling.
959 *Journal of Advances in Modeling Earth Systems*, 14(8), 1–44.
960 <https://doi.org/10.1029/2021MS002789>

961 Mayer, B., Stacke, T., Stottmeister, I., & Pohlmann, T. (2015). Sunda Shelf Seas: flushing
962 rates and residence times. *Ocean Science Discussions*, 12(3), 863–895.
963 <https://doi.org/10.5194/osd-12-863-2015>

964 Mayer, B., Rixen, T., & Pohlmann, T. (2018). The spatial and temporal variability of air-sea
965 CO₂ fluxes and the effect of net coral reef calcification in the Indonesian Seas: A
966 numerical sensitivity study. *Frontiers in Marine Science*, 5(APR), 1–19.
967 <https://doi.org/10.3389/fmars.2018.00116>

968 Miller, W. L., & Moran, M. A. (1997). Interaction of photochemical and microbial processes
969 in the degradation of refractory dissolved organic matter from a coastal marine

970 environment. *Limnology and Oceanography*, 42(6), 1317–1324.
971 <https://doi.org/10.4319/lo.1997.42.6.1317>

972 Moore, C. A., Farmer, C. T., & Zika, R. G. (1993). Influence of the Orinoco River on
973 hydrogen peroxide distribution and production in the eastern Caribbean. *Journal of*
974 *Geophysical Research: Oceans*, 98(C2), 2289–2298. <https://doi.org/10.1029/92JC02767>

975 Moore, S., Gauci, V., Evans, C. D., & Page, S. E. (2011). Fluvial organic carbon losses from a
976 Bornean blackwater river. *Biogeosciences*, 8(4), 901–909.
977 <https://doi.org/10.5194/bg-8-901-2011>

978 Mopper, K., Zhou, X., Kieber, R. J., Kieber, D. J., Sikorski, R. J., & Jones, R. D. (1991).
979 Photochemical degradation of dissolved organic carbon and its impact on the oceanic
980 carbon cycle. *Nature*, 353(6339), 60–62. <https://doi.org/10.1038/353060a0>

981 Moran, M. A., & Zepp, R. G. (1997). Role of photoreactions in the formation of biologically
982 labile compounds from dissolved organic matter. *Limnology and Oceanography*, 42(6),
983 1307–1316. <https://doi.org/10.4319/lo.1997.42.6.1307>

984 Moran, M. A., Sheldon, W. M., & Zepp, R. G. (2000). Carbon loss and optical property
985 changes during long-term photochemical and biological degradation of estuarine
986 dissolved organic matter. *Limnology and Oceanography*, 45(6), 1254–1264.
987 <https://doi.org/10.4319/lo.2000.45.6.1254>

988 Müller, D., Warneke, T., Rixen, T., Müller, M., Jamahari, S., Denis, N., et al. (2015). Lateral
989 carbon fluxes and CO₂ outgassing from a tropical peat-draining river. *Biogeosciences*,
990 12(20), 5967–5979. <https://doi.org/10.5194/bg-12-5967-2015>

- 991 Nichols, R. S., & Martin, P. (2021). Low biodegradability of dissolved organic matter from
992 Southeast Asian peat-draining rivers. *Journal of Geophysical Research: Biogeosciences*.
993 <https://doi.org/10.1029/2020JG006182>
- 994 Painter, S. C., Lapworth, D. J., Woodward, E. M. S., Kroeger, S., Evans, C. D., Mayor, D. J.,
995 & Sanders, R. J. (2018). Terrestrial dissolved organic matter distribution in the North
996 Sea. *Science of the Total Environment*, 630, 630–647.
997 <https://doi.org/10.1016/j.scitotenv.2018.02.237>
- 998 Powers, L. C., & Miller, W. L. (2015). Photochemical production of CO and CO₂ in the
999 Northern Gulf of Mexico: Estimates and challenges for quantifying the impact of
1000 photochemistry on carbon cycles. *Marine Chemistry*, 171, 21–35.
1001 <https://doi.org/10.1016/j.marchem.2015.02.004>
- 1002 Powers, L. C., Brandes, J. A., Miller, W. L., & Stubbins, A. (2017). Using liquid
1003 chromatography-isotope ratio mass spectrometry to measure the $\delta^{13}\text{C}$ of dissolved
1004 inorganic carbon photochemically produced from dissolved organic carbon. *Limnology
1005 and Oceanography: Methods*, 15(1), 103–115. <https://doi.org/10.1002/lom3.10146>
- 1006 Rixen, T., Wit, F., Hutahaean, A. A., Schlüter, A., Baum, A., Klemme, A., et al. (2022). 4 -
1007 Carbon cycle in tropical peatlands and coastal seas. In T. C. Jennerjahn, T. Rixen, H. E.
1008 Irianto, & J. Samiaji (Eds.), *Science for the Protection of Indonesian Coastal
1009 Ecosystems (SPICE)* (pp. 83–142). Elsevier.
1010 <https://doi.org/https://doi.org/10.1016/B978-0-12-815050-4.00011-0>
- 1011 Semiletov, I., Pipko, I., Gustafsson, Ö., Anderson, L. G., Sergienko, V., Pugach, S., et al.

1012 (2016). Acidification of East Siberian Arctic Shelf waters through addition of freshwater
1013 and terrestrial carbon. *Nature Geoscience*, 9(5), 361–365.
1014 <https://doi.org/10.1038/NEGO2695>

1015 Spencer, R. G. M., Stubbins, A., Hernes, P. J., Baker, A., Mopper, K., Aufdenkampe, A. K., et
1016 al. (2009). Photochemical degradation of dissolved organic matter and dissolved lignin
1017 phenols from the Congo River. *Journal of Geophysical Research*, 114(G03010).
1018 <https://doi.org/10.1029/2009JG000968>

1019 Stubbins, A., Spencer, R. G. M., Chen, H., Hatcher, P. G., Mopper, K., Hernes, P. J., et al.
1020 (2010). Illuminated darkness: Molecular signatures of Congo River dissolved organic
1021 matter and its photochemical alteration as revealed by ultrahigh precision mass
1022 spectrometry. *Limnology and Oceanography*, 55(4), 1467–1477.
1023 <https://doi.org/10.4319/lo.2010.55.4.1467>

1024 Stubbins, A., Mann, P. J., Powers, L., Bittar, T. B., Dittmar, T., McIntyre, C. P., et al. (2017).
1025 Low photolability of yedoma permafrost dissolved organic carbon. *Journal of*
1026 *Geophysical Research: Biogeosciences*, 122(1), 200–211.
1027 <https://doi.org/10.1002/2016JG003688>

1028 Susanto, D., Wei, Z., Adi, R., Zhang, Q., Fang, G., Fan, B., et al. (2016). Oceanography
1029 Surrounding Krakatau Volcano in the Sunda Strait, Indonesia. *Oceanography*, 29(2), 0–
1030 29. <https://doi.org/10.5670/oceanog.2016.31>

1031 Tzortziou, M., Osburn, C. L., & Neale, P. J. (2007). Photobleaching of dissolved organic
1032 material from a tidal marsh-estuarine system of the Chesapeake Bay. *Photochemistry*

- 1033 *and Photobiology*, 83(4), 782–792. <https://doi.org/10.1111/j.1751-1097.2007.00142.x>
- 1034 Urtizberea, A., Dupont, N., Rosland, R., & Aksnes, D. L. (2013). Sensitivity of euphotic zone
1035 properties to CDOM variations in marine ecosystem models. *Ecological Modelling*, 256,
1036 16–22. <https://doi.org/10.1016/j.ecolmodel.2013.02.010>
- 1037 Vähätalo, A. V., Salkinoja-Salonen, M., Taalas, P., & Salonen, K. (2000). Spectrum of the
1038 quantum yield for photochemical mineralization of dissolved organic carbon in a humic
1039 lake. *Limnology and Oceanography*, 45(3), 664–676.
1040 <https://doi.org/10.4319/lo.2000.45.3.0664>
- 1041 Vähätalo, A. V., Salonen, K., Münster, U., Järvinen, M., & Wetzel, R. G. (2003).
1042 Photochemical transformation of allochthonous organic matter provides bioavailable
1043 nutrients in a humic lake. *Archiv Fur Hydrobiologie*, 156(3), 287–314.
1044 <https://doi.org/10.1127/0003-9136/2003/0156-0287>
- 1045 Ward, C. P., Nalven, S. G., Crump, B. C., Kling, G. W., & Cory, R. M. (2017). Photochemical
1046 alteration of organic carbon draining permafrost soils shifts microbial metabolic
1047 pathways and stimulates respiration. *Nature Communications*, 8(1), 1–7.
1048 <https://doi.org/10.1038/s41467-017-00759-2>
- 1049 Ward, C. P., Bowen, J. C., Freeman, D. H., & Sharpless, C. M. (2021). Rapid and
1050 reproducible characterization of the wavelength dependence of aquatic photochemical
1051 reactions using light-emitting diodes. *Environmental Science and Technology Letters*,
1052 8(5), 437–442. <https://doi.org/10.1021/acs.estlett.1c00172>
- 1053 Weishaar, J. L., Aiken, G. R., Bergamaschi, B. A., Fram, M. S., Fujii, R., & Mopper, K.

1054 (2003). Evaluation of Specific Ultraviolet Absorbance as an Indicator of the Chemical
1055 Composition and Reactivity of Dissolved Organic Carbon. *Environmental Science &*
1056 *Technology*, 37(20), 4702–4708. <https://doi.org/10.1021/es030360x>

1057 White, E. M., Kieber, D. J., Sherrard, J., Miller, W. L., & Mopper, K. (2010). Carbon dioxide
1058 and carbon monoxide photoproduction quantum yields in the Delaware Estuary. *Marine*
1059 *Chemistry*, 118(1–2), 11–21. <https://doi.org/10.1016/j.marchem.2009.10.001>

1060 Wit, F., Rixen, T., Baum, A., Pranowo, W. S., & Hutahaean, A. A. (2018). The Invisible
1061 Carbon Footprint as a hidden impact of peatland degradation inducing marine carbonate
1062 dissolution in Sumatra, Indonesia. *Scientific Reports*, 8(1), 17403.
1063 <https://doi.org/10.1038/s41598-018-35769-7>

1064 Zepp, R. G. (2007). Solar UVR and aquatic Carbon, nitrogen, sulfur and metals cycles. In E.
1065 W. Helbling & H. Zagarese (Eds.) (pp. 137–184). Cambridge: Royal Society of
1066 Chemistry. <https://doi.org/10.1039/9781847552266-00137>

1067 Zhou, Y., Martin, P., & Müller, M. (2019). Composition and cycling of dissolved organic
1068 matter from tropical peatlands of coastal Sarawak, Borneo, revealed by fluorescence
1069 spectroscopy and parallel factor analysis. *Biogeosciences*, 16(13), 2733–2749.
1070 <https://doi.org/10.5194/bg-16-2733-2019>

1071 Zhou, Y., Evans, C. D., Chen, Y., Chang, K. Y. W., & Martin, P. (2021). Extensive
1072 Remineralization of Peatland-Derived Dissolved Organic Carbon and Ocean
1073 Acidification in the Sunda Shelf Sea, Southeast Asia. *Journal of Geophysical Research:*
1074 *Oceans*, 126(6), 1–23. <https://doi.org/10.1029/2021JC017292>

1075 Zika, R. G. (1981). Chapter 10 Marine Organic Photochemistry. In *Elsevier Oceanography*

1076 *Series* (Vol. 31, pp. 299–325). [https://doi.org/10.1016/S0422-9894\(08\)70332-5](https://doi.org/10.1016/S0422-9894(08)70332-5)

1077

1078

1079

1080

1081

1082

1083

1084

1085

1086

1087

1088

1089

Supporting Information

1090 Photodegradation of dissolved organic carbon derived from tropical peatlands in

1091 the Sunda Shelf Sea, Southeast Asia

1092

1093 Yongli Zhou^{1,*}, †, Moritz Müller², Nagur Cherukuru³, Patrick Martin^{1,*}

1094

1095 ¹Asian School of the Environment, Nanyang Technological University, 639798 Singapore

1096 ²Faculty of Engineering, Computing and Science, Swinburne University of Science and

1097 Technology, 93350 Kuching, Sarawak, Malaysia

1098 ³CSIRO Oceans and Atmosphere Flagship, Canberra ACT 2601, Australia

1099 †Current address: Ecosystem Center, Marine Biological Laboratory, Woods Hole, 02543,

1100 United States

1101

1102 **A1 Apparent quantum yield (AQY) calculations**

1103 **A1.1 Broadband AQY**

1104 The broadband apparent quantum yield ($\phi_{broadband}$) (unit: mol C (mol photons)⁻¹) for tDOC

1105 photo-remineralization was calculated for Exp 1–4 based on the DOC loss and the amount of

1106 photons absorbed following Fichot & Benner (2014) with the wavelength range modified:

$$1107 \quad \phi_{broadband} = \frac{DOC_{initial} - DOC_{final}}{\int_{t_0}^{t_{final}} \int_{290nm}^{700nm} \Xi((\lambda, t)) d\lambda dt} \quad (S1)$$

1108 where DOC is the amount of DOC (mol) in the sample; $\Xi(\lambda, t)$ is the downwelling

1109 irradiance absorbed by CDOM in the quartz cell (mol photons nm⁻¹ s⁻¹); λ denotes

1110 wavelength (nm); t denotes time (s). $\Xi(\lambda, t)$ was calculated following Fichot & Benner
1111 (2014):

$$1112 \quad \Xi(\lambda, t) = E_d(\lambda) T S (1 - e^{-K_{d,cell}(\lambda, t) PL}) \frac{a_g(\lambda, t)}{K_{d,cell}(\lambda, t)} \quad (S2)$$

1113 where $E_d(\lambda)$ is the downwelling irradiance spectrum of the xenon lamp just above the
1114 quartz cell (mol photons $\text{nm}^{-1} \text{s}^{-1} \text{m}^{-2}$, kept constant during the experiments); T (unitless) is
1115 the transmittance of the quartz window (0.95); S is the surface area (m^2) of the cuvette; and
1116 PL is the thickness (m) of the sample solution in the quartz cell. $K_{d,cell}(\lambda, t)$ is the diffuse
1117 attenuation coefficient of downwelling irradiance (m^{-1}) in the sample solution, which is the
1118 sum of the absorption of CDOM ($a_{CDOM}(\lambda, t)$) (m^{-1}), the absorption of water ($a_w(\lambda)$) (m^{-1})
1119 and the backscattering of water ($bb_w(\lambda)$) (m^{-1}) following Fichot and Benner (2014):

$$1120 \quad K_{d,cell}(\lambda, t) \cong a_{CDOM}(\lambda, t) + a_w(\lambda) + bb_w(\lambda) \quad (S3).$$

1121 Because the samples were filtered, we did not include particulate absorption and
1122 backscattering here in the calculations. Note that the absorption of CDOM ($a_{CDOM}(\lambda, t)$)
1123 decreases over time due to photobleaching. It was measured at regular intervals during each
1124 experiment, and the mean absorption of every two consecutive time points was used to
1125 calculate the absorbed photons $\Xi(\lambda, t)$ for the corresponding time interval. $E_d(\lambda)$ was
1126 measured from 177 nm to 872 nm at 1 nm resolution with an Ocean Insights FLAME
1127 radiometer, and the spectrum between 290 nm and 318 nm was derived by linear
1128 interpolation assuming zero irradiance at ≤ 290 nm.

1129

1130

1131 **A1.2 Spectrally resolved AQY**

1132 The spectrally resolved AQY for tDOC photo-remineralization ($\phi_{DOC}(\lambda)$) was calculated for
1133 each experiment as in Aarnos et al. (2018). The $\phi_{DOC}(\lambda)$ was assumed to decrease
1134 exponentially with increasing wavelength (Gao & Zepp, 1998):

1135
$$\phi_{DOC}(\lambda) = c e^{-d\lambda} \quad (S4)$$

1136 where c (mol C (mol photons)⁻¹ nm⁻¹) and d (nm⁻¹) are positive constants. The amount of the
1137 photo-remineralized DOC can be related to the AQY spectrum $\phi_{DOC}(\lambda)$ and the absorbed
1138 irradiance $\Xi((\lambda, t)$:

1139
$$DOC_{initial} - DOC_{final} = \int_{t_{initial}}^{t_{final}} \int_{290nm}^{700nm} \phi_{DOC}(\lambda) \Xi((\lambda, t) d\lambda dt \quad (S5).$$

1140 Therefore, c and d in Eq. 4 were iterated until the right side of Eq. S5 was as close as possible
1141 to the measured DOC loss, i.e., the left side of Eq. 5 using the *fminsearch* function of
1142 MATLAB. Because the optimized values of c and d are dependent on the starting values
1143 provided for iteration, a Monte Carlo approach was used to perturb the starting values and
1144 generate multiple combinations of c and d (Gu et al., 2017). The combination that provided
1145 the best fit between the modeled DOC loss and the measured DOC loss was selected (see
1146 Supporting Information in Aarnos et al., (2018)).

1147

1148 The concept of AQY was extended to the dose-dependent decrease in CDOM absorption. We
1149 refer to this as $\phi_{CDOM}(\lambda)$, which is the spectrally resolved AQY for the decrease in the
1150 volume-integrated CDOM absorption coefficient, with units of L m⁻¹ (mol photons)⁻¹ nm⁻¹.
1151 For example, the decrease in the volume-integrated Napierian absorption coefficient at 350

1152 nm (a_{350}) can be related to its spectrally resolved AQY $\phi_{a_{350}}(\lambda)$ and the absorbed irradiance
1153 $\Xi(\lambda, t)$ as:

$$1154 \quad (a_{350,initial} - a_{350,final} V) = \int_{t_{initial}}^{t_{final}} \int_{290nm}^{700nm} \phi_{a_{350}}(\lambda) \Xi(\lambda, t) d\lambda dt \quad (S6)$$

1155 where V is the volume (in L) of the sample solution. To obtain the volume-integrated CDOM
1156 absorption, the measured absorption coefficient is multiplied by the volume of the water
1157 sample, yielding $L m^{-1}$. We assumed that, like $\phi_{DOC}(\lambda)$, the $\phi_a(\lambda)$ decreases exponentially
1158 with increasing wavelength. For a_{350} , we have:

$$1159 \quad \phi_{a_{350}}(\lambda) = c' e^{-d'\lambda} \quad (S7)$$

1160 where c' ($L m^{-1} nm^{-1}$) and d' (nm^{-1}) are positive constants, which were iterated until the
1161 right side of Eq. S6 was as close as possible to the left side of Eq. S6 using the *fminsearch*
1162 function of MATLAB. This calculation was repeated across the CDOM absorption spectrum
1163 at 1-nm resolution from 250–700 nm, which returned 451 respective AQY spectra, i.e., AQY
1164 spectrum for a_{250} , AQY spectrum for a_{251} , AQY spectrum for a_{252} , ..., AQY spectrum for a_{691} ,
1165 AQY spectrum for a_{700} . Concatenating all these 1-dimensional AQY spectra returned the
1166 2-dimensional AQY spectrum shown in Figure 4b.

1167

1168

1169

1170 **A2 Photodegradation model**

1171 **A2.1 Model calculations**

1172 The DOC concentration at time T was calculated from its value at time $T-I$ and the amount of

1173 DOC consumed during the period between $T-1$ and T as:

$$1174 \quad DOC_T = DOC_{T-1} - \frac{\int_{T-1}^T pr_{DOC}(t) dt}{V} S \quad (S8)$$

1175 where $pr_{DOC}(t)$ is the areal rate of photo-remineralization of tDOC ($\text{mol C m}^{-2} \text{s}^{-1}$), S is the
1176 surface area of the water column under consideration (i.e., 1 m^2) and V is the volume of the
1177 water column (m^3), which was calculated from the water depth (Section 2.5.3) and surface
1178 area (1 m^2 here). The $pr_{DOC}(t)$ was calculated from the AQY spectrum ($\phi_{DOC}(\lambda)$) and the
1179 number of photons absorbed by CDOM ($\Xi(\lambda, t)$) in the water column:

$$1180 \quad pr_{DOC}(t) = \int_{300nm}^{700nm} \phi_{DOC}(\lambda) \Xi(\lambda, t) d\lambda \quad (S9).$$

1181 The irradiance absorbed by CDOM, $\Xi(\lambda, t)$, was calculated as:

$$1182 \quad \Xi(\lambda, t) = E_{o,0^-}(\lambda, t) (1 - e^{-K_o(\lambda, t) D}) f_{CDOM}(\lambda, t) \quad (S10)$$

1183 where $E_{o,0^-}(\lambda, t)$ is the total (i.e. upwelling + downwelling) scalar irradiance just below the
1184 water surface, $K_o(\lambda, t)$ is the diffuse attenuation coefficient of scalar irradiance, D is the
1185 water depth and $f_{CDOM}(\lambda, t)$ is the wavelength- and time-specific fraction of irradiance that
1186 is absorbed by CDOM. The right side of Eq. 10, except the term $f_{CDOM}(\lambda, t)$, calculates the
1187 total absorbed irradiance in the water column. We neglected the irradiance below 300 nm
1188 because the particulate absorption spectra, which were used for the calculation of K_o (see
1189 below), were not available below 300 nm. To assess the error caused by neglecting the
1190 irradiance below 300 nm, we used the simulated solar irradiance spectrum from 300–700 nm,
1191 and the AQY spectra for DOC photo-remineralization and CDOM photobleaching to
1192 back-calculate the DOC loss for our photodegradation Exp 1. The results only differed by 1.6%
1193 from the measured DOC loss, which shows that neglecting the irradiance below 300 nm only

1194 introduces a minimal error.

1195

1196 Because the upwelling irradiance is generally very small in waters that are optically deep,
1197 $E_{o,0^-}(\lambda, t)$ was approximated as the downwelling scalar irradiance, $E_{od,0^-}(\lambda, t)$, which was
1198 derived from the total (i.e. diffuse + direct) downwelling irradiance just above the water
1199 surface, $E_{d,0^+}(\lambda, t)$ (see Section 2.5.3), following (Fichot & Miller, 2010). $K_o(\lambda, t)$ was
1200 approximated using the diffuse attenuation coefficient of downwelling irradiance, $K_d(\lambda, t)$
1201 (Fichot & Miller, 2010). Therefore, Eq. 10 can be rewritten as Eq. 11 and was used in our
1202 model:

$$1203 \quad \Xi(\lambda, t) = E_{od,0^-}(\lambda, t) (1 - e^{-K_d(\lambda, t) D}) f_{CDOM}(\lambda, t) \quad (S11).$$

1204

1205 Light attenuation $K_d(\lambda, t)$ was calculated following Lee et al. (2005):

$$1206 \quad K_d(\lambda, t) = (1 + 0.005 \theta(t)) a_{tot}(\lambda, t) + 1.48 (1 - 0.52 e^{-10.8 a_{tot}(\lambda, t)}) b_{b_{tot}}(\lambda) \quad (S12)$$

1207 where $\theta(t)$ is the solar zenith angle above the water surface (degrees), $a_{tot}(\lambda, t)$ is the
1208 total absorption coefficient and $b_{b_{tot}}(\lambda)$ is the total backscattering coefficient in the shelf
1209 waters:

$$1210 \quad a_{tot}(\lambda, t) = a_{CDOM}(\lambda, t) + a_p(\lambda) + a_w(\lambda) \quad (S13)$$

$$1211 \quad b_{b_{tot}}(\lambda) = b_{b_p}(\lambda) + b_{b_w}(\lambda) \quad (S14)$$

1212 where the subscripts $CDOM$, p , w denote CDOM, particulates, and water, respectively.

1213 Particulate absorption and backscattering spectra were taken from in-situ measurements in

1214 our two model regions and were assumed to be constant over time.

1215

1216 The fraction of irradiance absorbed by CDOM, $f_{CDOM}(\lambda, t)$, was calculated as:

1217
$$f_{CDOM}(\lambda, t) = \frac{(1+0.005 \theta(t)) a_{CDOM}(\lambda, t)}{K_d(\lambda, t)} \quad (S15)$$

1218 where the numerator is the diffuse attenuation coefficient of downwelling irradiance that is
1219 only caused by CDOM absorption, while the denominator is the actual K_d calculated from
1220 CDOM, particles, and water.

1221

1222 In Eq. S15, the CDOM spectrum at time point T , $a_{CDOM}(\lambda, T)$, can be calculated from the
1223 CDOM spectrum at time point $T-1$ and the amount of CDOM that was photobleached
1224 between $T-1$ and T . For example, for a_{350} :

1225
$$a_{350, T} = a_{350, T-1} - \frac{\int_{T-1}^T pr_{a_{350}}(t) dt}{V} S \quad (S16)$$

1226 where $pr_{a_{350}}(t)$ is the areal rate of decrease in the volume-integrated a_{350} , S is the surface
1227 area of the water column (i.e., 1 m²) and V is the volume of the water column. The $pr_{a_{350}}(t)$
1228 was calculated as:

1229
$$pr_{a_{350}}(t) = \int_{300nm}^{700nm} \phi_{a_{350}}(\lambda) \Xi(\lambda, t) d\lambda \quad (S17)$$

1230 where $\phi_{a_{350}}(\lambda)$ is the spectrally resolved AQY for the decrease in the volume-integrated
1231 a_{350} of CDOM (Eq. S7); $\Xi(\lambda, t)$ is the number of photons absorbed by CDOM (Eq. S11).

1232 Because $pr_{a_{350}}(t)$ needs to be calculated from $a_{350}(t)$, Eq. S16 cannot be solved. Thus, in
1233 practice, the $\int_{T-1}^T pr_{a_{350}}(t) dt$ in Eq. S16 was approximated as $pr_{a_{350, T-1}} \Delta T$. Our results
1234 show that the daily change in CDOM absorption coefficient is small enough to allow this
1235 approximation. This calculation was applied across the CDOM spectrum at 1nm resolution

1236 from 250–700 nm to obtain $a_{CDOM}(\lambda, t)$.

1237

1238

1239

1240 **A2.2 Model input data**

1241 **A2.2.1 Solar irradiance**

1242 The downwelling irradiance spectrum above the water surface, $E_{d,0^+}(\lambda, t)$, and the solar
1243 zenith angle, $\theta(t)$, for each time point were obtained from the Tropospheric Ultraviolet and
1244 Visible (TUV) Radiation Model (US National Center for Atmospheric Research,
1245 [https://www2.acom.ucar.edu/modeling/tropospheric-ultraviolet-and-visible-tuv-radiation-mo](https://www2.acom.ucar.edu/modeling/tropospheric-ultraviolet-and-visible-tuv-radiation-model)
1246 [del](https://www2.acom.ucar.edu/modeling/tropospheric-ultraviolet-and-visible-tuv-radiation-model)). Data were obtained on an hourly basis for the 15th day of each month of 2019 for two
1247 locations: 0.5°N 104.5°E, representative of the southern Malacca Strait, and 1.9°N 109.7°E,
1248 representative of the Talang Region. For both locations, $E_{d,0^+}(\lambda, t)$ under clear-sky and
1249 cloud-corrected conditions was obtained. The overhead ozone column, the optical depth of
1250 clouds, and the optical depth of aerosols as input parameters for the TUV model were
1251 obtained from NASA Earth Observations (<https://neo.sci.gsfc.nasa.gov/>).

1252

1253 **A2.2.2 Particulate absorption and backscattering**

1254 For the southern Malacca Strait, particulate absorption and backscattering coefficients were
1255 obtained from bi-monthly measurements in the Singapore Strait between December 2018 to
1256 December 2020 (Martin et al., 2021). For the Talang Region, particulate absorption and

1257 backscattering coefficients were measured in September 2017 at multiple stations between
1258 the estuary of the Samunsam River and the Talang Islands (Cherukuru et al., 2021). For both
1259 regions, the particulate absorption coefficients were measured on samples filtered onto glass
1260 fiber filters using an integrating sphere accessory on a spectrophotometer, while particulate
1261 backscattering coefficients were measured at 9 wavelengths using a Wetlabs BB9 lowered to
1262 1m depth below water surface. Detailed methods can be found in Martin et al. (2021) and
1263 Cherukuru et al. (2021).

1264

1265 We fit a power-law function to each sample particulate backscattering spectrum ($R^2 = 0.05$ –
1266 0.78 for the Southern Malacca Strait, samples with $R^2 < 0.34$ were neglected; $R^2 = 0.68$ – 0.80
1267 for Talang Region) to obtain spectra from 300–700 nm at 1-nm resolution. We calculated the
1268 mean and standard deviation of the particulate absorption and backscattering spectra as the
1269 model input parameters (i.e., $a_p(\lambda)$ and $b_{b_p}(\lambda)$).

1270

1271 **A2.2.3 Starting values of DOC concentration and CDOM absorption**

1272 The initial DOC concentration for the southern Malacca Strait was calculated by assuming
1273 conservative mixing between peatland-draining rivers on Sumatra and seawater to a salinity
1274 of 29, which is approximately the lowest salinity in the Singapore Strait during the periods
1275 with strong terrestrial input (Zhou et al., 2021):

$$1276 \quad \text{DOC}(t_0) = \text{DOC}_{\text{Sumatra}} \times f_{\text{river}} \quad (\text{S18})$$

1277 where $\text{DOC}_{\text{Sumatra}}$ is the discharge-weighted average of riverine endmember DOC

1278 concentration of the major rivers on Sumatra ($890 \mu\text{mol L}^{-1}$) (Wit et al., 2018), and f_{river} is
1279 the fraction of freshwater in the modeling regions. Note that a marine DOC component was
1280 not included in Eq. 18 because we only model the photodegradation of terrigenous DOC here.
1281 In addition, marine CDOM was found in very low concentration in these oligotrophic waters
1282 (Martin et al., 2021), so neglecting the marine CDOM does not affect our estimates of light
1283 absorption by CDOM.

1284

1285 The f_{river} was calculated from salinity:

$$1286 \quad f_{river} = \left(1 - \frac{sal_{mod}}{sal_{marine}}\right) \quad (\text{S19})$$

1287 where sal_{mod} is the salinity in the modeling region (i.e., 29) and sal_{marine} is the marine
1288 endmember salinity for the water from the open South China Sea, which is taken as 33
1289 following Zhou et al. (2021). These calculations returned an initial DOC concentration of 108
1290 $\mu\text{mol L}^{-1}$ for the modeling for the Southern Malacca Strait.

1291

1292 CDOM spectral data from Sumatran rivers are not available. The DOC-specific absorbance at
1293 254 nm (SUVA_{254}) of the Maludam River ($5\text{--}6 \text{ L mg}^{-1} \text{ m}^{-1}$) is comparable to that of other
1294 peatland-draining rivers in northwestern Borneo (Martin et al., 2018), and we take the
1295 CDOM-to-DOC ratio of the Maludam River as representative of peatland-draining rivers in
1296 Southeast Asia. Therefore, we calculated the initial CDOM spectrum for the Southern
1297 Malacca Strait based on the DOC-specific CDOM absorption spectrum of the Maludam River
1298 and our riverine end-member DOC concentration for Sumatra ($890 \mu\text{mol L}^{-1}$):

1299
$$a_{CDOM, initial}(\lambda) = \frac{a_{CDOM, Maludam}(\lambda)}{DOC_{Maludam}} \times DOC_{Sumatra} \times f_{river} \quad (S20)$$

1300 where $a_{CDOM, Maludam}(\lambda)$ and $DOC_{Maludam}$ is the CDOM spectrum and DOC
 1301 concentration, respectively, of the Maludam River water sample (collected in December
 1302 2017). The starting CDOM absorption spectrum in Day 1 for modeling is shown in Fig. S3e.

1303

1304 For the Talang Region, the starting DOC concentration and the CDOM absorption spectrum
 1305 in Day 1 were calculated by assuming conservative mixing between the Samunsam River
 1306 water and seawater to salinity of 29 using Eqns. S18–S20. Riverine endmember DOC
 1307 concentration and CDOM absorption in the Samunsam River were measured in March and
 1308 September 2017 (Martin et al., 2018). Calculations using the annual mean riverine DOC
 1309 concentration of $1493 \mu\text{mol L}^{-1}$ returned an initial DOC concentration of $181 \mu\text{mol L}^{-1}$ and an
 1310 initial CDOM absorption spectrum (Fig. S3f) for modeling for the Talang Region.

1311

1312 A2.3 Photochemical decay constant of UniDOM

1313 First, we calculated the depth-normalized photochemical decay constant, \emptyset , based on the
 1314 monthly loss of DOC of year 1 from our modeling results under the cloud-corrected
 1315 conditions:

1316
$$\emptyset = \frac{\ln(DOC_{t1}) - \ln(DOC_{t2})}{\Delta t} \quad (S21)$$

1317 where DOC_{t1} and DOC_{t2} is the DOC concentration in the first and the last day of the
 1318 month, respectively. We then converted the \emptyset to \emptyset^{ref} based on equations in Anderson et al.
 1319 (2019):

1320
$$\phi^{ref} = \frac{\phi \times D}{\frac{1}{k_{UV}} - \frac{e^{-k_{UV} D}}{k_{UV}}} \quad (S22)$$

1321 where D is the water depth and k_{UV} is the extinction coefficient, which was approximated
1322 using the water UV attenuation, k_{UVW} , (0.12 m⁻¹) and CDOM decadic absorption coefficient
1323 at 350nm, k_{350} :

1324
$$k_{UV} = k_{UVW} + k_{350} \quad (S23).$$

1325 This returned ϕ^{ref} for each month and we report the mean value to account for the seasonal
1326 variation in solar irradiance. A decline in the decay constant with age proposed by Anderson
1327 et al. (2019) was not considered in our calculation because we did not observe a decrease in
1328 the apparent quantum yield over the course of our photodegradation experiments (Table S4).

1329

1330

1331 **References in Supporting information**

1332 Aarnos, H., Ylöstalo, P., & Vähätalo, A. V. (2012). Seasonal phototransformation of dissolved
1333 organic matter to ammonium, dissolved inorganic carbon, and labile substrates
1334 supporting bacterial biomass across the Baltic Sea. *Journal of Geophysical Research:*
1335 *Biogeosciences*, 117(1), 1–14. <https://doi.org/10.1029/2010JG001633>

1336 Aarnos, H., Gélinas, Y., Kasurinen, V., Gu, Y., Puupponen, V. M., & Vähätalo, A. V. (2018).
1337 Photochemical Mineralization of Terrigenous DOC to Dissolved Inorganic Carbon in
1338 Ocean. *Global Biogeochemical Cycles*, 32(2), 250–266.
1339 <https://doi.org/10.1002/2017GB005698>

1340 Aksnes, D. L., Dupont, N., Staby, A., Fiksen, Ø., Kaartvedt, S., & Aure, J. (2009). Coastal

1341 water darkening and implications for mesopelagic regime shifts in Norwegian fjords.
1342 *Marine Ecology Progress Series*, 387(Jerlov 1968), 39–49.
1343 <https://doi.org/10.3354/meps08120>

1344 Alkhatib, M., Jennerjahn, T. C., & Samiaji, J. (2007). Biogeochemistry of the Dumai River
1345 estuary, Sumatra, Indonesia, a tropical black-water river. *Limnology and Oceanography*,
1346 52(6), 2410–2417. <https://doi.org/10.4319/lo.2007.52.6.2410>

1347 Alleson, L., Koehler, B., Thrane, J. E., Andersen, T., & Hessen, D. O. (2021). The role of
1348 photomineralization for CO₂ emissions in boreal lakes along a gradient of dissolved
1349 organic matter. *Limnology and Oceanography*, 66(1), 158–170.
1350 <https://doi.org/10.1002/lno.11594>

1351 Anderson, T. R., Rowe, E. C., Polimene, L., Tipping, E., Evans, C. D., Barry, C. D. G., et al.
1352 (2019). Unified concepts for understanding and modelling turnover of dissolved organic
1353 matter from freshwaters to the ocean: the UniDOM model. *Biogeochemistry*, 146(2),
1354 105–123. <https://doi.org/10.1007/s10533-019-00621-1>

1355 Apell, J. N., & McNeill, K. (2019). Updated and validated solar irradiance reference spectra
1356 for estimating environmental photodegradation rates. *Environmental Science: Processes
1357 and Impacts*, 21(3), 427–437. <https://doi.org/10.1039/c8em00478a>

1358 Baum, A., Rixen, T., & Samiaji, J. (2007). Relevance of peat draining rivers in central
1359 Sumatra for the riverine input of dissolved organic carbon into the ocean. *Estuarine,
1360 Coastal and Shelf Science*, 73(3–4), 563–570. <https://doi.org/10.1016/j.ecss.2007.02.012>

1361 Beleites, C., & Sergio, V. (2012). hyperSpec: a package to handle hyperspectral data sets in R.

- 1362 *Journal of Statistical Software.*
- 1363 Cai, W.-J. (2011). Estuarine and Coastal Ocean Carbon Paradox: CO₂ Sinks or Sites of
1364 Terrestrial Carbon Incineration? *Annual Review of Marine Science*, 3(1), 123–145.
1365 <https://doi.org/10.1146/annurev-marine-120709-142723>
- 1366 Catalán, N., Marcé, R., Kothawala, D. N., & Tranvik, L. J. (2016). Organic carbon
1367 decomposition rates controlled by water retention time across inland waters. *Nature*
1368 *Geoscience*, 9(7), 501–504. <https://doi.org/10.1038/ngeo2720>
- 1369 Chen, H., Abdulla, H. A. N., Sanders, R. L., Myneni, S. C. B., Mopper, K., & Hatcher, P. G.
1370 (2014). Production of Black Carbon-like and Aliphatic Molecules from Terrestrial
1371 Dissolved Organic Matter in the Presence of Sunlight and Iron. *Environmental Science*
1372 *and Technology Letters*, 1(10), 399–404. <https://doi.org/10.1021/ez5002598>
- 1373 Cherukuru, N., Martin, P., Sanwlani, N., Mujahid, A., & Müller, M. (2021). A semi-analytical
1374 optical remote sensing model to estimate suspended sediment and dissolved organic
1375 carbon in tropical coastal waters influenced by peatland-draining river discharges off
1376 sarawak, borneo. *Remote Sensing*, 13(1), 1–31. <https://doi.org/10.3390/rs13010099>
- 1377 Ciais, P., Sabine, C., & Bala, G. (2013). Chapter 6: Carbon and other biogeochemical cycles.
1378 *Climate Change 2013: The Physical Science Basis.*
- 1379 Cory, R. M., & Kling, G. W. (2018). Interactions between sunlight and microorganisms
1380 influence dissolved organic matter degradation along the aquatic continuum. *Limnology*
1381 *and Oceanography Letters*, 3(3), 102–116. <https://doi.org/10.1002/lol2.10060>
- 1382 Cory, R. M., McKnight, D. M., Chin, Y. P., Miller, P., & Jaros, C. L. (2007). Chemical

1383 characteristics of fulvic acids from Arctic surface waters: Microbial contributions and
1384 photochemical transformations. *Journal of Geophysical Research: Biogeosciences*,
1385 *112*(4), 1–14. <https://doi.org/10.1029/2006JG000343>

1386 Dittmar, T., Whitehead, K., Minor, E. C., & Koch, B. P. (2007). Tracing terrigenous dissolved
1387 organic matter and its photochemical decay in the ocean by using liquid
1388 chromatography/mass spectrometry. *Marine Chemistry*, *107*(3), 378–387.
1389 <https://doi.org/10.1016/j.marchem.2007.04.006>

1390 Evans, C. D., Futter, M. N., Moldan, F., Valinia, S., Frogbrook, Z., & Kothawala, D. N.
1391 (2017). Variability in organic carbon reactivity across lake residence time and trophic
1392 gradients. *Nature Geoscience*, *10*(11), 832–835. <https://doi.org/10.1038/NGEO3051>

1393 Fichot, C. G., & Benner, R. (2014). The fate of terrigenous dissolved organic carbon in a
1394 river-influenced ocean margin. *Global Biogeochemical Cycles*, *28*(3), 300–318.
1395 <https://doi.org/10.1002/2013GB004670>

1396 Fichot, C. G., & Miller, W. L. (2010). An approach to quantify depth-resolved marine
1397 photochemical fluxes using remote sensing: Application to carbon monoxide (CO)
1398 photoproduction. *Remote Sensing of Environment*, *114*(7), 1363–1377.
1399 <https://doi.org/10.1016/j.rse.2010.01.019>

1400 Gao, H., & Zepp, R. G. (1998). Factors influencing photoreactions of dissolved organic
1401 matter in a coastal river of the southeastern United States. *Environmental Science and*
1402 *Technology*, *32*(19), 2940–2946. <https://doi.org/10.1021/es9803660>

1403 GEBCO Compilation Group. (2020). GEBCO 2020 Grid.

1404 <https://doi.org/10.5285/a29c5465-b138-234d-e053-6c86abc040b9>

1405 Giesen, W., Wijedasa, L. S., & Page, S. E. (2018). Unique Southeast Asian peat swamp forest
1406 habitats have relatively few distinctive plant species. *Mires and Peat*, 22, 1–13.
1407 <https://doi.org/10.19189/MaP.2017.OMB.287>

1408 Gu, Y., Lensu, A., Perämäki, S., Ojala, A., & Vähätalo, A. V. (2017). Iron and pH Regulating
1409 the Photochemical Mineralization of Dissolved Organic Carbon. *ACS Omega*, 2(5),
1410 1905–1914. <https://doi.org/10.1021/acsomega.7b00453>

1411 Helms, J. R., Stubbins, A., Ritchie, J. D., Minor, E. C., Kieber, D. J., & Mopper, K. (2008).
1412 Absorption spectral slopes and slope ratios as indicators of molecular weight, source,
1413 and photobleaching of chromophoric dissolved organic matter. *Limnology and*
1414 *Oceanography*, 53(3), 955–969. <https://doi.org/10.4319/lo.2008.53.3.0955>

1415 Helms, J. R., Stubbins, A., Perdue, E. M., Green, N. W., Chen, H., & Mopper, K. (2013).
1416 Photochemical bleaching of oceanic dissolved organic matter and its effect on
1417 absorption spectral slope and fluorescence. *Marine Chemistry*, 155, 81–91.
1418 <https://doi.org/10.1016/j.marchem.2013.05.015>

1419 Helms, J. R., Mao, J., Schmidt-Rohr, K., Abdulla, H., & Mopper, K. (2013). Photochemical
1420 flocculation of terrestrial dissolved organic matter and iron. *Geochimica et*
1421 *Cosmochimica Acta*, 121, 398–413. <https://doi.org/10.1016/j.gca.2013.07.025>

1422 Jankowski, J. J., Kieber, D. J., & Mopper, K. (1999a). Nitrate and nitrite ultraviolet
1423 actinometers. *Photochemistry and Photobiology*, 70(3), 319–328.
1424 <https://doi.org/10.1111/j.1751-1097.1999.tb08143.x>

- 1425 Jankowski, J. J., Kieber, D. J., & Mopper, K. (1999b). Nitrate and Nitrite Ultraviolet
1426 Actinometers. *Photochemistry and Photobiology*, 70(3), 319–328.
1427 <https://doi.org/10.1111/j.1751-1097.1999.tb08143.x>
- 1428 Johannessen, S. C., & Miller, W. L. (2001). Quantum yield for the photochemical production
1429 of dissolved inorganic carbon in seawater. *Marine Chemistry*, 76(4), 271–283.
1430 [https://doi.org/10.1016/S0304-4203\(01\)00067-6](https://doi.org/10.1016/S0304-4203(01)00067-6)
- 1431 Judd, K. E., Crump, B. C., & Kling, G. W. (2007). Bacterial responses in activity and
1432 community composition to photo-oxidation of dissolved organic matter from soil and
1433 surface waters. *Aquatic Sciences*, 69(1), 96–107.
1434 <https://doi.org/10.1007/s00027-006-0908-4>
- 1435 Kaiser, K., Benner, R., & Amon, R. M. W. (2017). The fate of terrigenous dissolved organic
1436 carbon on the Eurasian shelves and export to the North Atlantic. *Journal of Geophysical*
1437 *Research: Oceans*, 122(1), 4–22. <https://doi.org/10.1002/2016JC012380>
- 1438 Kaushal, N., Sanwlani, N., Tanzil, J. T. I., Cherukuru, N., Sahar, S., Müller, M., et al. (2021).
1439 Coral Skeletal Luminescence Records Changes in Terrestrial Chromophoric Dissolved
1440 Organic Matter in Tropical Coastal Waters. *Geophysical Research Letters*, 48(8), 1–12.
1441 <https://doi.org/10.1029/2020GL092130>
- 1442 Kitidis, V., Shutler, J. D., Ashton, I., Warren, M., Brown, I., Findlay, H., et al. (2019). Winter
1443 weather controls net influx of atmospheric CO₂ on the north-west European shelf.
1444 *Scientific Reports*, 9(1), 1–11. <https://doi.org/10.1038/s41598-019-56363-5>
- 1445 Koehler, B., Landelius, T., Weyhenmeyer, G. A., Machida, N., & Tranvik, L. J. (2014).

1446 Sunlight-induced carbon dioxide emissions from inland waters. *Global Biogeochemical*
1447 *Cycles*, 28(7), 696–711. <https://doi.org/10.1002/2014GB004850>

1448 Koehler, B., Broman, E., & Tranvik, L. J. (2016). Apparent quantum yield of photochemical
1449 dissolved organic carbon mineralization in lakes. *Limnology and Oceanography*, 61(6),
1450 2207–2221. <https://doi.org/10.1002/lno.10366>

1451 Koehler, B., Powers, L. C., Cory, R. M., Einarsdóttir, K., Gu, Y., Tranvik, L. J., et al. (2022).
1452 Inter-laboratory differences in the apparent quantum yield for the photochemical
1453 production of dissolved inorganic carbon in inland waters and implications for
1454 photochemical rate modeling. *Limnology and Oceanography: Methods*, 320–337.
1455 <https://doi.org/10.1002/lom3.10489>

1456 Lee, Z. P., Du, K. P., & Arnone, R. (2005). A model for the diffuse attenuation coefficient of
1457 downwelling irradiance. *Journal of Geophysical Research C: Oceans*, 110(2), 1–10.
1458 <https://doi.org/10.1029/2004JC002275>

1459 Martin, P., Cherukuru, N., Tan, A. S. Y., Sanwlan, N., Mujahid, A., & Müller, M. (2018).
1460 Distribution and cycling of terrigenous dissolved organic carbon in peatland-draining
1461 rivers and coastal waters of Sarawak, Borneo. *Biogeosciences*, 15(22), 6847–6865.
1462 <https://doi.org/10.5194/bg-15-6847-2018>

1463 Martin, P., Sanwlan, N., Lee, T., Wong, J., Chang, K., Wong, E., & Liew, S. (2021).
1464 Dissolved organic matter from tropical peatlands reduces shelf sea light availability in
1465 the Singapore Strait, Southeast Asia. *Marine Ecology Progress Series*.
1466 <https://doi.org/10.3354/meps13776>

- 1467 Martin, P., Moynihan, M. A., Chen, S., Woo, O. Y., Zhou, Y., Nichols, R. S., et al. (2022).
1468 Monsoon-driven biogeochemical dynamics in an equatorial shelf sea: Time-series
1469 observations in the Singapore Strait. *Estuarine, Coastal and Shelf Science*, 270(April),
1470 107855. <https://doi.org/10.1016/j.ecss.2022.107855>
- 1471 Massicotte, P., Asmala, E., Stedmon, C., & Markager, S. (2017). Global distribution of
1472 dissolved organic matter along the aquatic continuum: Across rivers, lakes and oceans.
1473 *Science of The Total Environment*, 609, 180–191.
1474 <https://doi.org/10.1016/j.scitotenv.2017.07.076>
- 1475 Mathis, M., Logemann, K., Maerz, J., Lacroix, F., Hagemann, S., Chegini, F., et al. (2022).
1476 Seamless Integration of the Coastal Ocean in Global Marine Carbon Cycle Modeling.
1477 *Journal of Advances in Modeling Earth Systems*, 14(8), 1–44.
1478 <https://doi.org/10.1029/2021MS002789>
- 1479 Mayer, B., Stacke, T., Stottmeister, I., & Pohlmann, T. (2015). Sunda Shelf Seas: flushing
1480 rates and residence times. *Ocean Science Discussions*, 12(3), 863–895.
1481 <https://doi.org/10.5194/osd-12-863-2015>
- 1482 Mayer, B., Rixen, T., & Pohlmann, T. (2018). The spatial and temporal variability of air-sea
1483 CO₂ fluxes and the effect of net coral reef calcification in the Indonesian Seas: A
1484 numerical sensitivity study. *Frontiers in Marine Science*, 5(APR), 1–19.
1485 <https://doi.org/10.3389/fmars.2018.00116>
- 1486 Miller, W. L., & Moran, M. A. (1997). Interaction of photochemical and microbial processes
1487 in the degradation of refractory dissolved organic matter from a coastal marine

1488 environment. *Limnology and Oceanography*, 42(6), 1317–1324.
1489 <https://doi.org/10.4319/lo.1997.42.6.1317>

1490 Moore, C. A., Farmer, C. T., & Zika, R. G. (1993). Influence of the Orinoco River on
1491 hydrogen peroxide distribution and production in the eastern Caribbean. *Journal of*
1492 *Geophysical Research: Oceans*, 98(C2), 2289–2298. <https://doi.org/10.1029/92JC02767>

1493 Moore, S., Gauci, V., Evans, C. D., & Page, S. E. (2011). Fluvial organic carbon losses from a
1494 Bornean blackwater river. *Biogeosciences*, 8(4), 901–909.
1495 <https://doi.org/10.5194/bg-8-901-2011>

1496 Mopper, K., Zhou, X., Kieber, R. J., Kieber, D. J., Sikorski, R. J., & Jones, R. D. (1991).
1497 Photochemical degradation of dissolved organic carbon and its impact on the oceanic
1498 carbon cycle. *Nature*, 353(6339), 60–62. <https://doi.org/10.1038/353060a0>

1499 Moran, M. A., & Zepp, R. G. (1997). Role of photoreactions in the formation of biologically
1500 labile compounds from dissolved organic matter. *Limnology and Oceanography*, 42(6),
1501 1307–1316. <https://doi.org/10.4319/lo.1997.42.6.1307>

1502 Moran, M. A., Sheldon, W. M., & Zepp, R. G. (2000). Carbon loss and optical property
1503 changes during long-term photochemical and biological degradation of estuarine
1504 dissolved organic matter. *Limnology and Oceanography*, 45(6), 1254–1264.
1505 <https://doi.org/10.4319/lo.2000.45.6.1254>

1506 Müller, D., Warneke, T., Rixen, T., Müller, M., Jamahari, S., Denis, N., et al. (2015). Lateral
1507 carbon fluxes and CO₂ outgassing from a tropical peat-draining river. *Biogeosciences*,
1508 12(20), 5967–5979. <https://doi.org/10.5194/bg-12-5967-2015>

- 1509 Nichols, R. S., & Martin, P. (2021). Low biodegradability of dissolved organic matter from
1510 Southeast Asian peat-draining rivers. *Journal of Geophysical Research: Biogeosciences*.
1511 <https://doi.org/10.1029/2020JG006182>
- 1512 Painter, S. C., Lapworth, D. J., Woodward, E. M. S., Kroeger, S., Evans, C. D., Mayor, D. J.,
1513 & Sanders, R. J. (2018). Terrestrial dissolved organic matter distribution in the North
1514 Sea. *Science of the Total Environment*, 630, 630–647.
1515 <https://doi.org/10.1016/j.scitotenv.2018.02.237>
- 1516 Powers, L. C., & Miller, W. L. (2015). Photochemical production of CO and CO₂ in the
1517 Northern Gulf of Mexico: Estimates and challenges for quantifying the impact of
1518 photochemistry on carbon cycles. *Marine Chemistry*, 171, 21–35.
1519 <https://doi.org/10.1016/j.marchem.2015.02.004>
- 1520 Powers, L. C., Brandes, J. A., Miller, W. L., & Stubbins, A. (2017). Using liquid
1521 chromatography-isotope ratio mass spectrometry to measure the $\delta^{13}\text{C}$ of dissolved
1522 inorganic carbon photochemically produced from dissolved organic carbon. *Limnology
1523 and Oceanography: Methods*, 15(1), 103–115. <https://doi.org/10.1002/lom3.10146>
- 1524 Rixen, T., Wit, F., Hutahaean, A. A., Schlüter, A., Baum, A., Klemme, A., et al. (2022). 4 -
1525 Carbon cycle in tropical peatlands and coastal seas. In T. C. Jennerjahn, T. Rixen, H. E.
1526 Irianto, & J. Samiaji (Eds.), *Science for the Protection of Indonesian Coastal
1527 Ecosystems (SPICE)* (pp. 83–142). Elsevier.
1528 <https://doi.org/https://doi.org/10.1016/B978-0-12-815050-4.00011-0>
- 1529 Semiletov, I., Pipko, I., Gustafsson, Ö., Anderson, L. G., Sergienko, V., Pugach, S., et al.

1530 (2016). Acidification of East Siberian Arctic Shelf waters through addition of freshwater
1531 and terrestrial carbon. *Nature Geoscience*, 9(5), 361–365.
1532 <https://doi.org/10.1038/NEGO2695>

1533 Spencer, R. G. M., Stubbins, A., Hernes, P. J., Baker, A., Mopper, K., Aufdenkampe, A. K., et
1534 al. (2009). Photochemical degradation of dissolved organic matter and dissolved lignin
1535 phenols from the Congo River. *Journal of Geophysical Research*, 114(G03010).
1536 <https://doi.org/10.1029/2009JG000968>

1537 Stubbins, A., Spencer, R. G. M., Chen, H., Hatcher, P. G., Mopper, K., Hernes, P. J., et al.
1538 (2010). Illuminated darkness: Molecular signatures of Congo River dissolved organic
1539 matter and its photochemical alteration as revealed by ultrahigh precision mass
1540 spectrometry. *Limnology and Oceanography*, 55(4), 1467–1477.
1541 <https://doi.org/10.4319/lo.2010.55.4.1467>

1542 Stubbins, A., Mann, P. J., Powers, L., Bittar, T. B., Dittmar, T., McIntyre, C. P., et al. (2017).
1543 Low photolability of yedoma permafrost dissolved organic carbon. *Journal of*
1544 *Geophysical Research: Biogeosciences*, 122(1), 200–211.
1545 <https://doi.org/10.1002/2016JG003688>

1546 Susanto, D., Wei, Z., Adi, R., Zhang, Q., Fang, G., Fan, B., et al. (2016). Oceanography
1547 Surrounding Krakatau Volcano in the Sunda Strait, Indonesia. *Oceanography*, 29(2), 0–
1548 29. <https://doi.org/10.5670/oceanog.2016.31>

1549 Tzortziou, M., Osburn, C. L., & Neale, P. J. (2007). Photobleaching of dissolved organic
1550 material from a tidal marsh-estuarine system of the Chesapeake Bay. *Photochemistry*

- 1551 *and Photobiology*, 83(4), 782–792. <https://doi.org/10.1111/j.1751-1097.2007.00142.x>
- 1552 Urtizberea, A., Dupont, N., Rosland, R., & Aksnes, D. L. (2013). Sensitivity of euphotic zone
1553 properties to CDOM variations in marine ecosystem models. *Ecological Modelling*, 256,
1554 16–22. <https://doi.org/10.1016/j.ecolmodel.2013.02.010>
- 1555 Vähätalo, A. V., Salkinoja-Salonen, M., Taalas, P., & Salonen, K. (2000). Spectrum of the
1556 quantum yield for photochemical mineralization of dissolved organic carbon in a humic
1557 lake. *Limnology and Oceanography*, 45(3), 664–676.
1558 <https://doi.org/10.4319/lo.2000.45.3.0664>
- 1559 Vähätalo, A. V., Salonen, K., Münster, U., Järvinen, M., & Wetzel, R. G. (2003).
1560 Photochemical transformation of allochthonous organic matter provides bioavailable
1561 nutrients in a humic lake. *Archiv Fur Hydrobiologie*, 156(3), 287–314.
1562 <https://doi.org/10.1127/0003-9136/2003/0156-0287>
- 1563 Ward, C. P., Nalven, S. G., Crump, B. C., Kling, G. W., & Cory, R. M. (2017). Photochemical
1564 alteration of organic carbon draining permafrost soils shifts microbial metabolic
1565 pathways and stimulates respiration. *Nature Communications*, 8(1), 1–7.
1566 <https://doi.org/10.1038/s41467-017-00759-2>
- 1567 Ward, C. P., Bowen, J. C., Freeman, D. H., & Sharpless, C. M. (2021). Rapid and
1568 reproducible characterization of the wavelength dependence of aquatic photochemical
1569 reactions using light-emitting diodes. *Environmental Science and Technology Letters*,
1570 8(5), 437–442. <https://doi.org/10.1021/acs.estlett.1c00172>
- 1571 Weishaar, J. L., Aiken, G. R., Bergamaschi, B. A., Fram, M. S., Fujii, R., & Mopper, K.

1572 (2003). Evaluation of Specific Ultraviolet Absorbance as an Indicator of the Chemical
1573 Composition and Reactivity of Dissolved Organic Carbon. *Environmental Science &*
1574 *Technology*, 37(20), 4702–4708. <https://doi.org/10.1021/es030360x>

1575 White, E. M., Kieber, D. J., Sherrard, J., Miller, W. L., & Mopper, K. (2010). Carbon dioxide
1576 and carbon monoxide photoproduction quantum yields in the Delaware Estuary. *Marine*
1577 *Chemistry*, 118(1–2), 11–21. <https://doi.org/10.1016/j.marchem.2009.10.001>

1578 Wit, F., Rixen, T., Baum, A., Pranowo, W. S., & Hutahaean, A. A. (2018). The Invisible
1579 Carbon Footprint as a hidden impact of peatland degradation inducing marine carbonate
1580 dissolution in Sumatra, Indonesia. *Scientific Reports*, 8(1), 17403.
1581 <https://doi.org/10.1038/s41598-018-35769-7>

1582 Zepp, R. G. (2007). Solar UVR and aquatic Carbon, nitrogen, sulfur and metals cycles. In E.
1583 W. Helbling & H. Zagarese (Eds.) (pp. 137–184). Cambridge: Royal Society of
1584 Chemistry. <https://doi.org/10.1039/9781847552266-00137>

1585 Zhou, Y., Martin, P., & Müller, M. (2019). Composition and cycling of dissolved organic
1586 matter from tropical peatlands of coastal Sarawak, Borneo, revealed by fluorescence
1587 spectroscopy and parallel factor analysis. *Biogeosciences*, 16(13), 2733–2749.
1588 <https://doi.org/10.5194/bg-16-2733-2019>

1589 Zhou, Y., Evans, C. D., Chen, Y., Chang, K. Y. W., & Martin, P. (2021). Extensive
1590 Remineralization of Peatland-Derived Dissolved Organic Carbon and Ocean
1591 Acidification in the Sunda Shelf Sea, Southeast Asia. *Journal of Geophysical Research:*
1592 *Oceans*, 126(6), 1–23. <https://doi.org/10.1029/2021JC017292>

1593 Zika, R. G. (1981). Chapter 10 Marine Organic Photochemistry. In *Elsevier Oceanography*

1594 *Series* (Vol. 31, pp. 299–325). [https://doi.org/10.1016/S0422-9894\(08\)70332-5](https://doi.org/10.1016/S0422-9894(08)70332-5)

1595

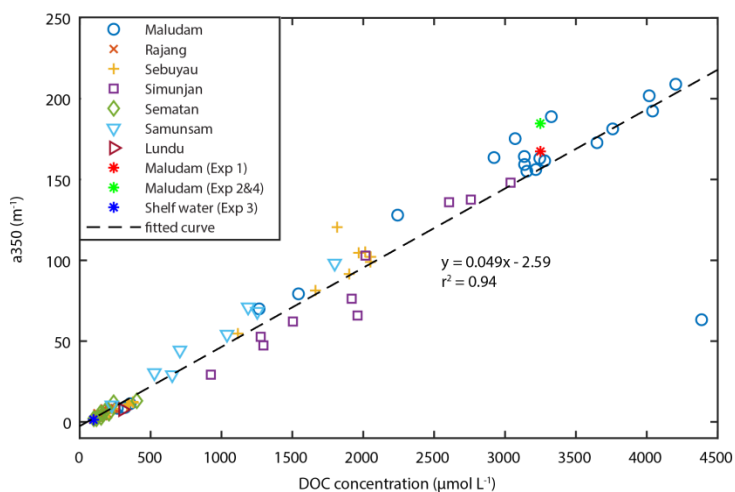
1596

1597

1598

1599

1600 **A3 Supplementary Figures and Tables**



1601

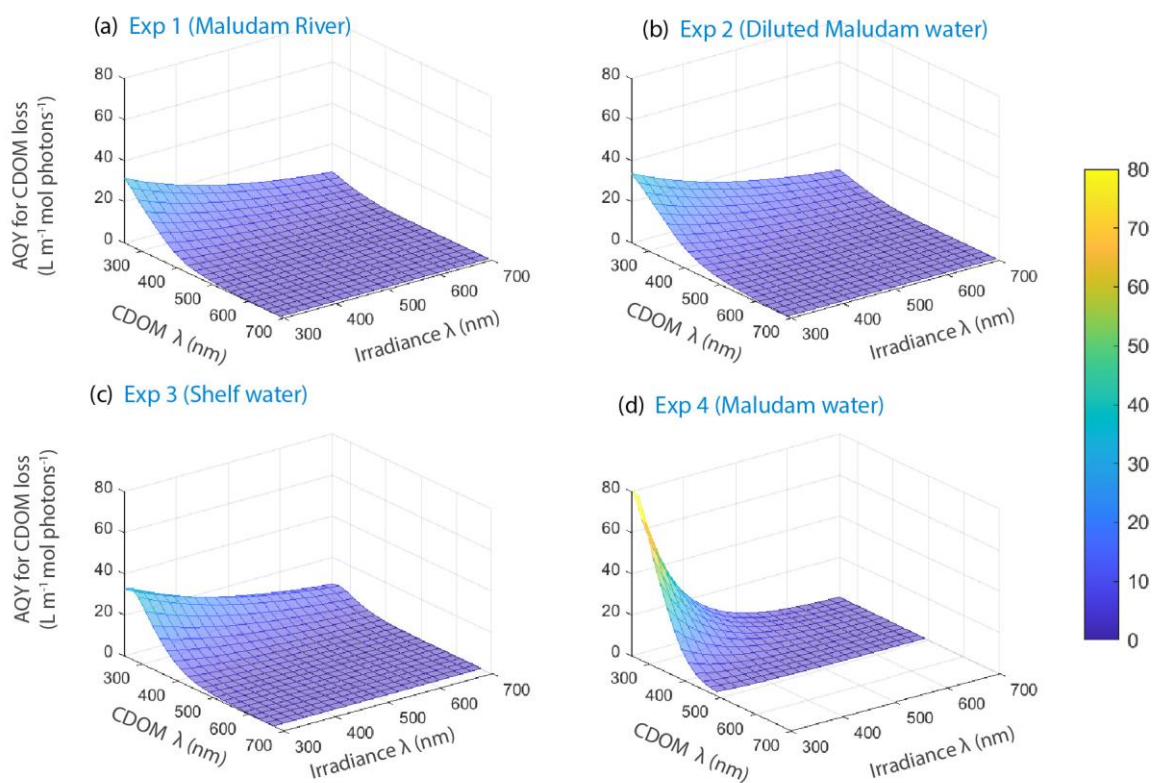
1602 Figure S1. Relationship between DOC concentration and CDOM absorption (a_{350}) across

1603 different rivers in Sarawak, Borneo (data from Martin et al. 2018), and in the shelf sea water

1604 sample collected in the Singapore Strait for Exp 3. Samples used to determine tDOC AQY in

1605 this study follow the relationship.

1606



1607

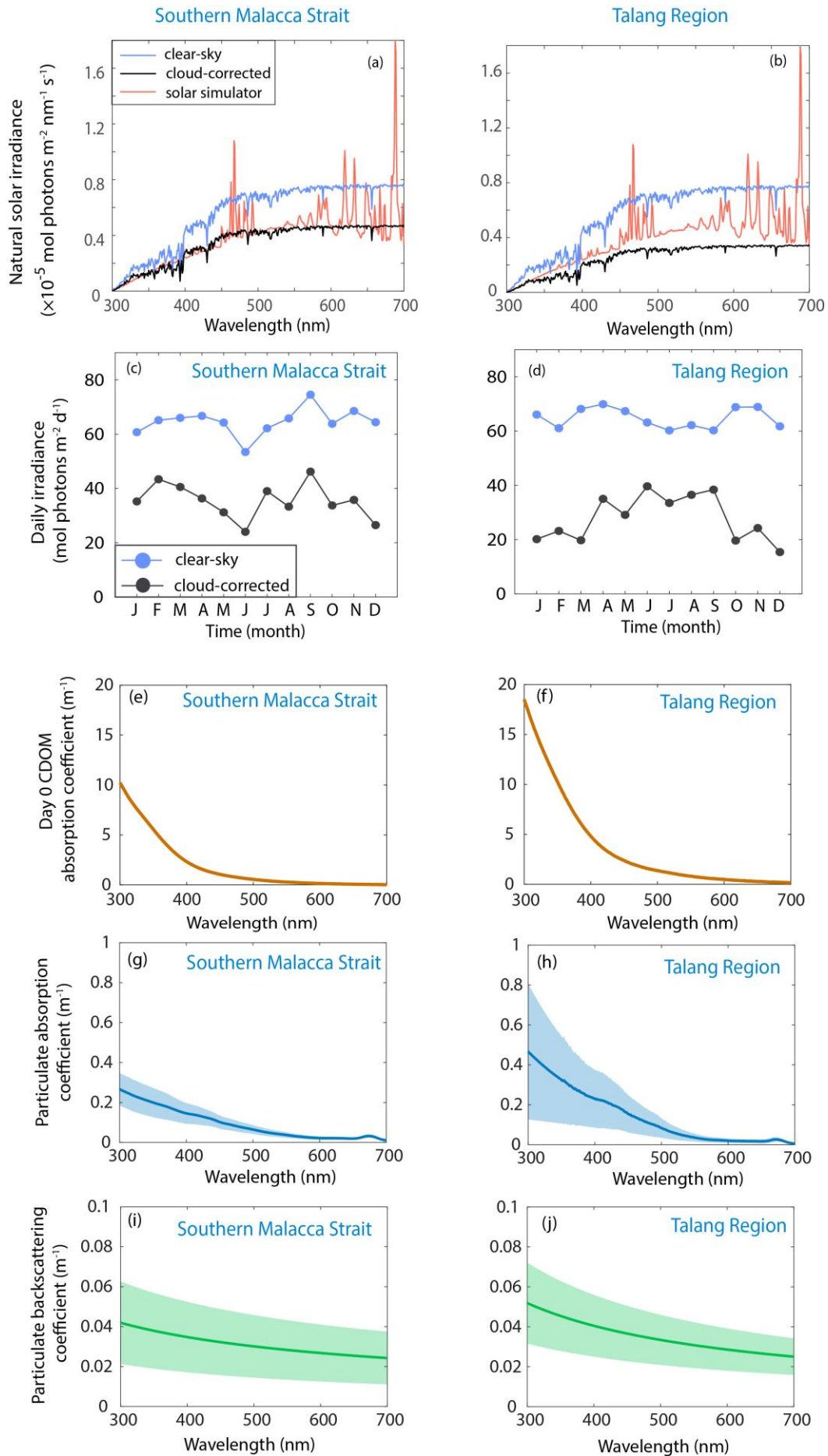
1608 Figure S2. Photochemical efficiency spectra for CDOM photobleaching, i.e. decrease in
 1609 volume-integrated absorption coefficient, calculated from data of Exp 1–4. In Exp 4, the
 1610 AQY for CDOM photobleaching above 500 nm of the CDOM absorption spectrum were
 1611 given in negative values, due to the measurement noise of CDOM absorption at the longer
 1612 wavelengths, and thus omitted.

1613

1614

1615

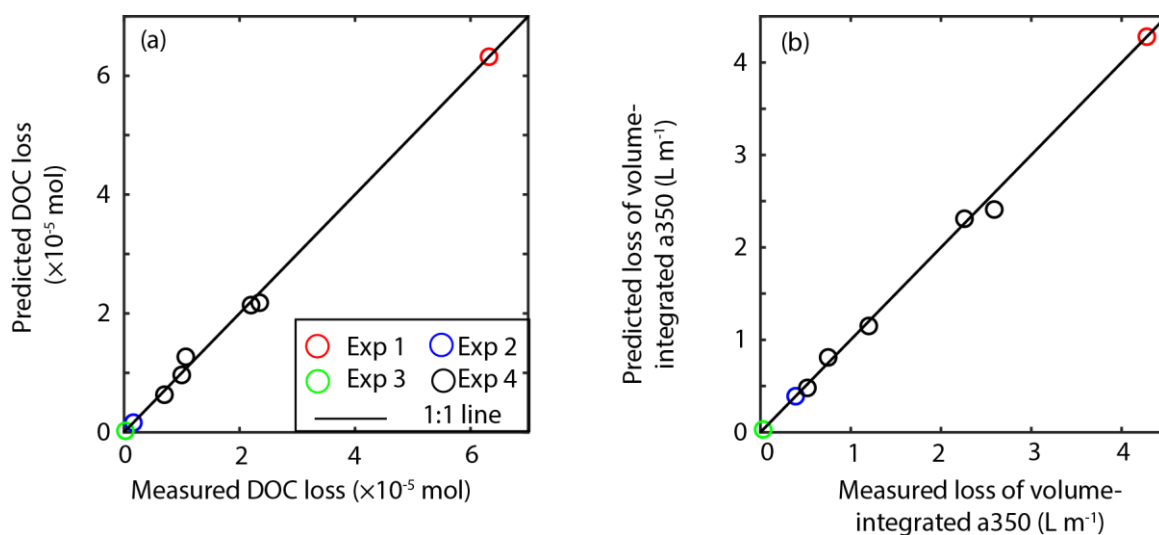
1616



1618 Figure S3. Model input data for both modeling regions. (a) – (b) Annual mean noon-time (12
 1619 pm local time) natural solar irradiance under clear-sky and cloud-corrected conditions for
 1620 both modeling regions, compared with the irradiance of the solar simulator for Exp 1–4. (c)–
 1621 (d) Seasonal variations in the daily irradiance under clear-sky and cloud-corrected conditions.
 1622 Daily irradiance for each month was integrated over 300 to 700 nm and 24 hours. (e)–(f)
 1623 Initial CDOM absorption spectra (i.e. in Day 0). (g)–(h) Particulate absorption spectrum. (i)–
 1624 (j) Particulate backscattering spectrum. The shading in panels g–j indicates the uncertainties
 1625 of the spectra calculated from all the spectrum for estimating the model output by Monte
 1626 Carlo simulation.

1627

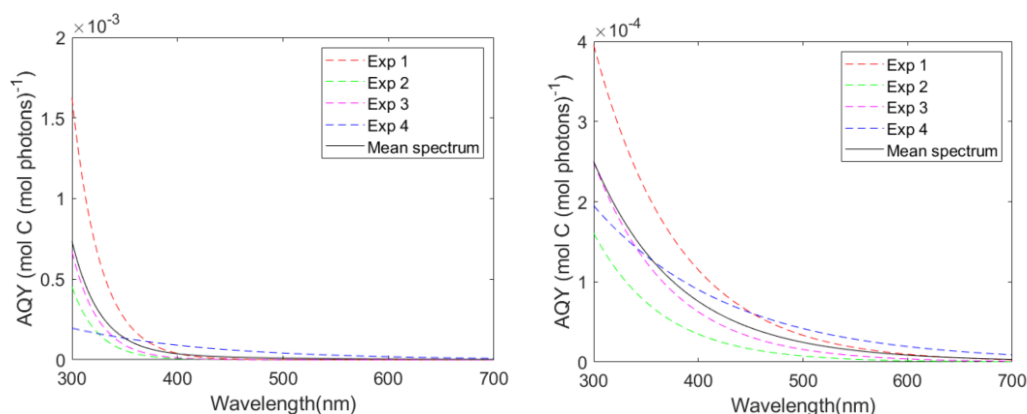
1628



1629

1630 Figure S4. Comparison of the measured and the optimized AQY-predicted (a) loss of DOC
 1631 and (b) loss of the volume-integrated a_{350} of CDOM of Exp 1 – 4. Data of Exp 4 were from
 1632 the multiple cut-off filters treatments.

1633



1634

1635

Figure S5. The AQY spectra of DOC photo-rem mineralization optimized using a

1636

starting value for c of 100 (left pane) and 0.01 (right pane). The AQY spectra in Fig.

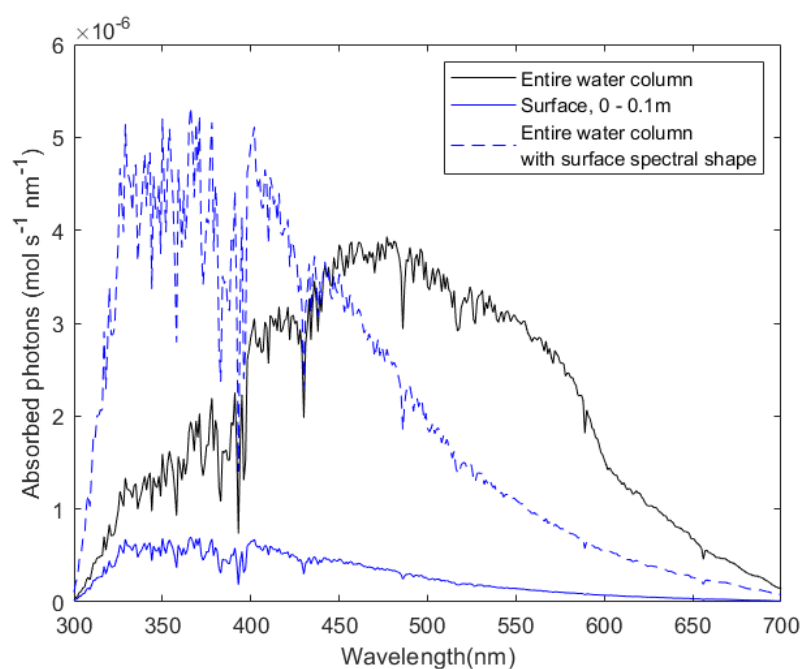
1637

4a in the original draft were optimized using a starting value of 1.0 as in Aarnos et al.,

1638

(2018).

1639



1640

1641 Figure S6. Spectra of photons absorbed by CDOM at the water surface (0 – 0.1m, solid blue
 1642 line) and depth-integrated for the entire water column (solid black line) in our model for a
 1643 1-m² grid in the Southern Malacca Strait region with irradiance spectrum at noon of July
 1644 2019. The dashed blue line shows a hypothetical absorbed photon spectrum for the same total
 1645 quantity of absorbed photons as for the black line, but with surface spectral shape (dashed
 1646 blue line). The broadband AQY from our photodegradation experiments could only be

1647 applied accurately to the whole water column if the spectrum of absorbed photons followed
1648 the dashed blue line, but in fact the absorbed photon spectrum is greatly shifted to longer
1649 wavelengths.

1650

1651

1652

1653 Table S1. Results from nitrite actinometry conducted following Jankowski et al., (1999). We
1654 measured the photo-production of salicylic acid in incubations in the Suntest solar simulator
1655 using experimental conditions as for our tDOC photodegradation experiments. The
1656 theoretically predicted photo-production of salicylic acid was calculated from the apparent
1657 quantum yield of salicylic acid production, the absorption spectrum of nitrite, and the
1658 irradiance spectrum of the test chamber as measured by the FLAME radiometer. The
1659 measured and predicted salicylic concentrations agree to within 6%, indicating that the
1660 irradiance spectrum measured by our radiometer can well represent the irradiance received
1661 inside the quartz cuvette we used for the photodegradation experiments.

1662

Cut-off wavelength of the optical filter used	Predicted salicylic acid concentration (nM)	Measured salicylic acid concentration (nM)	% difference
295nm	163	168	-2.97
320nm	151	160	-5.63

1663

1664

1665

1666

1667 Table S2. Variables in the photodegradation model.

Variable	Definition	Unit
a_{CDOM}	CDOM absorption coefficient	m^{-1}
a_{W}	Water absorption coefficient	m^{-1}
a_{p}	Particulate absorption coefficient	m^{-1}

bb_w	Water backscattering coefficient	m^{-1}
bb_p	Particulate backscattering coefficient	m^{-1}
K_d	Downwelling attenuation coefficient	m^{-1}
$E_{d,0+}$	Solar irradiance just above the sea surface	$mol\ photons\ m^{-2}\ s^{-1}$
$E_{d,0-}$	Solar irradiance just below the sea surface	$mol\ photons\ m^{-2}\ s^{-1}$
ϵ	Photons absorbed by CDOM	mol
λ	Wavelength	nm
θ	Solar zenith angle	degree
ϕ_{DOC}	Apparent quantum yield for photo-remineralization of DOC	$Mol\ DOC\ (mol\ photons)^{-1}$
ϕ_{CDOM}	Apparent quantum yield for photo-induced loss of volume-integrated CDOM absorption coefficient. For example ϕ_{a350} is the apparent quantum yield for the photo-induced loss of volume-integrated CDOM absorption coefficient at 350nm.	$L\ m^{-1}\ (mol\ photons)^{-1}$

1668

1669

1670

1671

1672 Table S3. Changes in DOC and CDOM parameters during photodegradation experiments.

	DOC ($\mu\text{mol L}^{-1}$)	a_{350} (m^{-1})	$S_{275-295}$ (nm^{-1})	SUVA ₂₅₄ (L mg^{-1} m^{-1})
Exp 1 (Maludam River water, 416 hours)				
Initial	3250	167.4	0.011	5.41
End	850	5.9	0.021	1.23
%loss	74%	96%		
Exp 2 (diluted Maludam water, 462 hours)				
Initial	204	13.5	0.010	6.06
End	150	0.6	0.032	1.61
%loss	26%	96%		
Exp 3 (Singapore water during tDOC input, 500 hours)				
Initial	97	1.4	0.018	2.40
End	88	0.3	0.032	1.53
%loss	9%	79%		
Exp 4 (Maludam River water, 144hours, no-optical-filer treatment)				
Initial	3249	184.7	0.011	5.87

End	2268	85.9	0.014	4.52
%loss	30%	54%		

1673

1674

1675

1676

1677 Table S4. The broadband Apparent Quantum Yield (AQY) for DOC photo-remineralization
 1678 calculated for different time intervals from Exp 1 – 3. We did not observe a steady decrease in
 1679 AQY over time. Only data before DOC concentration stopped to decrease were used to
 1680 calculate AQY.

Exp No.	Time Interval (hour)	DOC loss (μmol) within the quartz cell	Absorbed photons (mol) Integrated over 290–700 nm	Broadband AQY ($\mu\text{mol C mol photons}^{-1}$)
1 (Maludam Water)	0 – 72	15	0.15	100
	72 – 144	10	0.14	74
	144 – 216	8	0.12	64
	216 – 288	10	0.10	101
	288 – 258	12	0.08	153
	358 – 431	7	0.07	110
	0 – 431	63	0.66	95
2 (Maludam mixed with seawater)	0 – 51	0.33	0.014	25
	51 – 111	0.42	0.0087	48
	111 – 188	0.12	0.0069	16
	188 – 268	0.048	0.0044	11
	268 – 362	0.36	0.0028	128
	362 – 462	0.35	0.0019	178
	0 – 462	1.61	0.0383	42

3 (Singapore Strait)	0 – 24	0.078	0.00063	123
	24 – 70.5	0.075	0.00094	80
	70.5 – 119	0.017	0.00073	23
	119 – 170.5	0.074	0.00056	133
	0 – 170.5	0.24	0.0029	85

1681

1682

1683 Table S5. Simulation results of tDOC remineralization by photodegradation in the Southern
 1684 Malacca Strait using broadband AQY in the model, showing much larger tDOC loss
 1685 compared to the results based on spectrally-resolved AQY (summarized in Table 2).

Conditions	Initial ($\mu\text{mol L}^{-1}$)	Final ($\mu\text{mol L}^{-1}$)	%loss
Clear-sky	108	45	58%
Cloud-corrected	108	63	42%

1686

1687

1688

1689

1690

1691 Table S6. Comparison of modelling results between using different starting values of
 1692 coefficient c for optimizing AQY spectra.

	Initial DOC ($\mu\text{mol/L}$)	Final DOC ($\mu\text{mol/L}$)		
Starting value used		0.01	1.0	100
Southern Malacca Strait, cloud corrected	108	81	86	88
Talang Region, cloud corrected	181	173	174	176

1693